Fall 12-2021

Characterization and Influence of the McMurdo Shear Zone, Antarctica on the Ross Ice Shelf and Its Tributary

Lynn Kaluzienski
University of Maine, lynn.kaluzienski@maine.edu

CHARACTERIZATION AND INFLUENCE OF THE MCMURDO SHEAR ZONE, ANTARCTICA ON THE ROSS ICE SHELF AND ITS TRIBUTARY GLACIERS

By

Lynn Marie Kaluzienski

B.S., Emory University, 2014

A DISSERTATION

Submitted in Partial Fulfillment of the

Requirements for the Degree of

Doctor of Philosophy

(in Glaciology and Remote Sensing)

The Graduate School

The University of Maine

December 2021

Advisory Committee:

Peter Koons, Professor in School of Earth and Climate Sciences, Co-Advisor

Gordon Hamilton, Professor in School of Earth and Climate Sciences (deceased), Co-Advisor

Chris Borstad, Assistant Professor in Civil Engineering, Montana State Univ.

Seth Campbell, Assistant Professor in School of Earth and Climate Sciences

Zoe Courville, Adjunct Assistant Professor in Engineering, Dartmouth University

Ellyn Enderlin, Assistant Professor in Department of Geoscience, Boise State Univ.

Eric Landis, Professor in Civil and Environmental Engineering

Martin Truffer, Professor in Department of Physics, Univ. of Alaska, Fairbanks

CHARACTERIZATION AND INFLUENCE OF THE MCMURDO SHEAR ZONE, ANTARCTICA ON THE ROSS ICE SHELF AND ITS TRIBUTARY GLACIERS

By Lynn Marie Kaluzienski

Dissertation Co-Advisors: Koons/Hamilton

An Abstract of the Dissertation Presented
in Partial Fulfillment of the Requirements for the
Degree of Doctor of Philosophy
(in Glaciology and Remote Sensing)
December 2021

As ice shelves are floating and lack resistive stress at their base, resistance to flow is accommodated along their lateral margins and various pinning points such as ice rises and nunataks. As such, ice shelf shear margins and their strength through time remain a critical control on ice shelf stability. Specifically, lateral shear zone destabilization is an important precursor to ice shelf collapse. In this thesis I utilize *in-situ*, remote sensing, and numerical modeling techniques in order to characterize the flow field and geometry of the western lateral margin of the Ross Ice Shelf as well as a region upstream of the grounding line. I first develop a method to investigate the kinematic drivers of crevasse initiation in the McMurdo Shear Zone, Antarctica through the delineation of crevasse features from ground penetrating radar observations and comparison with kinematic outputs derived from remotely-sensed ice surface velocities. I then use spatial patterns in crevasse attributes to make inferences on crevasse history and discuss implications on the current and future stability of the shear margin. Next, I estimate ice thickness within this shear margin from a combination of mid-frequency ground penetrating radar observations and Digital Elevation Models and assess the sensitivity of Ross Ice Shelf stress balance to uncertainties in ice thickness datasets within this region through numerical modeling

techniques. My results suggest that previous modeling frameworks have overestimated the sensitivity of the region to melting. Finally, I perform a transient streamline analysis of a region of upstream grounded ice known as the Whillans and Ice Stream and characterize the short-term velocity fluctuations within its slowdown evolution using available remotely-sensed velocity datasets between 1997 and 2016. I incorporate these observations of velocity fluctuations as well as mass changes into a transient finite element modeling solution of ice flow. Through inversion techniques, I estimate annual changes in basal shear stress in order to force a 100-year transient model of ice slowdown for the Whillans Ice Stream and discuss the possible mechanisms that could be driving slowdown fluctuations on annual timescales such as lake drainage events, basal freeze-on and till weakening mechanisms, as well as changes to downstream boundary conditions.

DEDICATION

This work is dedicated to Dr. Gordon Hamilton. You inspired me from the first and will continue to be the kind of scientist I strive to become.

ACKNOWLEDGEMENTS

First and foremost, I would like to express my sincere gratitude to my advisors, Gordon Hamilton and Peter Koons. Thanks to Gordon for teaching me the fundamentals of fieldwork and supporting and encouraging my research proposal ideas. Your memory continues to provide inspiration down my path as a glaciologist. Thanks to Peter Koons for your unwavering support throughout my degree. Over the past 7 years I have encountered many setbacks on the circuitous journey to finishing my dissertation. You have stood by my side and provided guidance through it all and for that I am enormously grateful. Thanks to Ellyn Enderlin for stepping up to co-advise me in the period after Gordon's passing. I appreciate all that you did to provide a supportive space within the UMaine Glaciology Lab and all of your thorough and helpful feedback throughout the writing process.

I owe a debt of gratitude to the rest of my committee who provided helpful suggestions and critiques along the way. Special thanks to Dr. Martin Truffer for agreeing to host my visiting studentship at the University of Alaska Fairbanks. You played a large part in making UAF feel like a home and I am thankful for your mentorship and insightful advice both within and outside of academia. Thank you to Dr. Seth Campbell who helped me search for sponsoring institutions and fostering my skills in field glaciology both on the Juneau Icefield and in Antarctica. You helped me gain back confidence in my research abilities at a difficult time. Thank you to Dr. Zoe Courville for providing the opportunity to become a student trainee at CRREL and dealing with my nonstop emails with understanding and humor. Thank you to Dr. Chris Borstad who supported field opportunities in Svalbard and provided invaluable guidance throughout my numerical modeling work. I would also like to thank Dr. Eric Landis for his unique perspective and encouragement.

Outside my committee I would also like to express gratitude to Dr. Nicole Schlegel for giving me one-on-one modeling guidance at all times of the day and night. Special thanks

to Dr. Steven Arcone for his invaluable radar expertise. And thank you to everyone on my various field crews, especially Ben, Josh, Austin, Jim and Peter Braddock.

A HUGE thanks to the glaciology groups at UMaine and UAF as well as peers and friends both within and outside of work. I would very much like to thank my dear friend Jessica Scheick who helped me through more than one existential life crisis. Thank you to Konstanze Haubner who drove cross country on my academic road trip from Maine to Alaska and has helped me with numerical modeling issues throughout my dissertation. And thank you to Fiona, for always providing a welcoming home for me when I visit Maine. Finally I would like to thank my family, most of all my mother and brother who have dealt with my relocation to further and further away places. Funding for this work comes from the National Science Foundation under grants ANT-1264000 and ANT-1245915 as well as the Cold Regions Research and Engineering Lab.

TABLE OF CONTENTS

LIST OF TABLES

LIST OF FIGURES

CHAPTER 1

INTRODUCTION: ICE SHELF STABILITY

1.1 Introduction

1.1.1 Introduction and Aims of Thesis

Ice shelves (i.e., expansive floating sections of glacier ice) fringe most of Antarctica's coastline, provide resistance to ice flow from the ice sheet interior, and control the rate of ice discharge into the ocean. As nearly 75 percent of the ice flux from the Antarctic Ice Sheet passes through ice shelves (Bindschadler and others, 2011), understanding controls on ice shelf stability is paramount to future predictions of sea level rise. The Antarctic Ice Sheet stores approximately 26 million gigatons of ice, estimated at 58 m of sea level rise equivalent, yet uncertainties in centennial global sea-level rise predictions are dominated by uncertainties in ice sheet contributions (van de Wal and others, 2019). Current contributions to sea-level rise are dominated by thermal expansion and mountain glacier melt input, but recent modeling efforts predict meltwater outputs from the Antarctic and Greenland Ice Sheets will surpass these inputs by the end of the century (van de Wal and others, 2019).

The importance of floating ice shelf influence on ice sheet contributions to sea-level rise was not widely agreed upon until roughly a decade ago. Ice sheets and ice shelves were assumed to be mechanically uncoupled with ice shelves acting as passive bodies of ice. Now the concept of buttressing – that ice shelves exert a back-force at the grounding line and resist the flow of their tributary glaciers – is widely accepted as a critical control on the force balance of ice sheets (Pattyn, 2018). However, ice sheet models still struggle to capture changes in bulk rheology and buttressing due to the mechanical weakening of ice shelves.

Lateral margin resistance is particularly important for ice shelves due to the absence of resistive stresses at their base. The strength of these shear margins and stability through

time is therefore a critical control on ice shelf stress balance. Specifically, lateral shear zone destabilization is an important precursor to ice shelf collapse (Scambos and others, 2008). Therefore, detailed observations of shear margins can serve as important indicators of overall ice shelf stability. In addition, a deeper understanding of the mechanisms by which shear margins weaken will be important.

1.1.2 Definition and Characteristics of Ice Shelf Shear Margins

Ice shelf shear margins are zones of focused strain localization resulting from steep velocity gradients where relatively fast-flowing ice moves past bedrock or neighboring slower moving ice. They are typically located along the lateral margins of glaciers or within the confluence of glacial streams in ice shelves. In this dissertation, I will focus on two regions of interest along the Ross Ice Shelf (RIS). The first is the McMurdo Shear Zone (MSZ), a relatively well-studied segment of the western lateral margin of the Ross Ice Shelf (RIS) where fast ice ($\sim$450 m yr^{-1}, estimated from GPS observations during field data acquisition) shears past the slower-moving McMurdo Ice Shelf (MIS; $\sim$200 m yr^{-1}; Arcone and others 2016), creating a 5–10 km wide zone of intense crevassing. The second is the confluence of the Whillans and Mercer ice streams (WMIS) flowing out of the Siple Coast region of West Antarctica and into the RIS. A long-term slowdown ($\sim$4 m yr^{-1}) and a thickening (0.06 + 0.02 m yr^{-1}) of the Whillans Ice Stream are believed to be occurring (Joughin and others, 2005; Stearns and others, 2005), which influences the shear margin dividing Whillans and Mercer Ice Streams. However, the consistency of this slowdown and changes to the shear margin are unknown.

1.2 Factors Influencing Ice Shelf Stability

While the effects of climate change such as increased atmospheric and oceanic warming are certainly important in influencing ice-shelf stability, this dissertation focuses on exploring the mechanisms by which these changes occur. Factors influencing ice-shelf

stability include surface mass balance (Banwell and MacAyeal, 2015; DeConto and Pollard, 2016), ocean induced basal melt and freeze-on processes (e.g. Alley and others 2016; Craven and others 2009, ice shelf fracture and suturing processes (Jansen and others, 2013; Kulessa and others, 2014) and lateral ice shelf buttressing due to contact with land (i.e. pinning points) or adjacent slower moving ice (Favier and others, 2016; Reese and others, 2018).

Observations of thinning ice shelves across Antarctica point to a common sequence of events along their lateral margins that follow initial submarine melt-driven thinning: thinning increases susceptibility to fracture and crevassing, which reduces the load-bearing surface area and lateral drag provided by the ice shelves, and ultimately results in a substantial loss of buttressing potential at the grounding line (Dupont and Alley, 2005; Khazendar and others, 2015; MacGregor and others, 2012).

By far the most important contribution to uncertainty of ice sheet contributions to sea level rise is the effect of the Marine Ice Sheet Instability (Robel and others, 2019). This is the hypothesis, first put forward by Weertman in 1974 (Weertman, 1974), that the West Antarctic Ice Sheet is preconditioned for collapse. This instability is a result of the fact that the majority of the ice sheet lies below sea level which leads to the following positive feedback effect: initial basal melt at the grounding line causes the ice sheet to retreat into deeper water, exposing a greater surface area to basal melt. This process is believed to have occurred in paleo- records (Pollard and others, 2015), and is predicted to be occurring again in present times (Ritz and others, 2015).

1.2.1 Feedbacks on Floating Ice

While the MIS has important consequences at the grounding line, several significant feedbacks occur within the shear margins of ice shelves. The first feedback concerns the effect of deformational heating. Ice is a non-Newtonian fluid in which thermomechanical feedbacks occur. The viscosity of ice for a given stress decreases with temperature, with warmer ice deforming more readily than colder ice under the same applied stress.

Therefore, an inherent feedback occurs with strain heating: faster ice flow leads to higher rates of shear heating and further ice softening. This process is often exacerbated by feedbacks related to ice fabric, crystallographic orientation, and ice impurities (Jones and Glen, 1969; Budd and Jacka, 1989; Cyprych and others, 2016). As ice flows, its crystalline fabric changes in response to the stresses it has encountered. While crystallographic orientation away from shear margins is typically isotropic, crystals within regions of high shear are known to rotate to a preferred orientation that is more easily deformable (Qi and others, 2019); this in turn leads to an increased rate in shear.

1.2.2 Feedbacks within Grounded Regions

While dynamic feedbacks along ice shelves mostly occur at their lateral margins, grounded ice regions have some additional feedback processes that can occur at the ice-bed interface. For the fast flowing ice streams of West Antarctica, these inherent instabilities can lead to the complete stagnation of an ice stream on the order of a thousand year time period, such as has been documented at the Kamb Ice Stream (Catania and others, 2006). While the exact mechanism of the switch from stagnation to activation is unknown, a cyclic nature can be observed: fast motion induces melting at the ice-bed interface which reduces basal shear stress. As ice speeds up, a thinning occurs which leads to a greater basal temperature gradient, and heat due to frictional heating is advected away from the bed more efficiently (Christoffersen and Tulaczyk, 2003a). This increase in temperature gradient can lead to a switch from basal melting to basal freeze-on (Tulaczyk and others, 2000). As basal freeze-on increases, ice flow slows down which reduces the contribution of shear heating, which is then compensated by the latent heat of fusion (i.e. more basal freeze-on) which can lead to further ice deceleration.

While this runaway process can lead to ice stream stagnation on its own, the feedback is further complicated by the non-linear rheological properties of till. Till rheology is believed to be largely a function of stress and water content, with water-saturated till being

less consolidated and weaker. The instability is again tied to thermomechanics, with the transport of water and heat within the till being coupled (Christoffersen and Tulaczyk, 2003b). As freeze-on occurs at the ice-till interface, this causes a heat sink, and water flows out of the till leading to dewatering. This reduction in water content leads to a more consolidated (i.e. stronger) till layer which can enhance slowdown (Bougamont and others, 2011). The highly non-linear (quasi-plastic) rheology (i.e. resistive to flow until a critical yield stress is reached) is not easily adopted in ice flow models, making predictions on the timing of ice stream stagnation difficult.

1.3 Ice Shelf Buttressing and Tributary Glacier Dynamics

The importance of back-stress, defined qualitatively as a stress induced by anything that resists the forward motion of glacial ice (Thomas, 1973), is clear when considering the effects of the rapid, large-scale collapse of the Larsen A and B ice shelves along the Antarctic Peninsula on ice discharge from their tributary glaciers (Glasser and Scambos, 2008). For instance, glaciers that fed the Larsen B ice shelf exhibited as much as an eight-fold increase in velocity following the collapse of the ice shelf in 2002 (Rignot and others, 2004). While peak flow velocity has since decreased following its initial collapse, Larsen B's disintegration has continued to have significant and long-lasting impacts on the discharge of tributary glaciers in the region (Rott and others, 2011; Khazendar and others, 2015). Less severe changes along ice shelves can also considerably alter the stress balance distribution of tributary glaciers, resulting in a reduction of back-stress and subsequent sea level rise (MacGregor and others, 2012; Khazendar and others, 2015).

1.4 Summary and Dissertation Objectives

The overarching aim of this dissertation is to improve our understanding of ice sheet dynamics and the role of floating ice in modulating mass flux across the grounding lines of the Antarctic Ice Sheet. This work focuses on three main objectives:

- Characterize the flow field and geometry of the western lateral margin of the Ross Ice Shelf using remote-sensing derived surface kinematics and ground penetrating radar
- Infer the sensitivity of grounding line flux of the Ross Ice Shelf to changes observed at its western lateral margin utilizing finite element numerical modeling of ice flow, temperature, and stress balance
- Assess the downstream impact of a reduction in buttressing by characterizing the flow field and basal properties at the Whillans/Mercer Ice Stream confluence through time and comparing the time series with predicted trends from ice stream modeling efforts

1.4.1 Overview of Chapters

In Chapter 2, I investigate the kinematic drivers of crevasse initiation in the McMurdo Shear Zone, Antarctica. To do so, I delineate crevasse features within a robust high frequency ground penetrating radar dataset collected within the region. I compare these with kinematic outputs derived from remotely-sensed ice surface velocities in order to develop a statistical method to estimate crevasse initiation threshold values. I then use spatial patterns in crevasse attributes such as width and overlying snowbridge thickness to make inferences on crevasse history. I close with a discussion of the implications on the current and future stability of the shear zone as well as regional consequences to logistic operations along the shear zone. In the third chapter, I assess the sensitivity of Ross Ice Shelf stress balance to uncertainties in ice thickness datasets, in particular along its western lateral margin. I first present estimates of ice thickness based on *in-situ* GPR observations and surface elevation observations within the McMurdo Shear Zone. I then utilize the Ice Sheet System Model (ISSM; Larour and others 2012) to explore both instantaneous transient effects of localized thinning within the region and their associated sea-level rise.

In Chapter 4, I characterize short-term velocity fluctuations in the slowdown evolution of the Whillans Ice Stream and discuss implications on the flow of the neighboring Mercer Ice Stream as well as crevasse initiation within the region. To do so, I combine crevasse

observations from high-frequency ground penetrating radar surveys, kinematic outputs derived from available satellite derived velocity outputs, as well as a detailed flow-line analysis through time. Next, I incorporate these velocity fluctuations as well as mass changes into finite element modeling solutions. Through inversion techniques, I estimate annual changes in basal shear stress in order to force a 100-year transient model of ice slowdown for the WIS. I close the chapter with a discussion of the possible mechanisms that could be driving slowdown fluctuations on annual timescales such as lake drainage events, basal freeze-on and till weakening mechanisms, as well as changes to downstream boundary conditions.

CHAPTER 2
CREVASSE INITIATION AND HISTORY WITHIN THE MCMURDO SHEAR ZONE, ANTARCTICA

2.1 Introduction

Ice shelf shear margins are zones of focused strain localization resulting from steep velocity gradients where relatively fast-flowing ice moves past bedrock or neighboring slower moving ice. They are typically located along the lateral margins of glaciers or within the confluence of glacial streams in ice shelves. Shear zone stability represents a potentially critical control on the mass balance of Ice Sheets because ice shelves buttress the flow of ice from the Ice Sheet interior (Reese and others, 2018). Observations across Antarctica point to a common sequence of lateral shear zone destabilization that follows initial submarine melt-driven thinning: thinning increases susceptibility to fracture and crevassing, which reduces the load-bearing surface area and lateral drag provided by the ice shelves, and ultimately results in a substantial loss of buttressing potential at the grounding line (Dupont and Alley, 2005; Khazendar and others, 2015; MacGregor and others, 2012). While several modeling studies have highlighted the crucial role lateral margins play in ice shelf stability (Favier and others, 2016; Khazendar and others, 2015), feedbacks between thinning, mechanical weakening and fracture, and calving have only recently been successfully incorporated into numerical ice shelf modeling (Borstad and others, 2012, 2016). Here I present a statistical approach to predict crevasse initiation in a shear zone based on surface velocity observations and using ground penetrating radar as calibration.

The strong lateral gradients in velocity produce regions of local expansion and tensile failure generates extensive swaths of concentrated crevassing. Multiple studies have laid the groundwork for deriving critical strain rate and principal stress thresholds for crevasse initiation based on field observations (Kehle, 1964; Meier, 1958; Vaughan, 1993). However, crevasse initiation depends on several factors including ice temperature, density, impurities,

crystallography, and history (Vaughan, 1993), such that critical thresholds will vary in type and value across different glacial environments. A more thorough understanding of crevasse initiation thresholds could better capture the aforementioned feedbacks between acceleration, crevassing, and weakening in large-scale numerical models which currently only parameterize these feedbacks through damage—a scalar variable that quantifies the loss of load-bearing surface area due to ice shelf fracture. Alternatively, Emetc and others (2018) used a statistics-based approach to predict the location of observed surface fractures based on several potential parameters including flow regime, geometry, and mechanical properties of ice. They found the most reliable predictor parameters for modeling surface fractures on ice shelves to be the effective strain rate (i.e., the second invariant of the strain rate tensor) and principal stress.

Understanding crevasse initiation may best be achieved with small-scale observations in which crevasses can be directly observed. While large-scale observations of intensified fracture and rifting have been observed through remote-sensing observations (Borstad and others, 2017), snow cover may obscure the full extent of a crevasse field—particularly in regions of high snow accumulation—requiring *in-situ* observations to accurately map crevasses. I combine crevasse observations from high-frequency ground penetrating radar (GPR) surveys and kinematic outputs derived from remotely-sensed ice surface velocities of the McMurdo Shear Zone, Antarctica, to develop a statistical method to investigate the kinematic drivers of crevasse initiation and to estimate crevasse initiation threshold values. While the crevasse initiation strain rate threshold for the McMurdo Shear Zone is not directly transferable to other glacial settings, the method can be used as a tool for monitoring dynamic changes in shear zones through time with minimal *in-situ* data. The method can also be leveraged to optimize safety when collecting *in-situ* observations within or traversing potentially crevassed regions.

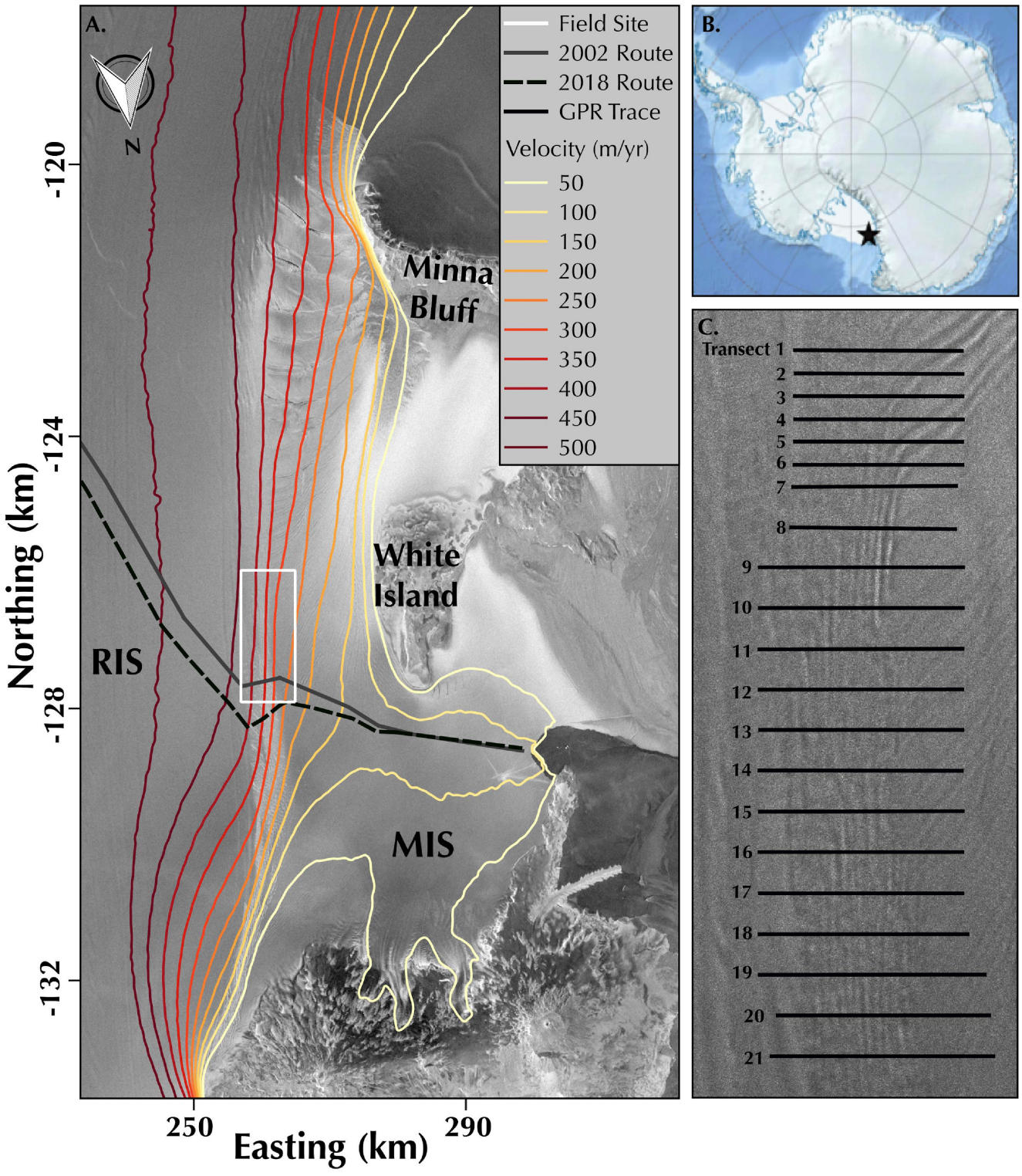

Figure 2.1. McMurdo Shear Zone location map. (a) Radarsat2 image of the MSZ with contour map of velocity from MEaSUREs2. 2002 and 2018 SPoT route locations are noted by the solid grey line and dashed lines respectively.(b) Overview of Antarctica with location of MSZ noted by red star. (c) GPR transects superimposed on 2017 TerraSAR-X image.

2.1.1 The McMurdo Shear Zone

This study focuses on the McMurdo Shear Zone (MSZ), a relatively well-studied segment of the western lateral margin of the Ross Ice Shelf (RIS) where fast ice (∼450 m yr^{-1}, estimated from GPS observations during field data acquisition) shears past the slower-moving McMurdo Ice Shelf (MIS; ∼200 m yr^{-1}), creating a 5–10 km wide zone of intense crevassing (Fig. 2.1). A weakening of this lateral margin has the potential to destabilize the RIS, as has been observed and modeled on smaller ice shelves (MacGregor and others, 2012; McGrath and others, 2012; Vieli and others, 2007). Widths of crevasses from ground-truth data in this region have ranged from small <0.5 m-wide cracks to ∼14 m-wide (Courville, 2015). Near surface crevasses typically oriented at ∼45° to flow (Arcone and others, 2016) indicate relatively recent formation given the rotation associated with shear.

Synchronous and aligned crevassing occurs in the marine ice at ∼160 m depth in the study area, despite a lack of evidence of open meteoric englacial fractures (Arcone and others, 2016). This suggests that the englacial ice is under great stress, likely fractured, and the greatest source of potential instability. Recent modeling by Reese and others (2018) predicts that moderate thinning in this region could have far-reaching effects, including an immediate acceleration of the Bindschadler and MacAyeal ice streams located more than 900 km away. Recent observed changes of summer ice flow direction along the MIS following a break-up event in March 2016 (Banwell and others, 2017; MacAyeal, personal communication; MacDonald and others, 2019) suggest that dynamic changes may already be underway in this previously stable region.

The MSZ region is also logistically important to the U.S. and New Zealand Antarctic research programs. The United States Antarctic Program (USAP) annually mitigates crevasse hazards along the South Pole Traverse (SPoT) route that crosses the MSZ. Since the route's creation in 2002 it has advected northward past White Island into a region of greater flow divergence and intensified crevassing motivating the need to chart a new route

across the MSZ where crevassing is minimal. Crevasses along the route have been monitored yearly with GPR for infrequent mitigation (filling). My observations from 2017 add to this dataset and provide the most spatially extensive and robust dataset of *in-situ* crevasse observations to date.

2.2 Methods

I analyzed ∼95 km of high-frequency ground penetrating radar (GPR) data collected within the MSZ in October of 2017. I identified individual crevasse features and estimated their maximum width and overlying snowbridge thickness. Kinematic outputs such as shear strain rate, dilatation rate, and vorticity rate were derived from MEaSUREs2 and auto-RIFT ice flow velocities. I estimated the relative frequency distribution of crevasses with respect to the kinematic data outputs. By utilizing these relative frequency distribution plots I then predicted the number of crevasses along two potential routes across the MSZ. Details of the methods used to process and analyze these data are provided below.

2.2.1 GPR Collection and Processing

I used a GSSI SIR30 control unit and model 5103 400MHz antenna unit to record 20 traces s^{-1} over a time range of 200 ns (∼20 m in firn) and 4096 32-bit samples/trace with a time-variable gain. This time range was guided by GPR observations from previous field seasons where minimal crevassing was found below 20 m (Arcone and others, 2016). I deployed two four-wheel-drive battery-powered rovers (Yeti, Trautmann and others 2009; and Scotty, Lever and others 2013, a later adaptation of Yeti's design) to tow two separate GPR systems (to cover more ground) at a constant speed of ∼1.5 m s^{-1}. Each rover was coupled with a Garmin-19x GPS system and followed waypoints along 21 preplanned transect routes orthogonal to overall ice flow direction (Fig. 2.1). This field survey was designed both to investigate the spatial distribution of crevassing upstream of the SPoT

where few observations have been gathered in the past, and to examine the inheritance of past rifting at the tip of Minna Bluff. Transect length and spacing were constrained by rover battery power capabilities and amount of time spent in the field.

I manually identified the leading edge of the direct-coupling wave (i.e., a combination of direct transmission between transmitter and receiver antennas, and a surface reflection) in the radar profiles, and set the depth to zero at that point. I then used the travel time to depth conversion to transform the round-trip transit time into thickness using the following formula

$$d = \left(\frac{ct}{2\sqrt{\epsilon_r}} \right) \tag{2.1}$$

where ϵ_r is the dielectric permittivity (dimensionless), c is the speed of light in a vacuum (3 x 10^8 ms^{-1}) and t is the round-trip transit time (in seconds). A permittivity value of ϵ_r = 2.2 was used for a depth of 20 m, as derived from hyperbolic diffractions (Arcone and Delaney, 2000; Arcone and others, 2016). This value corresponds to an effective average density of 0.58 kg m^{-3} (Kovacs and others, 1982). To reduce data volume and increase the signal-to noise ratio, I stacked the radar data by averaging adjacent traces together in sets of three. Spatial accuracy before stacking was ∼0.2 m per trace with a maximum error of ∼0.4 m after stacking. A broadband finite-impulse response filter was applied to the stacked transects to alleviate high-frequency noise and low-frequency modulation (Arcone and others, 2016; Campbell and others, 2017).

2.2.2 Velocity Datasets

Kinematic outputs were derived from multiple velocity datasets including MEaSUREs2 and JPL auto-RIFT (Gardner and others, 2018; Rignot and others, 2017). The MEaSUREs2 velocities were derived using speckle tracking and interferometric phase analysis using RADARSAT-1, RADARSAT-2, ERS-1,ERS-2, and Sentinel-1 SAR platforms, and ENVISAT ASAR acquired from 1996-1997, 2000, and 2007-2016 (Rignot and others, 2017). In addition, JPL auto-RIFT velocities were derived using

feature-tracking techniques from Landsat 7 and Landsat 8 scenes acquired during periods of solar illumination (September-March) from 2013-2018 and have a temporal resolution of less than 48 days (Gardner and others, 2018). The MEaSUREs2 dataset was mosaicked as outlined by Rignot and others (2011) to produce a 450 m-resolution velocity map with uncertainties of $\sim$3 m yr^{-1} in both x and y directions. The auto-RIFT dataset provided by Gardner and others (2018) produced yearly velocity maps from 2014–2017 at 250 m resolution with uncertainties of 20-30 m yr^{-1} for individual velocity estimates. Both datasets were produced in the Antarctic Polar Stereographic projection (EPSG 3031) with true scale at 71° S. Temporal variations of the auto-RIFT velocities were comparable to the magnitude of uncertainty and therefore short-term seasonal variations were considered insignificant.

I created gridded estimates of the ice velocity components using a Kriging algorithm (Surfer® 16 from Golden Software, LLC; after Abramowitz and Stegun 1972) that predicts the value of a function at a given point by computing a weighted average of the known values of the function in the neighborhood of the point. I then calculated the local spatial derivatives in ice velocity ($\frac{\partial V_x}{\partial x}$,$\frac{\partial V_x}{\partial y}$,$\frac{\partial V_y}{\partial x}$, and $\frac{\partial V_y}{\partial y}$) using neighboring pixels. $\frac{\partial V_x}{\partial y}$ and $\frac{\partial V_y}{\partial x}$ will hereafter be called "flow-parallel shear" and "flow-perpendicular shear", respectively. These terms are included for simplicity but it should be noted that they are not entirely accurate in that the flow direction changes slightly throughout the study region. While principal strain rates are typically used to assess where crevasses initiate, the overall ice flow direction in the MSZ is almost perfectly S-N oriented in the Antarctic Polar Stereographic projection. I therefore calculated shear strain rate ε (deformational component due to shear), vorticity rate ω (rotational component), and dilatation rate Δ (rate of change in area relative to original area) from the spatial derivatives using the following equations:

$$\varepsilon = \frac{1}{2}\left(\frac{\partial V_y}{\partial x} + \frac{\partial V_x}{\partial y}\right) \tag{2.2}$$

$$\omega = \frac{1}{2}\left(\frac{\partial V_y}{\partial x} - \frac{\partial V_x}{\partial y}\right) \tag{2.3}$$

$$\Delta = \left(\frac{\partial V_x}{\partial x} + \frac{\partial V_y}{\partial y} \right) \tag{2.4}$$

where the y-component of the velocity V_y(m yr^{-1}) was considered positive in the southward direction and the x-component of the velocity V_x (m yr^{-1}) was considered positive in the westward direction.

2.2.3 Crevasse Features

GPR records from shear zones can be difficult to interpret due to the complexity of features such as intersecting crevasses and cracking and folding stratigraphic layers. I therefore split features into two categories for analysis: 1) slot crevasses with distinct voids and in which diffractions emanate from the terminated strata along their walls and 2) less distinct crevasse features with evidence of sagging snowbridges and apparent voids but no distinct walls (Fig. 2.2). All other features were excluded.

For each feature, I estimated the thickness of the overlying snowbridge H and the maximum crevasse width W_{max}. H was quantified as the distance from the glacier surface to the strongest peak of the hyperbola overlying the void. W_{max} was calculated as

$$W_{max} = d \sin(\phi - \theta) \tag{2.5}$$

where d is the manually delineated width of the void (in meters), ϕ is the ice flow direction from the remotely-sensed velocity datasets (in degrees), and θ is the crevasse strike angle (in degrees). For slot crevasses, d was delineated as the distance between the peaks of the hyperbolas that emanate from crevasse walls; for crevasses that widen slightly with depth the maximum distance between hyperbolic peaks was used (i.e. bottom dashed light in Fig. 2.2 right). In the case of less distinct crevasse features which lack distinct walls, d was determined as the distance between terminated strata. I assume that these crevasses are actively forming within the study region and, as such, I use a strike angle of 45° to ice flow in Equation 5.

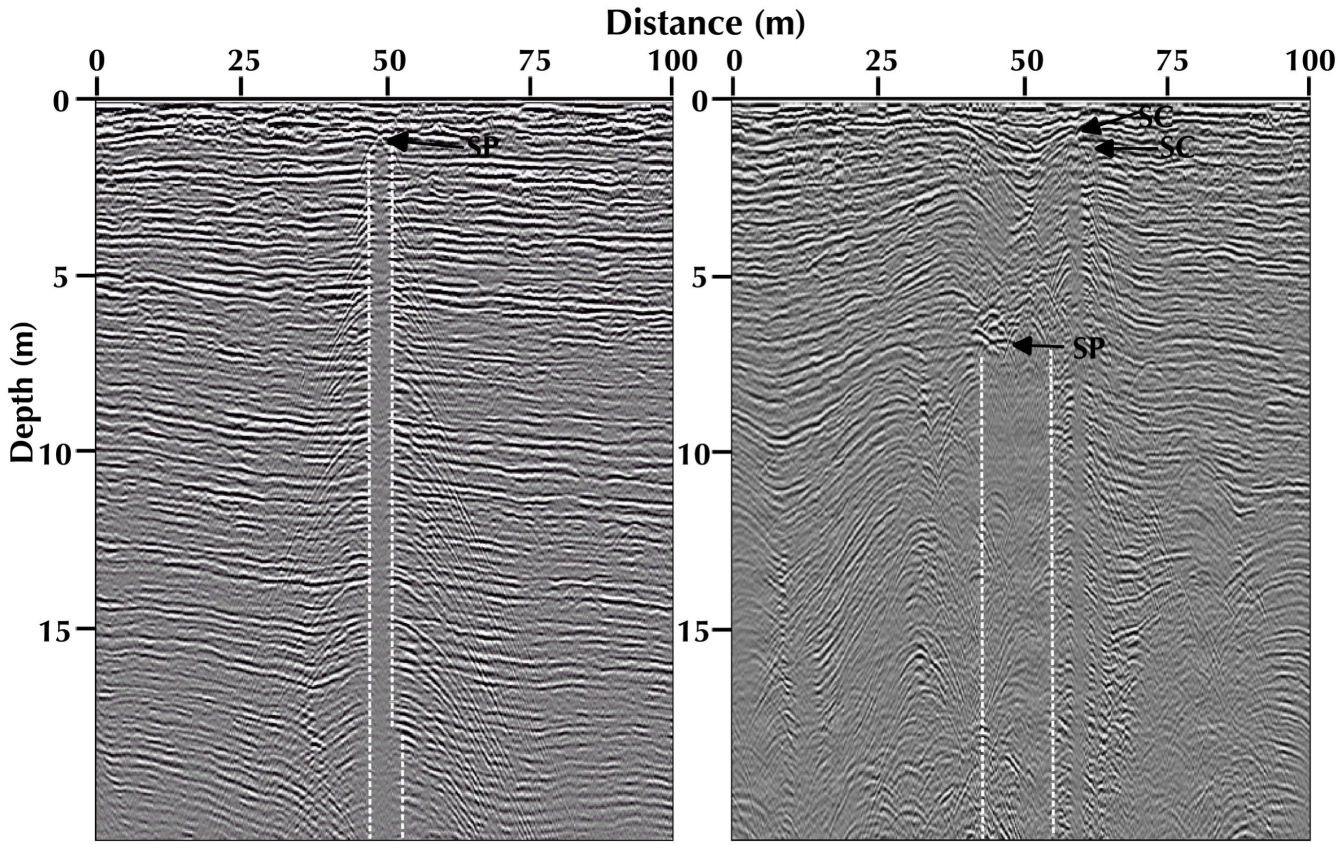

[h!]

Figure 2.2. Crevasse attributes from GPR. (left) 400MHz profile of a simple crevasse centered at 3.3 km along transect 21 in linear greyline format. The crevasse widens slightly at depth, with a maximum width of 5 meters. The arrow indicates the strongest peak ("SP") of the hyperbolic reflection which yields overlying snowbridge thickness of 1 m. Assuming a 45 ° strike angle would make it 0.7 m wide. (right) 400 MHz profile of a complex buried crevasse centered at 1.81 km along transect 2. The crevasse appears 13 m wide. The strongest peak ("SP") of the hyperbolic reflection yields an overlying snowbridge thickness of 5.5 m. Assuming a 45 ° strike angle would make it 9.3 m wide. Two additional simple crevasses ("SC") are noted with arrows.

2.2.4 Statistical Method and Normalization

To compare crevasse features and surface kinematics I overlaid crevasse locations on top of the kinematic maps and extracted the associated kinematic output values at each crevasse location. I found several instances in the GPR record of crevasses in echelon, the closest of which were spaced ∼5 m apart. I therefore up-sampled each kinematic output using a nearest neighbor approach in order to estimate the kinematic output every 5

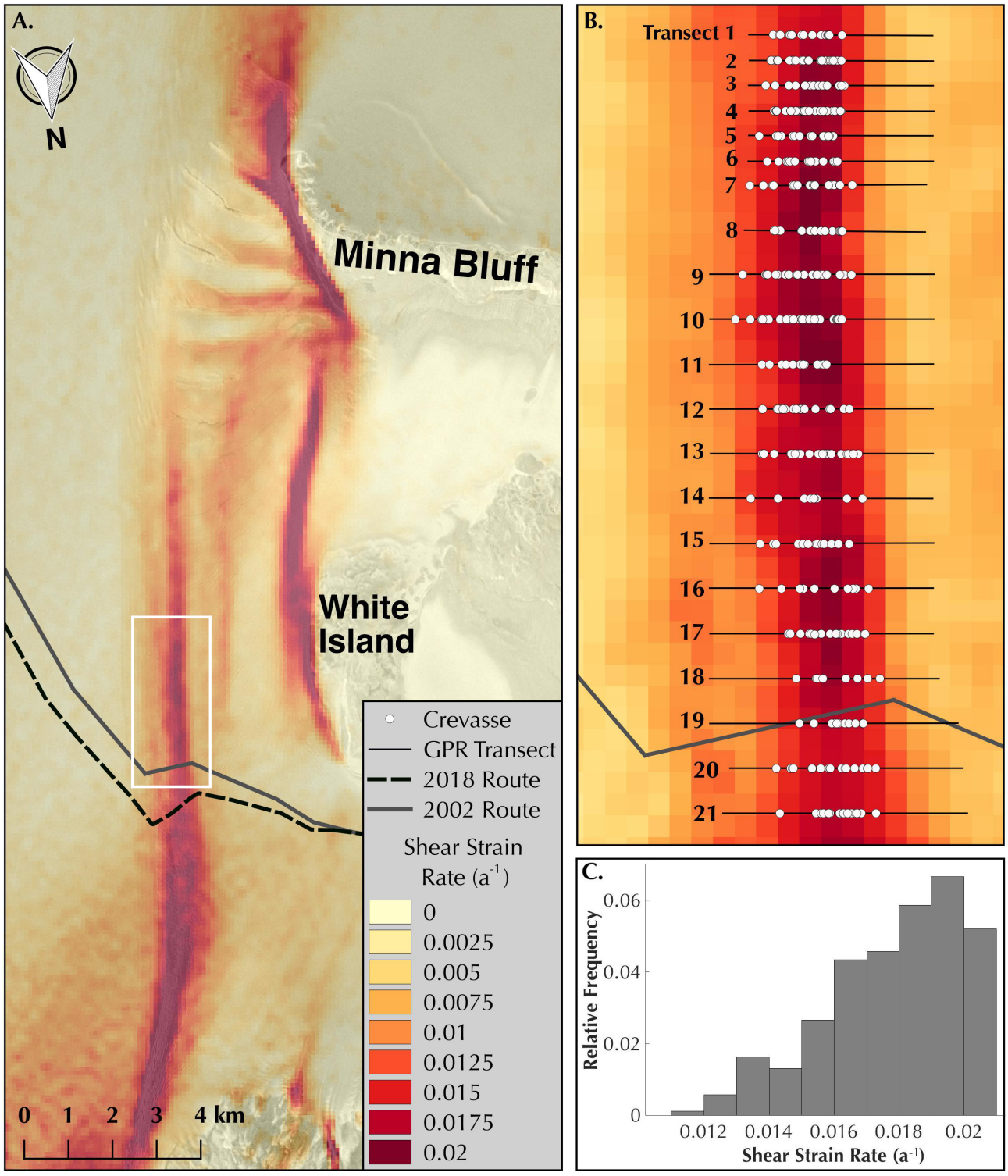

Figure 2.3. MSZ surface kinematics. (a) Gridded map of interpolated shear strain rate overlaid on Radarsat2 image. (b) Close-up of field area outlined in white in the overview panel. Grey lines indicate GPR transect routes with crevasses noted by white circles. (c) Plot of the relative frequency of crevasses with respect to shear strain rate.

meters along each transect and used this as the total number of observations. I then binned the kinematic data to identify differences in crevasse occurrence across the range of shear strain rate, vorticity, and dilatation observations. Bin sizes were determined using Scott's normal reference rule:

$$h = 3.5\left(\frac{s}{n^{\frac{1}{3}}}\right) \tag{2.6}$$

where h is bin size, s is standard deviation of the data, and n is the number of crevasse observations (Scott, 1979). The number of bins varied across different kinematic outputs but ranged between 9 and 15. I then computed the number of crevasses in each bin and normalized the data to account for differences in the total number of observations within each bin along the GPR transect paths. I normalized the data by dividing the number of crevasses for each bin by the total number of observations for each bin across the entire dataset to produce a relative frequency distribution of crevasses for each kinematic dataset (Fig. 2.3 ; Fig. 2.4; see also Appendix B).

2.3 Results

A total of 420 crevasse features were identified from the GPR dataset. 333 of these features were simple slot crevasses and 87 were less distinct features interpreted as crevasses. Results presented in this section include all crevasse features. Table 1 includes the range of values of shear strain rate, vorticity, and dilatation (derived from both the MEaSUREs2 and auto-RIFT velocity datasets) where crevasses were found.

Surface shear strain rates proved best for predicting crevasse features, with regions of higher shear strain rate more likely to have a greater number of crevasses (Fig. 2.4). Values of shear strain rate derived from the MEaSUREs2 velocity dataset range between 0.005—0.020 yr^{-1} in the surveyed area of MSZ, with crevasses located at a minimum of 0.011 yr^{-1}. Interpolated rates of vorticity also show a correlation with crevasse location with vorticity magnitude values between 0.006—0.022 yr^{-1} and crevasses located at a minimum of 0.013 yr^{-1}. Despite differences in horizontal resolution and time periods of

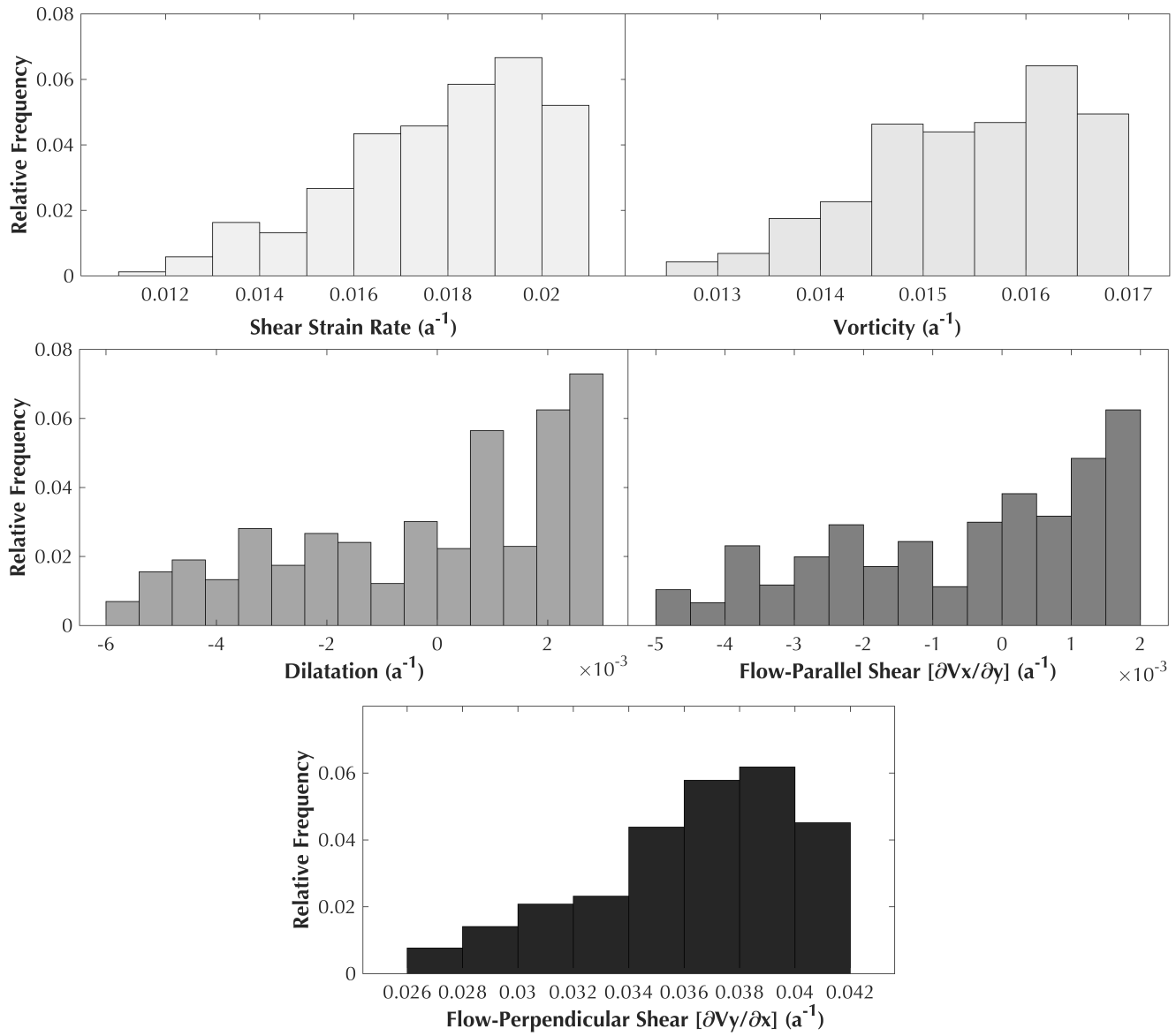

Figure 2.4. Relative frequency distribution plots from MEaSUREs2 velocity data. for shear strain rate, vorticity, dilatation, $\frac{\partial V_x}{\partial y}$, and $\frac{\partial V_y}{\partial x}$. Auto-RIFT plots are provided in Appendix A.

acquisition, threshold values for shear strain rate and vorticity, as well as the shape of their relative frequency distribution plots, show good agreement between the MEaSUREs2 and averaged auto-RIFT datasets (Appendix A). However, dilatation estimates did not agree well between datasets, therefore no clear threshold value could be identified. No distinct spatial patterns in crevasse width or snowbridge thickness were found. I also evaluated

Table 2.1. Range of values for kinematic outputs in m yr^{-1} derived from the velocity data where crevasses were found

Dataset	MEaSUREs2	auto-RIFT
Shear Strain Rate	0.011–0.020	0.012–0.021
Vorticity	0.013–0.022	0.013–0.023
Dilatation	-0.006–0.003	-0.008–0.005

Auto-RIFT values were averaged from 2014-2017. Frequency distribution plots for MEaSUREs2 outputs can be found in Fig. 2.3c and plots for auto-RIFT outputs are included in Appendix A.

each crevasse based on USAP's mitigation criteria for the MSZ region developed by the Cold Regions Research and Engineering Laboratory (CRREL): in order for a crevasse to be deemed safe to cross by a large tracked vehicle its maximum width cannot exceed the thickness of its overlying snowbridge (Lever, 2002). It is important to note that this criterion is only valid for the specific conditions of the MSZ. Based on this criterion I determined the crevasse width to snowbridge thickness ratio W_{max}/H, which I will call aspect ratio for simplicity, for each crevasse (Fig. 2.5). While the aspect ratio of a crevasse has no real physical meaning, evaluating this ratio is useful for identifying whether or not a crevasse will need to be mitigated by USAP (i.e. opened and filled with snow when $W_{max}/H > 1$) during future traverses. The crevasses show a pattern in which the relative aspect ratio of crevasses appears to increase in the southward direction.

2.4 Discussion

2.4.1 Implications for Crevasse Initiation

This analysis suggests that flow in the McMurdo Shear Zone is dominated by simple shear, as seen in the similarities between the relative distribution plots for flow-perpendicular shear, shear strain rate, and vorticity. While the shear strain rate threshold proved to be the best criterion for predicting crevasse initiation in my study region, the dominant causal mechanism for crevasse formation is stretching in one or more directions. However, because the area of interest is dominated by simple shear, the direction of stretching is defined as a function of the shear strain rate. In areas of complex

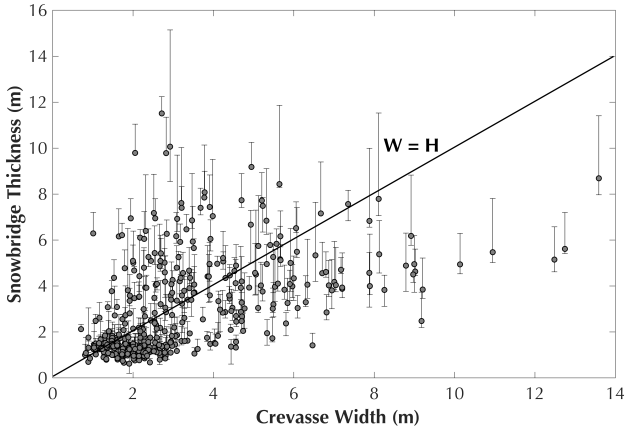

Figure 2.5. Size ratios of crevasse features. Snowbridge thickness was quantified as the distance from the glacier surface to the strongest peak of the hyperbola overlying the void. The minimum snowbridge thickness value was defined as the shallowest hyperbolic peak while the maximum thickness was defined by the top of the void. Crevasses below the solid diagonal line would require remediation according to USAP's crossing criterion.

shear, this would not be the case and a crevasse initiation threshold based solely on shear strain rate would be inadequate.

In theory, one could apply the derived shear strain threshold to velocity outputs from future modeling scenarios of the MSZ to qualitatively predict how the crevasse field will evolve over time. Such an analysis would be useful for both logistical purposes (i.e. to determine which regions will be the most crevassed in the future) as well as scientifically for predicting changes in back-stress due to either a decrease or increase in damage along the shear margin. However, crevasse initiation depends on density, crystallography, ice history, and temperature, all of which may evolve with the crevasse field; therefore, some caution should be used when applying this shear strain threshold to forward modeling.

2.4.2 Implication on Shear Zone Stability

Despite the clear evidence of a complicated history of ice deformation and fracture within my particular study site, the patterns from Fig. 2.5 and Fig. 2.6 provide some insight into the current stability of the region. While the concept of the aspect ratio was conceived for safety purposes and the term has no direct physical meaning, it provides a

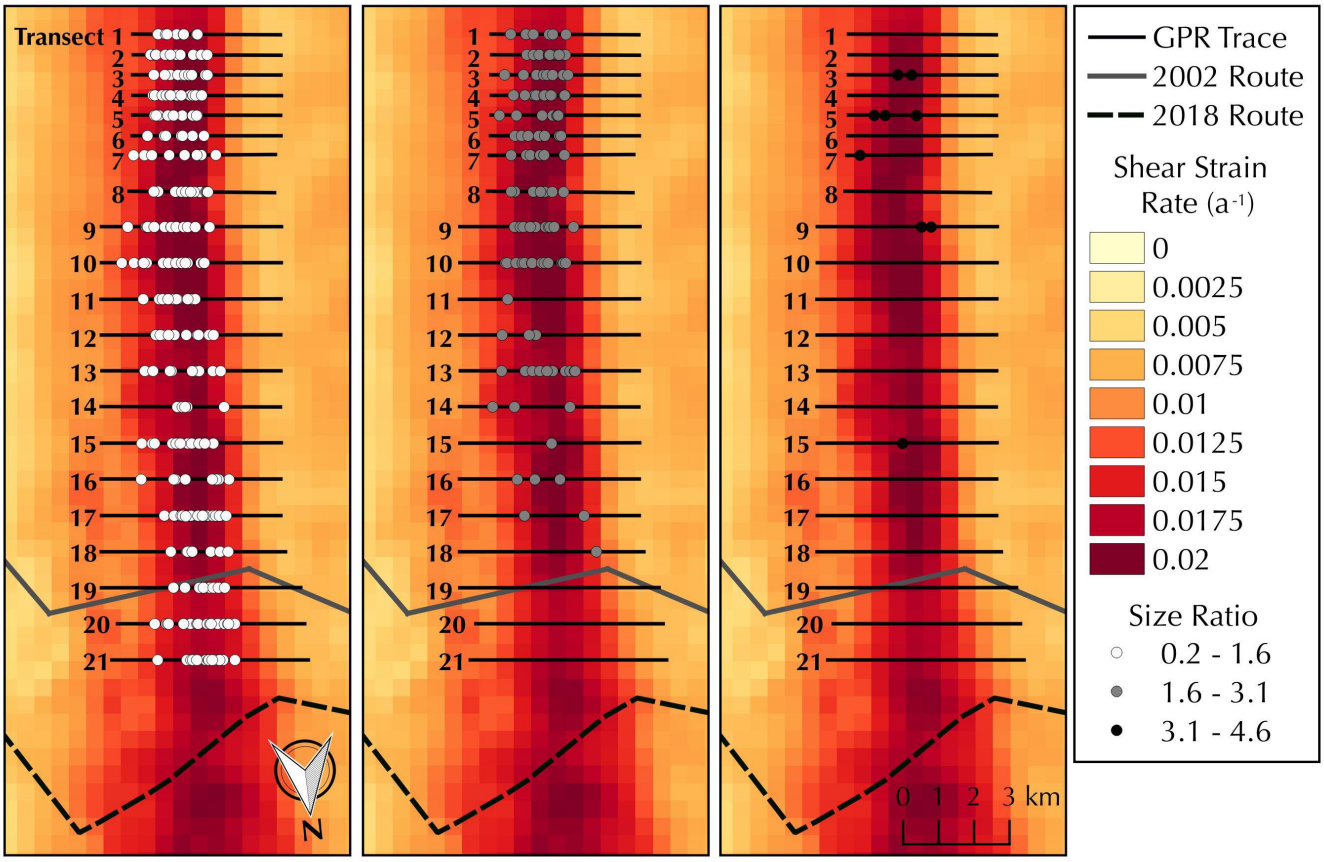

Figure 2.6. Spatial pattern of differing size ratios of crevasse features. The size ratio increases in the southward direction (i.e., crevasses are wider with respect to their snowbridge thickness in the southern part of the survey).

first order approximation of the ratio of the crevasse opening rate versus the accumulation rate in the snowbridge. I make two assumptions to arrive at this simplification: 1) the effect of snow compression due to bridging is negligible, and 2) crevasses form at the near surface. Although I cannot definitively rule-out that crevasses form at depth as discussed by Colgan and others (2016), most evidence for initiation at depth is from theoretical work (Nath and Vaughan, 2003; Van der Veen, 1999) or observations that are limited and/or unique in nature (Scott and others, 2010). For the MSZ region, the overwhelming majority of crevasse observations, including those from previous GPR campaigns that investigated to depths of ~170 m (Arcone and others, 2016), come from 0-20 m depth. Consequently,

the crevasses in the study region likely form near the surface. If I also assume accumulation rate to be relatively constant, whereas opening rate depends on the stress state of each crevasse, then each point on Fig. 2.5 indicates that particular crevasse's history. I thus interpret crevasses just above the horizontal axis of Fig. 2.5 to be the youngest, because they are opening at a faster rate than they can be buried. Conversely, crevasses with thick snowbridges are interpreted as older. The lack of wide, deep crevasses (top right of the spectrum in Fig. 2.5 could indicate few relict crevasses, and that older crevasses have healed. Data in the top left of Fig. 2.5 may be an example of older crevasses that have partially healed.

While I did not find a strong spatial pattern in crevasse width or snowbridge thickness, the aspect ratio appears to increase in the southward direction (i.e., crevasses are wider with respect to their snowbridge thickness in the southern part of the survey, as seen in Fig. 2.6.This pattern could be due to several different reasons:

1. my initial assumption of a spatially constant accumulation rate is inaccurate and in fact there is a pronounced increase in accumulation rate toward the south,

2. crevasses have a greater opening rate toward the south,

3. crevasses are opening quickly in the south and then healing as they advect northward and I only see newer, thinner crevasses on top, and/or

4. there is a transient effect where crevasses are staying open for a longer period of time in the southern portion of the survey.

While local variations in accumulation rate are likely, I have found little evidence to support scenario 1. RACMO accumulation rate values are lower in the southern portion of the survey (Van de Berg and others, 2006), while estimates from Arthern and others (2006) have the opposite spatial pattern with slightly higher estimates in the southern portion (on the order of mm). Scenario 2 is certainly plausible as the shear strain rate is generally

higher in the southern portion of the survey. Scenario 3 is unlikely as repeat GPR surveys performed by SPoT from 2002-2016 along the road show little indication of crevasse healing, with all monitored crevasses continuing to widen from year to year. Scenario 4 would indicate the region is not in steady state and is in fact, changing over time.

Recent changes in ice flux have been observed both upstream and downstream of the McMurdo Shear Zone that could affect the stress balance distribution within the region. Most notably, between 2016 and 2017 a previously inactive rift at the edge of the MIS widened and propagated over 3 km and eventually led to the calving of a 14 km^2 tabular iceberg (Banwell and others, 2017). GPS- velocity measurements from 2016-2017 in the vicinity of the rift indicated a distinct change in direction in the wake of the calving event (MacAyeal, personal communication; see also Banwell and others, 2019). These observed changes along the MIS front represent an important perturbation of the downstream boundary condition that could alter longitudinal stresses and velocity patterns within the MSZ. For example, this calving event could potentially drive longitudinal extension along the MIS due to a reduction in back-stress at the calving front. This in turn could cause a widening of the shear zone. Thus, both scenarios 2 and 4 seem the most likely and further observations of temporal variations in the spatial pattern of the aspect ratio are needed to definitely assess whether deviations in the flow field from steady state have an appreciable influence on crevasse opening and closure.

2.4.3 Viability of the South Pole Traverse

Since its creation in 2002, the South Pole Traverse route has advected ∼4 km at its western edge and ∼6 km at is eastern edge. The traverse route is now located in a region where the shear zone is wider. In addition, it has rotated ∼40° and stretched ∼1 km lengthwise, causing a greater portion of the traverse to be in a region that exceeds the threshold shear strain rate for crevasse initiation. Crevasse mitigation efforts have become more time-consuming as the number of crevasses that need to be mitigated have increased

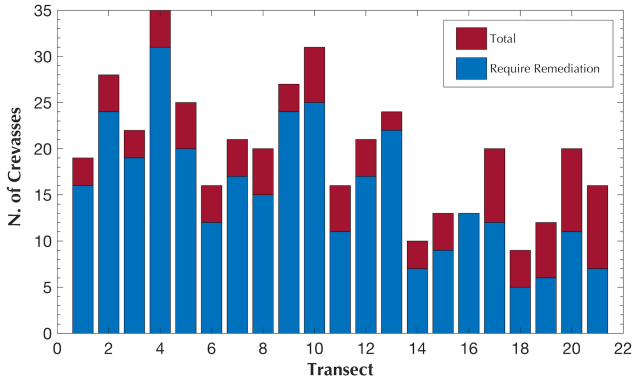

Figure 2.7. Observed and predicted crevasses for each GPR transect. Bar graph of the total number of crevasses located along each transect as well as number of crevasses that would require remediation based on USAP's crossing criterion.

and USAP currently has plans to create a new route. This would suggest that the relative aspect ratio of crevasses along the road has increased over time, which is counter to my observations where the relative aspect ratio of crevasses appears to decrease in the northward direction. This discrepancy may be due to the fact that even the northern-most survey line is ∼3.2 km to the south of the center of the current route crossing location and ∼1 km north of where ice begins to flow around White Island and into the McMurdo Ice shelf. I therefore have limited observations of crevasses in this region where there is a considerable added effect from the flow-parallel shear component of the velocity field.

I identified the two most viable route locations between transects 14 and 15 and between transects 18 and 19 called Route 1 and 2, respectively. These two areas are located at local minima of both shear strain rate (Fig. 2.6) and the number of crevasses that would require remediation (Fig. 2.7) and were placed perpendicular to flow. To identify the ideal route from these two options, I advected the two routes over the next 20 years using the average velocity field from MEaSUREs2 and annually extracted the shear strain rate along each yearly route position (Fig. 2.8). To provide a first order estimate of the number of crevasses along each route, I multiplied the relative frequency of crevasses from the distribution plots by the shear strain rate at 5 m spacing and summed the result

(Fig. 2.9). I also compared the percent of the crossing that would be above the shear strain threshold for crevasses, which I estimate as 0.011 yr^{-1} from my observations.

Analysis of my dataset suggests the best location for a new route would be Route 1, approximately ∼9.3 km south of the midpoint of its current position and ∼4.3 km south of the midpoint of its original location in 2002. This potential route would advect through a narrower portion of the shear zone than Route 2, which is located just to the south of where the shear zone begins to widen drastically due to the added component of flow-parallel shear as ice flows past the tip of White Island. In addition, Route 2 would likely be more susceptible to far field changes along the MIS front. I therefore believe the traverse crossing would require less mitigation in the long-run if it is moved to the location of Route 1.

2.5 Conclusions

This analysis suggests that flow in the McMurdo Shear Zone is dominated by simple shear and that crevasse initiation typically occurs when the shear strain rate exceeds a value of 0.011 yr^{-1} and vorticity magnitude of 0.013 yr^{-1}. Shear strain rate appears to be the best indicator for predicting crevasse locations, with regions of higher shear strain rate more likely to have a greater number of crevasses. The depth of snowbridge thickness and/or width of crevasses in the McMurdo Shear Zone do not appear to correlate with the shear strain rate and/or vorticity. However, the aspect ratio of individual crevasses decreases in the northward direction of ice flow so that there are fewer wider and shallower crevasses towards the northern limit of my study site.

Although the method presented here provides a means to infer the presence or absence of crevasses in lateral shear zones with high-frequency radar observations, there are still several limitations to this method. First and foremost, the radar transects discretely sample the crevasse field and it is nearly impossible to identify all of the crevasses within each transect using either automated or manual methods. The spatial resolution of the radar data, as well as the remotely-sensed velocity data, may influence the derived crevasse

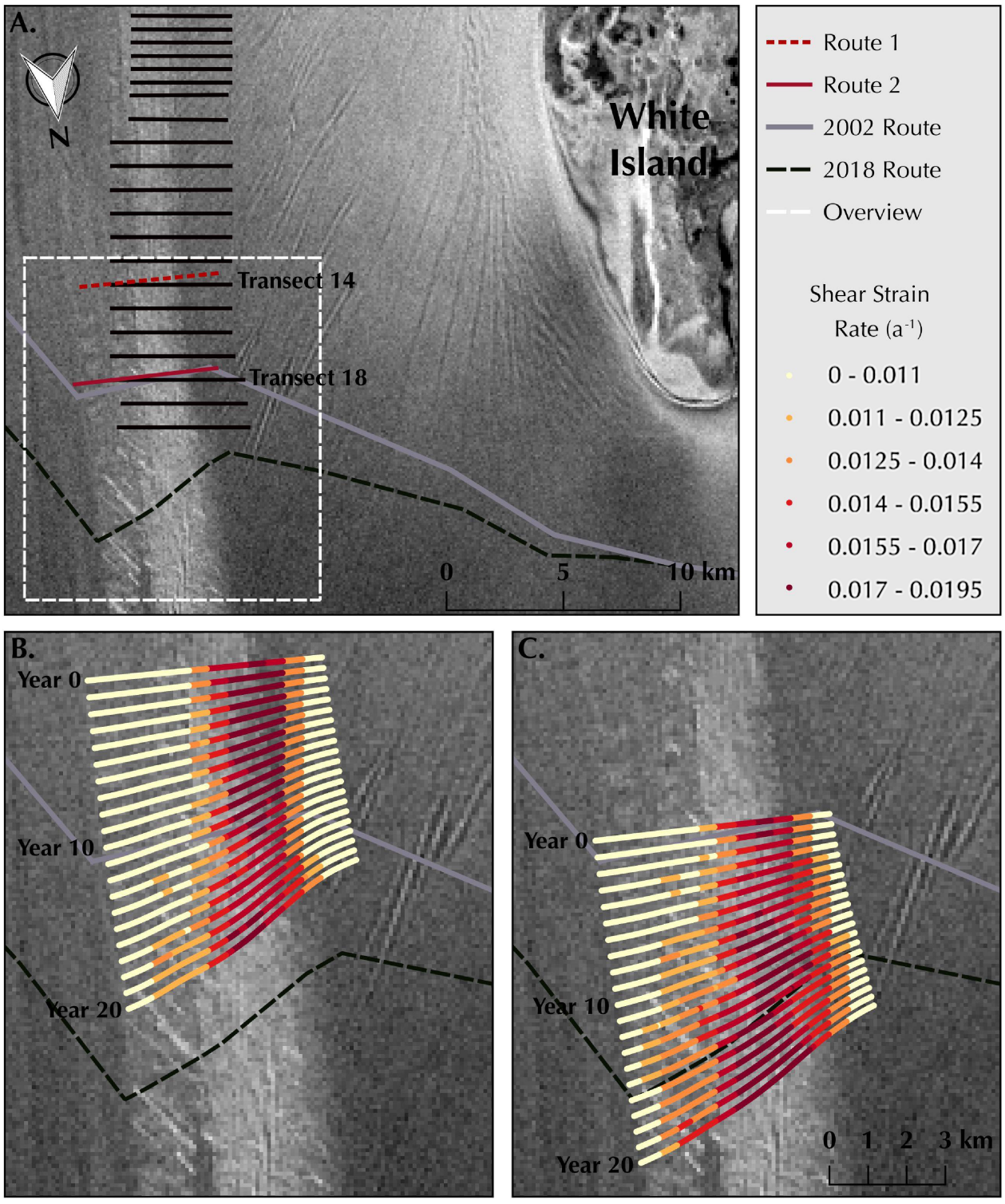

Figure 2.8. Future advection of potential SPoT routes and associated shear strain rate through time over 20 years. (a) Radarsat2 image of the MSZ area. Potential Route 1 and 2 noted by dashed and solid red line, respectively.(b) Location and shear strain rate of Route 1 throughout advection (c) Location and shear strain rate of Route 2 throughout advection.

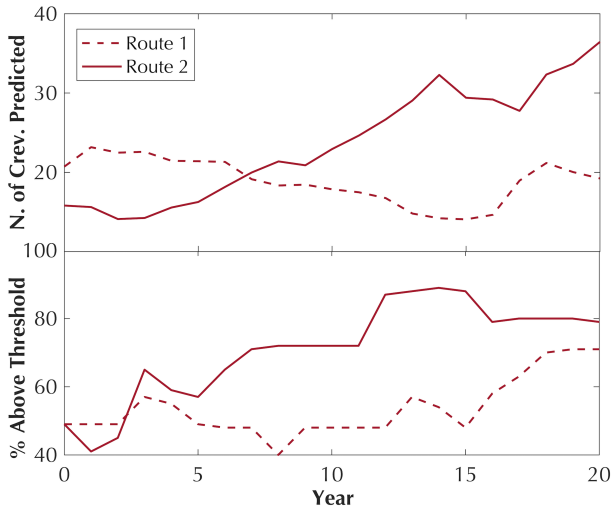

Figure 2.9. Predicted number of crevasses encountered along potential SPoT routes (top) Number of crevasses predicted for Route 1 and 2 as they advect 20 years. (bottom) Percent of route above a shear strain threshold of 0.0114 yr^{-1}.

initiation threshold. The quality and spatio-temporal sampling of the velocity dataset will also influence the analysis.

As previously stated, crevasse initiation depends on several factors including ice temperature, density, crystallography, and ice history. Therefore, the threshold values derived for the MSZ cannot be directly applied to other glacial environments. However, a similar shear strain threshold value should be applicable in other areas dominated by simple shear, and the method provided here can be repeated to find other kinematic threshold criteria for more complex shear margins, to study shear margin evolution, and to assess localized damage and weakening processes in locations using minimal *in-situ* data.

CHAPTER 3

ROSS ICE SHELF DYNAMICS AS A FUNCTION OF ICE THICKNESS

3.1 Introduction

Ice shelves fringing most of Antarctica's coastline provide resistance to ice flow from the Ice Sheet interior and control the rate of ice discharge into the ocean. As over 70 percent of the Antarctic Ice Sheet drains into ice shelves (Pritchard and others, 2012), understanding controls on ice shelf stability is critical to predicting the future evolution of the Antarctic Ice Sheet (AIS) and subsequent sea level rise. Factors influencing ice-shelf stability include surface mass balance (Banwell and MacAyeal, 2015; DeConto and Pollard, 2016), basal melt and freeze-on (e.g. Alley and others, 2016; Craven and others, 2009), ice shelf fracture and suturing processes (Jansen and others, 2013; Kulessa and others, 2014), and lateral ice shelf buttressing due to contact with land or adjacent slower moving ice (Favier and others, 2016; Reese and others, 2018). The loss of buttressing due to submarine ice melt or ice shelf collapse can considerably alter the stress balance distribution of tributary glaciers and result in long term acceleration of grounded ice (Glasser and Scambos, 2008; Rott and others, 2011; Khazendar and others, 2015).

Ice shelves are particularly vulnerable to changes along their lateral shear margins. Full thickness rifting often originates in these regions of high stress before propagating across ice shelves and leading to calving events, such has been seen at Pine Island Glacier and the Larsen C Ice shelf (Alley and others, 2016; Jansen and others, 2013). Thinning within shear margins increases their susceptibility to fracture and crevassing, which reduces the load-bearing surface area and lateral drag provided by the ice shelves. Shear margin weakening can be exacerbated by the formation of basal troughs. Recent work by Alley and others (2019) has shown that buoyant plumes of warm ocean water beneath ice shelves is preferentially focused into these basal troughs, leading to localized melting, further weakening of the margin, and loss of buttressing.

Buttressing is heavily influenced by changes in ice thickness; modeling studies suggest that ice flux across the grounding line is particularly sensitive to of localized ice-shelf thinning (Reese and others, 2018; Zhang and others, 2020).Therefore, models that aim to assess the importance of buttressing on dynamics must be informed by accurate ice thickness. Estimates of ice shelf thickness critically depend on the density of the overlying firn, underlying marine ice, and accurate measurements of freeboard (i.e. height above floatation). However, before the release of the MEaSUREs BedMachine Antarctica dataset in 2019 (Morlighem and others, 2020), large-scale ice shelf models have typically relied on Bedmap2 data to initialize model geometry (Fretwell and others, 2013). Ice thickness grids of Antarctic ice shelves within the Bedmap2 model, primarily derived from satellite altimetry (Griggs and Bamber, 2011), are estimated to have overall uncertainties of +/- 150 m (Fretwell and others, 2013). In addition, ice shelf shear margin geometries are poorly constrained for two reasons: 1) firn densification due to horizontal divergence is not accounted for in the model used for firn-correction (Van den Broeke, 2008); *in-situ*studies have shown the firn column to be 30 m thinner within shear margins of ice streams in northeast Greenland than estimates from this simplified firn model (Christianson and others, 2014; Riverman and others, 2019). 2) The effect of marine ice, both widespread beneath ice shelves and believed to have particularly large accretion rates within suture zones (Jansen and others, 2013), was not accounted for in thickness estimates. Taken together, these findings suggest *in-situ* thickness estimates are sorely needed in the previously poorly constrained lateral margins along Antarctic ice shelves.

For the Ross Ice Shelf (RIS), an important region of lateral resistance is its western lateral margin, a ∼140 km section of ice spanning between the rock outcrop Minna Bluff and Ross Island. A weakening of this lateral margin might destabilize the RIS, as has been observed and modeled on smaller ice shelves (Vieli and others, 2007; MacGregor and others, 2012; McGrath and others, 2012). Most notably, modeling work by Reese and others (2018) predicts that a moderate thinning of ∼1 m in this region can have

far-reaching effects, including an immediate acceleration of the Bindschadler and MacAyeal ice streams located more than 900 km away.

In this study, I present estimates of ice thickness based on (1) *in-situ* GPR observations and (2) surface elevation observations along a portion of the western lateral margin of the Ross Ice Shelf known as the McMurdo Shear Zone (MSZ). I then explore how uncertainties in ice thickness within this region influence mass flux across the grounding line. To do so, I utilize the Ice Sheet System Model (ISSM; Larour and others (2012)) to explore both instantaneous transient effects of localized thinning and associated sea level rise.

3.2 McMurdo Shear Zone Structure and Thickness

This study focuses on a portion of the western lateral margin of the Ross Ice Shelf known as the McMurdo Shear Zone (MSZ), formed where the relatively fast ice of the Ross Ice Shelf ($\sim$450 ma^{-1}) shears past the slower moving ice of the neighboring McMurdo Ice Shelf ($\sim$200 ma^{-1}). Kinematically, the MSZ is dominated by simple shear (Kaluzienski and others, 2019), creating a 5-10 km wide zone of intense crevassing that stretches from Minna Bluff to Ross Island (Fig. 3.1). Changes in ice flux both upstream and downstream of the MSZ that could affect the stress balance distribution and overall stability of the region have been observed over the last decade. Most notably, a calving event at the edge of the MIS produced a 14 km^3 tabular iceberg in 2017 (Banwell and others, 2017), representing an important downstream perturbation that could alter longitudinal stresses and velocity patterns within the MSZ due to a reduction in back-stress at the calving front. A detailed analysis of crevasse size ratio (i.e, comparison of crevasse width to snowbridge thickness) and spatial distribution indicates the region may not be in steady state due to a transient effect where crevasses remain open for a longer period of time in the southernmost portion of the shear zone (Kaluzienski and others, 2019).

Ground penetrating radar (GPR) observations have been carried out in the MSZ on a yearly basis since 2002, when the United States Antarctic Program created the South Pole

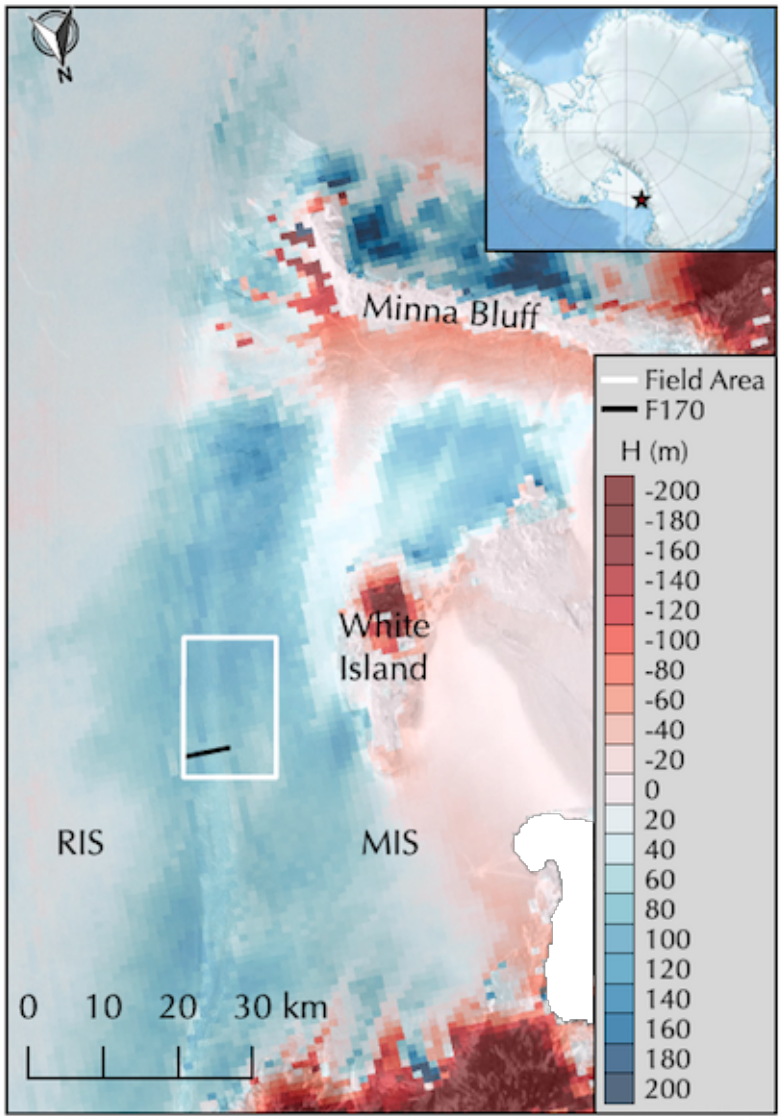

Figure 3.1. Map of ice thickness difference between BedMachine and Bedmap2 along MSZ. Location of field study area is outlined in white. Location of GPR transect F170 from Arcone et al., 2016 (Fig. 3.2) noted by black line.

Traverse route to cross the shear zone. GPR observations collected in 2014 and 2015 reveal a top to bottom structure of ∼40 m of firn, ∼120 m of meteoric ice, and at least 20 m of stratified marine ice before losing signal, indicating the ice is at least 180 m thick (Arcone and others, 2016). Observations of the marine ice transition layer at ∼160 m depth are over three times thicker than Bedmap2 ice thickness estimates within the region, and slightly thicker than Bedmachine estimates (Figs. 3.1 and 3.2). As previously

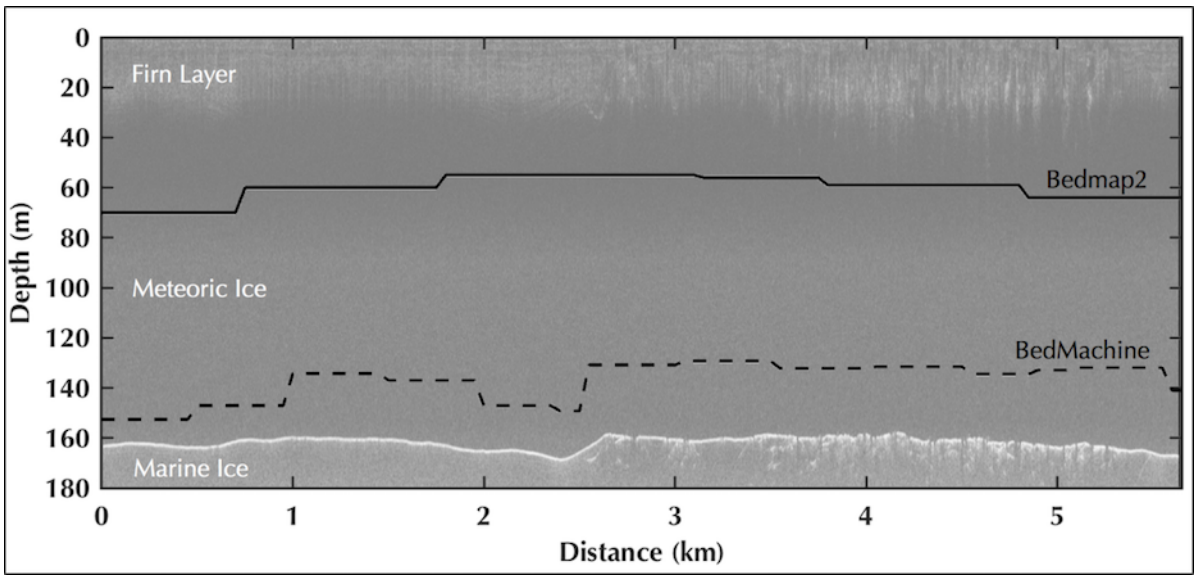

Figure 3.2. Comparison of GPR observations of ice thickness with remote sensing datasets. 200MHz profile of 5.7 km transect collected transverse to the MSZ in 2015 (Transect F170, Arcone et al., 2016) in linear greyline format. Ice thickness estimates from Bedmap2 and BedMachine are shown for the same location

acknowledged, underestimates of ice thickness in shear margins are likely due to an exclusion of the effects of shear-induced firn densification and paucity of knowledge of marine ice location and density. GPR observations from Arcone et al. 2016 reveal folded strata within the firn layer across the MSZ believed to be caused by a combination of the east-west compression against the McMurdo Ice Shelf as well as shear (Arcone and others, 2016). The relative dielectric permitivities used to calibrate depth in the 2016 study were derived by matching the recorded GPR hyperbolic diffractions with modeled parabolas and ranged between 2.17–2.34 (Arcone and others, 2016). These values correspond with average firn densities for the top 10 m of 560–630 kg m^{-3}. This range of densities is similar to the only firn measurements ever recorded in the MSZ, those of (Lever, 2002) which found an average density of 500 kg m^{-3} from a 2 m-long core from a snowbridge taken in 2001. These densities also exceed even the densest profiles ever measured for ice shelf firn, that of Stuart and Bull (1963), who did not reach a density of 630 kg m^{-3} until a depth of 10 m in an area of compression near Scott Base on the nearby McMurdo Ice Shelf.

Full thickness GPR measurements (i.e, penetrating to the bottom of the ice shelf) are difficult in regions with thick marine ice layers due to saline content which results in high absorption losses and low bottom reflectivity. Similarly, airborne radio-echo-sounding measurements have failed to penetrate the full depth of the marine ice layer along the Filchner-Ronne Ice Shelf (Lambrecht and others, 2007) and along Larsen Ice Shelf C Luckman and others (2012); Jansen and others (2013). Direct observations of marine ice thickness have been limited to single ice-core drill holes at spot locations for the Ronne-Filchner (200–400 m; Oerter and others (1992); Thyssen and others (1993); Blindow (1994)) and the Amery (190 m; Craven and others (2005, 2009)) ice shelves. No significant drill measurements have been made on the Ross Ice Shelf, other than the 6 m found at the southern end (Zotikov and others, 1980). Well-informed estimates of the thickness of the marine ice layer are therefore lacking in many locations, despite their importance for deriving accurate estimates of the full thickness of the ice shelf as well as the relative importance of marine ice on shelf dynamics.

3.3 GPR Data and Ice Thickness Solution

I analyzed ∼30 km of 100 and 200 MHz frequency ground penetrating radar data collected within the MSZ in October of 2017 as well as data from Arcone and others (2016) that was collected further south of my survey in 2014. I autopicked bright horizons at depth interpreted to be the transition layer between meteoric and basal marine ice. A mosaicked Digital Elevation Model was constructed from Worldview images between December 2013- January 2014 to inform more accurate elevation estimates with respect to GPR transect locations. I then used these elevation and meteoric-marine ice interface estimates to solve for the total thickness of the ice column assuming the ice was in hydrostatic equilibrium. Details of the methods used to process and analyze the GPR and DEM datasets follow as well as details on the various density assumptions for firn, meteoric ice, and marine ice follow.

3.3.1 GPR Collection and Processing

A GSSI SIR30 control unit and model 5100 and 3207 100 MHz and 200 MHz antenna units were used to record 20 traces s^{-1} over time ranges of 2600 ns and 2900 ns, respectively. Data were recorded at 4096 32-bit sample/trace with a time variable gain. Two four-wheel-drive battery-powered rovers (Yeti; Trautmann and others 2009, and Scotty; Lever and others 2013), a later adaptation of Yeti's design) were used to tow two separate GPR systems (to cover more ground) at a constant speed of $\sim$1.5 m s^{-1}. Each rover was coupled with a Garmin-19x GPS system and followed waypoints along 21 preplanned transect routes designed to investigate crevasse distribution within the MSZ using a higher-frequency (400 MHz) antenna. Transect length and spacing were constrained by rover battery power capabilities under low temperatures as well as amount of time spent in the field. Fig. 3.1 illustrates 13 of the routes spanning $\sim$58 km where the 200 MHz antenna collected data in order to examine the inheritance of past rifting at the tip of Minna Bluff as well as the spatial distribution of marine ice accretion both within and alongside the MSZ. In addition, I compared the GPR record from this study to one transect from Arcone and others (2016) for consistency.

GPR transects were post-processed similar to previous work (Arcone and others, 2016; Kaluzienski and others, 2019). The travel-time to depth conversion ($d=ct/2\sqrt{\epsilon}$) was used to transform the round-trip transit time into thickness where ϵ is the dielectric permittivity (dimensionless), c is the speed of light in a vacuum (3 x 10^8 m s^{-1}) and t is the round-trip transit time (in seconds). I used ϵ= 3.0 as an initial guess for the full thickness calibration before manually delineating the meteoric- marine ice transition horizon in the radar profiles. I then analyzed hyperbolic features across transects 149, 154, and 360 and compared each hyperbolic arc with traced remigration trajectories to derive estimates of the dielectric constant. This allowed for a comparison of dielectric constant with depth as features were identified throughout the firm column. I then used the following equation

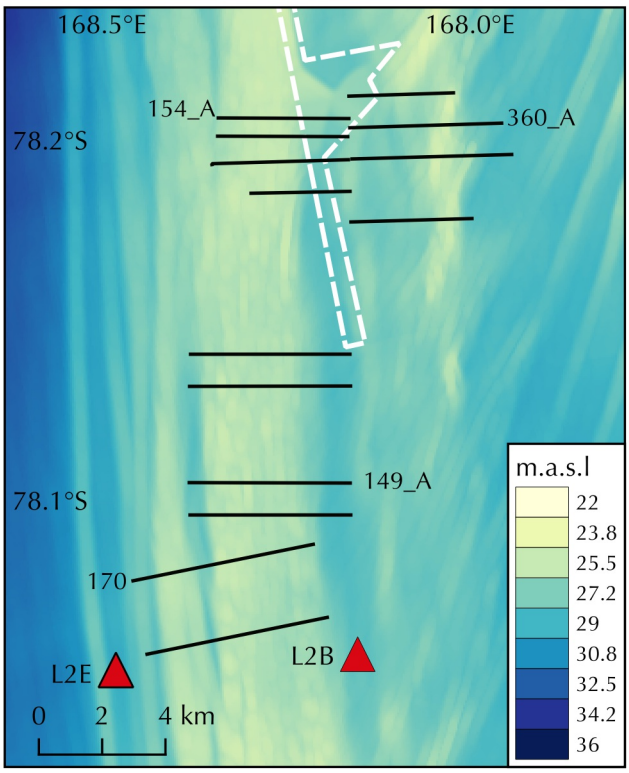

Figure 3.3. DEM of MSZ region and GPR transect locations. Worldview derived Digital Elevation Model of MSZ overview region from Fig. 3.1. White dashed line indicates gap in data coverage where interpolation was needed. Black lines illustrate GPR transect traces used for ice thickness estimation. Red triangles indicate GPS locations used for tidal signal analysis.

from Kovacs and others (1995) to convert the dielectric constant to density:

$$\epsilon = (1 + 0.845\rho) \tag{3.1}$$

where ρ is the density in kg m^{-3}. I then reassessed the marine ice transition depth using the two-way travel time and new dielectric constant estimate.

3.3.2 DEM Generation and Ice Thickness Solution

The NASA Ames Stereo Pipeline was utilized in order to construct a very high-resolution Digital Elevation Model at an initial 5 m horizontal resolution and ∼3 m vertical uncertainties (Enderlin and Hamilton, 2014; Shean and others, 2016) for three Worldview images collected from December 2013–January 2014. I then took the spatial

average of neighboring pixels in order to downsample each scene to 60 m spatial resolution, reducing the standard vertical error to ∼10 cm. I initially attempted to coregister the Worldview DEMs that included land coverage to the REMA dataset, but were unsuccessful due to a lack of overlap. I therefore coregistered an initial scene to tidally corrected elevation data derived from two GPS stations (Fig. 3.3; black and yellow triangles) which collected data over a period of 9 days in 2014 (2.13 m correction; Fig. C.1; see Appendix C for GPS field methods, data processing, and tidal correction). A 2D linear interpolation was used to fill-in data gaps in my region of interest (white dashed line Fig. 3.3). Uncertainties in elevation due to ocean dynamic topography were accounted for by subtracting 1.4 m from the mosaicked DEM (Padman and others, 2003) leaving the inverse barometer effect (∼1.2 m; Padman and others 2009) as the only significant source of error.

Assuming the ice is in hydrostatic equilibrium, the balance between the weight of the ice column versus the weight of displaced sea water is as follows:

$$\left(h_{f_1} + h_{f_2}\right)\rho_f + h_i\rho_i + h_m\rho_m = \rho_w\left(h_{f_2} + h_i + h_m\right) \tag{3.2}$$

Where h_{f_1} is the thickness of firn above sea level (i.e. freeboard), h_{f_2} is the thickness of firn below sea level, h_i is the thickness of meteoric ice, h_m is the thickness of marine ice, ρ_f is the average density of the total firn layer, ρ_i is the density of meteoric ice (assumed to be 917 kg m^{-3}), ρ_m is the density of marine ice (assumed to be 936 kg m^{-3} from Craven and others 2009), and ρ_w is the density of sea water (1028 kg m^{-3}). Solving for marine ice thickness, Eq. 3.2 can be rewritten as:

$$h_m = \left[\frac{h_{f_2}\left(\rho_w - \rho_f\right) + h_{f_3}\left(\rho_w - \rho_i\right) - h_{f_1}\rho_f}{\left(\rho_m - \rho_w\right)}\right] \tag{3.3}$$

3.4 Model Description and Initialization

I utilized the Ice-Sheet and Sea-Level System Model (ISSM; Larour and others 2012), a finite element thermomechanical model of ice flow, to explore instantaneous responses in

velocity to thinning along the western lateral margin of the Ross Ice Shelf. Subsequent transient simulations were carried out in order to study the evolution of the Ross Ice Shelf over a 25-year period and assess potential contribution to sea level rise. I tested three separate ice shelf geometry scenarios, the first initialized from Bedmap2, the second initialized from BedMachine, and the third initialized using a combination of BedMachine and interpolated thickness data from my *in-situ* derived ice thickness measurements (referred to as ISSM_{BM_2}, ISSM_{BM}, and ISSM_{IS} model suites, respectively).

3.4.1 Geometry and Parameterization

Table 3.1: Datasets used for model parameterization.

Datum	Source	Description
Grounded ice bed topography, ice thickness, and surface elevation	Fretwell and others (2013)	Bedmap2; gridded products derived from variety of sources including field surveys and altimetry estimates
Floating ice thickness and bed topography Scenario 1	Griggs and Bamber (2011)	Bedmap2; gridded products derived from variety of sources including field surveys and altimetry estimates
Floating ice thickness and bed topography Scenario 2	Morlighem and others (2020)	BedMachine version BedMachine Antarctica_2019-11-05_v01.nc; derived from conservation of mass
Floating ice thickness and bed topography Scenario 2	GPR measurements and Morlighem and others (2020)	Ice thickness estimates based on GPR surveys carried out in 2017

Continuation of Table 3.1		
Datum	Source	Description
Surface mass balance	Vaughan and others (1999)	Ice accumulation rate from SeaRISE version Antarctica5km _withshelves_v0.75.nc
Ice surface velocity	Mouginot and others (2019)	MEaSUREs Phase-Based Antarctica Ice Velocity Map Version 1
Ice surface temperature	Lenaerts and Van den Broeke (2012)	Ice surface temperature from RACMO2
Land mask	Bohlander and Scambos (2007)	Land mask from SeaRISE version Antarctica5km_withshelves _v0.75.nc
Initial basal melt rate	(Schlegel and others, 2018)	Ice shelf basal melt rates from Massachussetts Institute of Technology General Circulation model (MITgcm) run with high horizontal (9km) and vertical (150 levels) grid spacing. See Schodlok et al. 2016 for model methods
Geothermal heat flux	Maule and others (2005)	Basal heat flux from SeaRISE version Antarctica5km_withshelves _v0.75.nc

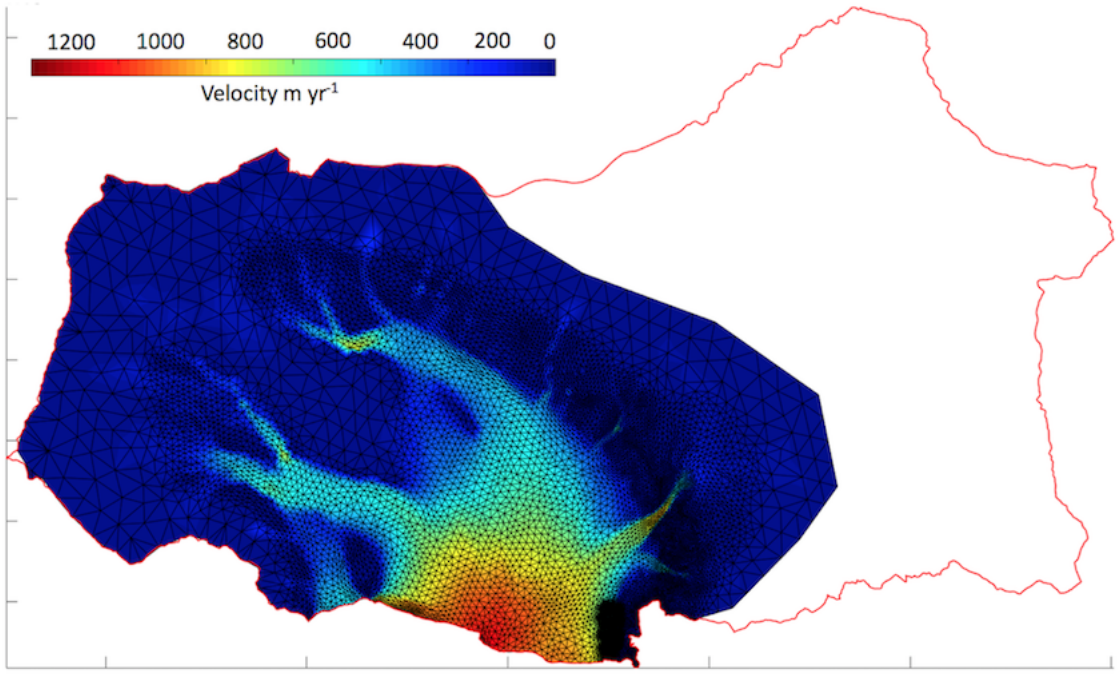

Figure 3.4. Overview of ISSM model domain and initialized velocity field. Red outline indicates full Ross Ice Shelf catchment area. Black overlay illustrates adaptive mesh refinement.

The model domain was first set to the Ross Ice Shelf catchment. To reduce computation time, I excluded the northwest portion in the region where ice flow is less than ~20 m yr^{-1} from my domain (See Fig. 3.4). I used an adaptive mesh with resolution varying between 16km and 3km. The mesh was refined through a fully automatic adaptive surface remeshing tool developed by Frey (2001). I adapted the mesh using both an effective strain rate map derived from MEaSUREs phase-derived velocity data (Mouginot and others, 2019) as well as a grounded ice mask derived from Bohlander and Scambos (2007). This refinement technique produced a final mesh of ~27,000 mesh elements with refinement within shear margins and along the grounding line. Grounded ice geometry was initialized from Bedmap2 while floating ice geometry varies for each of the three model geometry scenarios. Each model suite was initialized by the corresponding thickness dataset, and the ice-shelf surface and base were adjusted to assure hydrostatic equilibrium

according to the model densities for ice and sea water. Table 3.1 outlines all datasets used in the parameterization step.

For an initial temperature estimate, I computed the depth-averaged temperature accounting for both vertical advection and diffusion of heat into the base of the ice shelf as a function of surface temperature from the RACMO2 Regional Climate Model (Lenaerts and Van den Broeke, 2012), a basal temperature of 273.15 degrees K (i.e. freezing point), and basal melt rates from the Massachusetts Institute of Technology General Circulation model (MITgcm) runs by Schlegel and others (2018). This resulted in a depth averaged solution of Eq. 25 from Holland and Jenkins (1999):

$$T_I(z) = \frac{(T_S - T_B)\exp(\frac{-w_I z}{\kappa_I^T}) + T_B - T_S \exp(\frac{w_I H_I}{\kappa_I^T})}{1 - \exp(\frac{w_I H_I}{\kappa_I^T})} \tag{3.4}$$

Where T_I is ice shelf temperature, T_S is the surface temperature, T_B is the basal temperature, w_I is the vertical velocity of ice shelf, calculated from the melt rate, κ_I is the ice shelf thermal diffusivity, and H_I is the ice shelf thickness.

3.4.2 Thermal Steady-state Solution, Inverse Methods, and Model Relaxation

Table 3.2: Steps for model initialization. IHP stands for ice hardness parameter, HO stands for Higher Order Approximation, and SSA stands for Shallow Shelf Approximation.

Step	Input	Output	Extent	Stress Balance Approx	Portion of Domain
Rheology Inversion 1	IHP (initial guess from surface temperature), observed velocity	Depth averaged IHP for ice shelf, solved velocity for ice shelf	2D	SSA	Floating
Friction Inversion 1	Friction coefficient (initial guess based on surface slope), observed velocity on grounded ice, solved velocity on floating ice from IHP Inversion 1	Inverted basal friction (grounded ice)	2D	SSA	Floating and Grounded
Stress Balance	Observed horizontal velocities	3D velocity solution	3D	HO	Floating and Grounded
Thermal 1	Observed surface temperature	3D instantaneous temperature field	3D	n/a	Floating and Grounded

Continuation of Table 3.2					
Step	Input	Output	Extent	Stress Balance Approx	Portion of Domain
Thermal 2	Observed surface temperature, lateral boundary temperatures Thermal 1, 3D velocity field from Stress Balance 1	Improved 3D temperature field	3D	n/a	Floating and Grounded
Steady State	Observed horizontal velocities, vertical velocities from Stress Balance 1, observed surface temperature, lateral boundary temperatures from Thermal 2	Improved 3D temperature field	3D	HO	Floating and Grounded

Continuation of Table 3.2					
Step	Input	Output	Extent	Stress Balance Approx	Portion of Domain
Rheology Inversion 2	Ice hardness parameter guess from Cuffey approximation to depth averaged temperature from Steady State, observed velocity	Depth averaged IHP for ice shelf, solved velocity for ice shelf	2D	SSA	Floating
Friction Inversion 2	Friction coefficient (initial guess based on surface slope), observed velocity on grounded	Inverted basal friction	2D	SSA	Floating and Grounded

The majority of the model domain was ungrounded and no friction inversion was applied. The modeled velocities in this region were therefore particularly sensitive to the rheology inversion, which was in turn is sensitive to the initial temperature estimate. As large-scale ice temperature measurements of the RIS are non-existent, steps were taken to ensure the most reasonable model estimate of ice shelf temperature. This section outlines the iterative inversion and temperature solutions performed before the transient relaxation step. An outline of the sequence of steps and corresponding inputs and outputs can be found in Table 3.2.

I began the ice hardness inversion step with an initial inversion for the depth averaged ice hardness parameter B in Glen's flow law along the floating portion of the domain using the 2D Shallow Shelf Approximation (SSA, MacAyeal 1989). I refer the reader to Larour and others (2012) for a full description of ISSM's governing equations. A first guess for the ice hardness parameter was computed assuming the Arrhenius relation dependent on initial temperature following Cuffey and Paterson (2010). A second inversion for the basal friction coefficient k was then performed over the full domain using $\tau_b = -k^2 N v b$ (where τ_b is the basal stress magnitude, N is the effective pressure, and vb is the basal velocity magnitude) and setting friction equal to zero along the floating portion. The initial guess for the friction coefficient was based on the assumption that driving stress is equal to basal stress at any given point using the geometry of the grounded ice. As my main region of interest is a shear margin, I required an initial temperature field that takes into account horizontal advection. I was also interested in the advection of cold ice from the continent interior into the ice shelf and ultimately wanted a three dimensional transient thermal solution. The model was first extruded into three dimensions with ten layers of mesh using an extrusion exponent of 3 in order to refine the lower layers of the ice shelf and thus pay more attention to the temperature effects of the ice-ocean interface. I then solved a 3D Higher Order (HO; Blatter 1995; Pattyn 2003) stress balance solution to compute the vertical velocity component after specifying horizontal velocities from the MEaSUREs Phase-Based Antarctica Ice Velocity Map (Version 1).

While a full 3D transient thermal solution would be advantageous, it would be computationally intensive, and I was less interested in an accurate temperature field for the grounded portion of the domain which relies more on the friction inversion than the rheology inversion. I therefore solved an initial 3D thermal solution without advection after specifying the surface temperature from RACMO2, assuming basal temperatures to be at the melting point, and using basal melt rates from Schlegel and others (2018). This solution provided a 3D instantaneous temperature field that was used to specify lateral

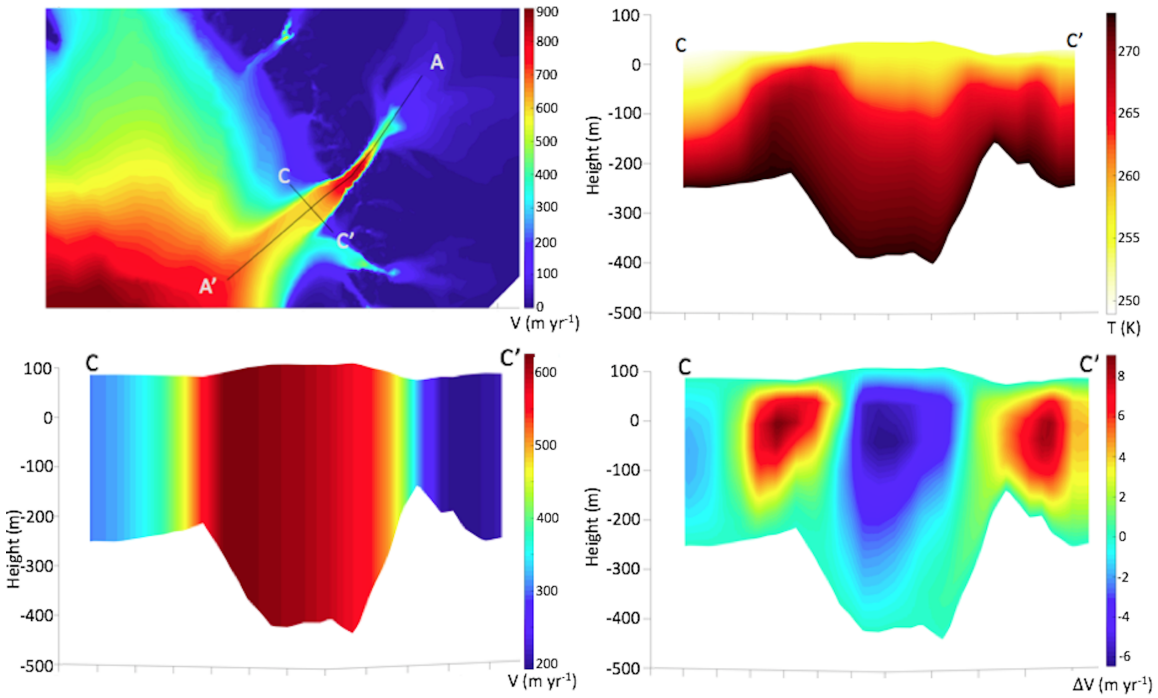

Figure 3.5. Comparison between ISSM Thermal Solution and Steady State Solution for the outflow of Byrd Glacier. Top Left) Ice velocity solution from Steady State Solution in ISSM. C to C' illustrates cross flow transect for outflow of Byrd Glacier. Top Right) Temperature after Steady State Solution for cross section across Byrd Ice Stream. Bottom Left) Cross section velocity in m yr^{-1}. Bottom Right) Difference in temperature between S illustrating the advection of colder ice from the continental interior and shear warming at the margins of the outlet flow of Byrd Glacier.

boundary temperatures for a second, thermal solution. In this second thermal solution, I specified 3D velocities from the earlier Stress Balance (note that the order of the initial thermal solution and stress balance solution does not matter). I then solved for a Steady State solution, again specifying initial velocities from MEaSUREs and implementing the Blatter and Pattyn HO flow law (Blatter, 1995; Pattyn, 2003) after specifying lateral boundary temperatures from Thermal Solution 2. I then collapsed the model back into two dimensions and depth-averaged the improved temperature field before repeating the rheology and friction inversion steps, this time implementing an L-curve analysis to minimize the misfit between model and observations and the regularizing term (Jay-Allemand and others, 2011).

Table 3.3. Model names and descriptions

Model Name	Description
ISSM_{BM2}	Ice shelf geometry initialized from Bedmap2
ISSM_{BM}	Ice shelf geometry initialized from BedMachine
ISSM_{IS}	Ice shelf geometry initialized from combination of BedMachine and interpolated ice thickness data from in-situ GPR observations

3.5 Ice Shelf Solutions

I organized the model runs into three separate suites, each initialized from a different ice thickness dataset along the floating portion of the domain (Table 3.2). Following the framework of Reese and others (2018), I first ran initial stress balance solutions for each model suite in order to explore how instantaneous changes in velocity resulting from localized thinning scenarios were sensitive to ice shelf thickness initialization. To do so, I ran the following two scenarios within each model suite: 1) a stress balance control run $\text{ISSM}_{SB_{control}}$ with no forcing and 2) a stress balance solution ISSM_{SB} where a 20 x 20 km region of the lateral margin is thinned instantaneously by 1 m.

Next, transient simulations were carried out, first by performing a relaxation step for each model suite in order to smooth out discontinuities between model fields following the previous inversion steps. However, I was interested in keeping initial geometries as close to the observed datasets for subsequent runs. I therefore only allowed the model to relax until the change in velocity between timesteps at each vertice was sufficiently small. A value of $<\sim$5m yr^{-2}, achieved after a model run of 5 years, was chosen to balance the trade-off between the velocity gradient between timesteps and the total relaxation time. A 25 year control run $\text{ISSM}_{control}$ was then run without an applied forcing for each model suite. I then investigated model transient response to localized thinning and spatial sensitivity along 5 different sectors–these will be referred to as case studies–along the shear margin over two separate 25 year transient simulations: 1) a thinning scenario $\text{ISSM}_{T_{thinning}}$ where

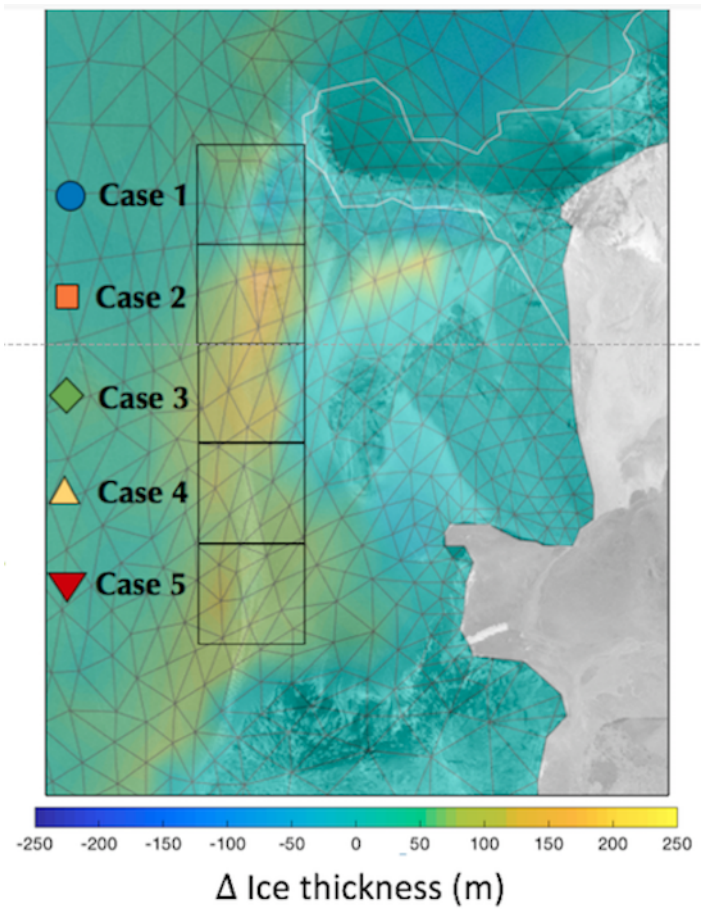

Figure 3.6. Comparison of ice thickness geometries. Close up of MSZ portion of model domain illustrating the difference in ice thickness initialization between ISSM_{IS} and ISSM_{BM2}, with outlines of model mesh and 20 x 20 km sections for each case study (shape and color for each case study used in Fig. 3.9

an initial amount of ice was removed from each sector and 2) a basal melt scenario $\text{ISSM}_{T_{basalmelt}}$ where a constant basal melt rate was implemented for each sector. For each transient simulation and case study, I applied 1 m, 2 m, and 3 m of instantaneous thinning (15 simulations in total). An additional 15 scenarios were run with basal melt rates of 1m, 2m, and 3m applied throughout the simulation. These 30 scenarios and basal melt rate forcings accounted for the range of previous melt rates estimated within the region (Adusumilli and others, 2020; Das and others, 2020).

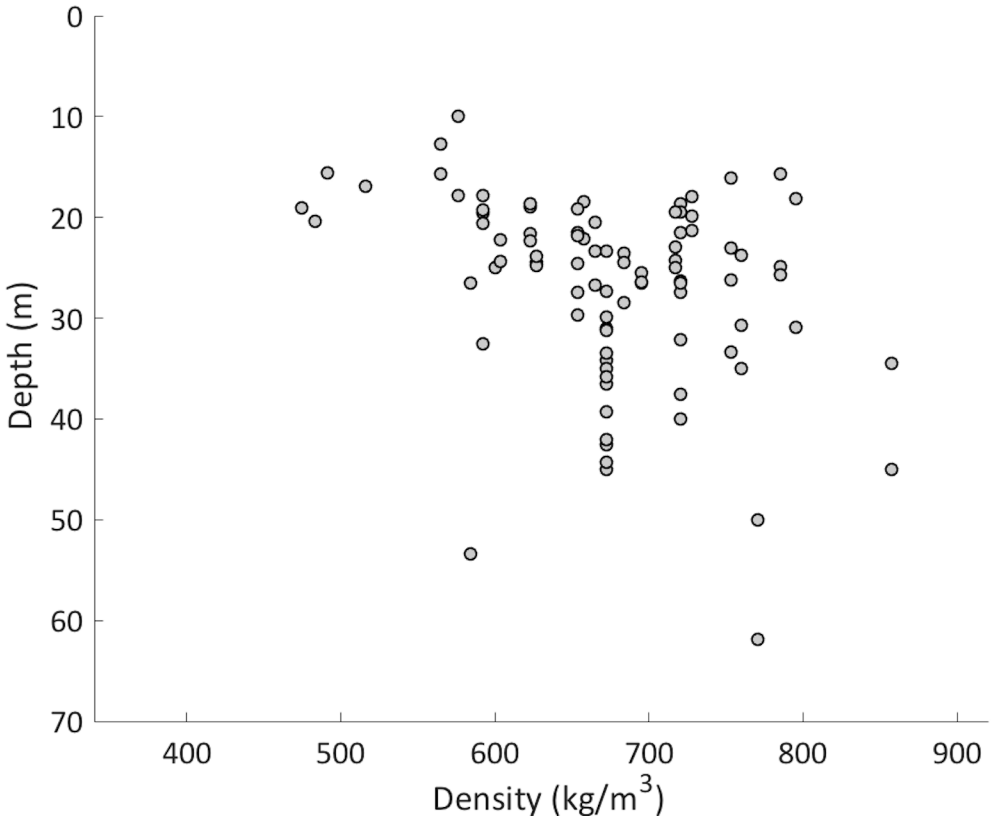

Figure 3.7. Density of firn vs depth within the MSZ. Estimated density with depth derived from dieletric constant from GPR analysis of hyperbolic diffractions from transects 154_A, 360_A, and 149_A (labeled in Fig. 3.3 using Eqn. 3.1)

3.6 Results

3.6.1 Ice Density, Marine Ice Layer, and Total Thickness

Matching hyperbolic diffractions to particular dielectric permitivity values at depth, I found most features to have a density of 721 kg m^{-3} (from Eqn. 3.1 with ϵ=2.6 with a minimum firn stratification depth of ∼28 m) and found almost all hyperbolic features exist above 40 m, which I interpreted to be the bottom of the firn layer. A density of 721 kg m^{-3} for the top 28 m of firn and density of 819 kg m^{-3} for the remaining 12 meters (average between 721 and 917 kg m^{-3}) were then assumed. These values were incorporated into equation 3.3 to solve for the thickness of the marine ice layer resulting in a marine ice thickness range between 8 and 55 m. However, I found several diffractions distributed

throughout the marine ice layer from the 100 MHz frequency portion of the GPR datasetat at depths of ∼28-30 m. Approximately 18 percent of the original thickness estimate was thinner than this 28 m estimate, most of which was in the southernmost portion of the survey. However, I was able to find at least one example of a diffraction between 28-30 m in this region. I therefore set the minimum marine ice thickness to 28 m in all regions where the solution was thinner than these observations, and found the total thickness within the study region to range between 180 and 210 m.

3.6.2 Instantaneous Velocity Results

Comparing instantaneous velocity results between ISSM_{BM}, ISSM_{BM2}, and ISSM_{IS}, I found ISSM_{BM2} to exhibit a greater change in velocity magnitude in response to the same perturbation regardless of the magnitude or location (i.e., case study) of thinning applied (See Fig. 3.8 for results from 1m thinning applied to Case study 3). This makes sense because ISSM_{BM2} had a thinner initial thickness, therefore a relatively greater portion of the ice shelf was removed under the same thinning scenario. However, all three model suites exhibited a velocity response at a similar maximum distance away from the thinning perturbation. This agrees with findings from (Reese and others, 2018) and their prediction that localized ice-shelf thinning can accelerate ice flow up to 900 km away from the initial perturbation. In addition, each model scenario exhibited a linear response in velocity with the increased amount of thinning (i.e. the 2m forcing resulted in roughly double the change in velocity than the 1m forcing).

3.6.3 Transient Velocity Results

A comparison of the change in ice flux across the grounding line between ISSM_{BM}, ISSM_{BM2}, and ISSM_{IS} revealed similar findings to the instantaneous velocity results; ISSM_{BM2} was found to be more sensitive to scenarios of applied thinning and basal melt rates than ISSM_{BM} and ISSM_{IS}. However, I did find discrepancies in ice flux between the various model suites to be larger in the northern portion of the domain (Fig. 3.9 Case

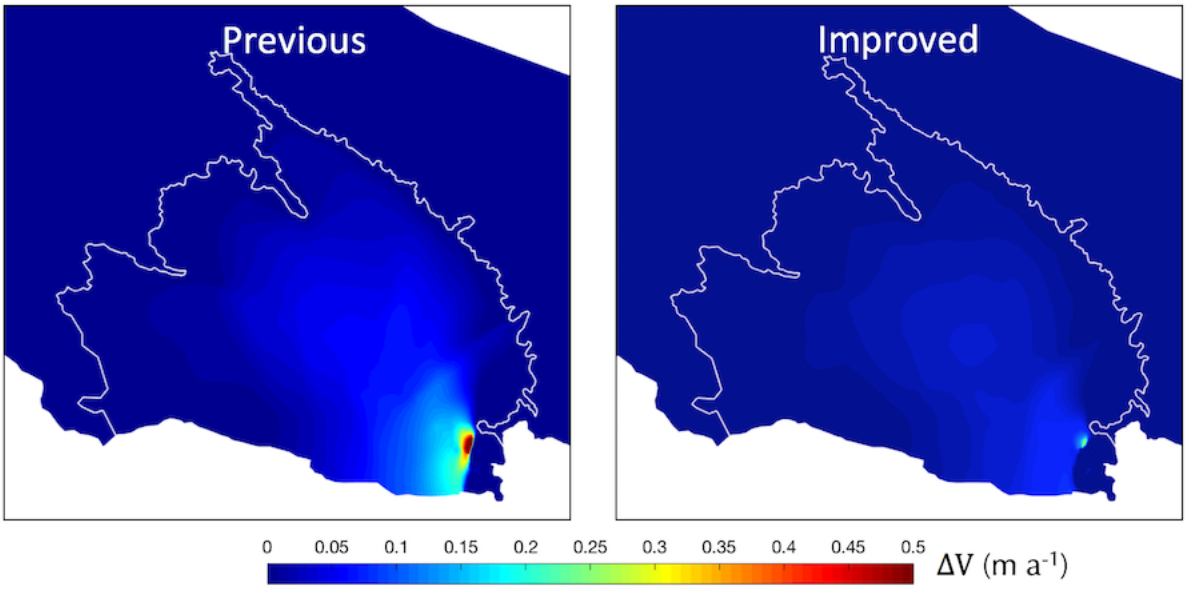

Figure 3.8. Instantaneous velocity response to thinning within MSZ 1m thinning perturbation applied to Case Study 3 for Bedmap2 (left) and BedMachine+ GPR estimate model (right)

Table 3.4. Change in accumulated flux response for all case studies for various melting scenarios over 25 year simulations in gigatons (Gt)

Model Name	1 m Forcing	2 m Forcing	3 m Forcing
ISSM$_{BM}$	0.267	0.557	0.870
ISSM$_{BM2}$	0.438	0.970	1.612
ISSM$_{IS}$	0.262	0.546	0.851

studies 3, 4, and 5). To explain this spatial sensitivity, I compared the change in total flux of each model to the total percentage of ice removed and found a roughly linear relationship. This pattern suggests that Case studies 3, 4, and 5, have greater discrepancies in ice flux simply because a greater portion of the ice shelf is removed. However, this relationship is not perfectly linear. For example the ISSM$_{BM2}$ scenario for Case study 3 had 57.1 percent of its initial thickness removed and exhibited a change in flux of 27.4 Gt while Case study 4 had 57.9 percent of its initial thickness removed and exhibited an increase in flux of 25.1 Gt. Even though Case study 4 had a greater portion of its ice removed, it underwent a smaller change in flux. One possible reason for this non-linearity

could be differences in the initial ice hardness parameter between different model suites. Each model's final rheology inversion step is sensitive to its initial ice thickness dataset. For the Bedmap2 scenario, the inversion step compensates for the underestimation of ice thickness through a larger value of the ice hardness parameter(i.e. stiffer ice).

After exploring the spatial sensitivity of individual case studies, I analyzed the combined effect of thinning across all case studies (Table 3.4). The magnitude of flux between the various scenarios was relatively small (for example the maximum deviation was $\sim$ 7.61 Gt between ISSM_{BM2} and ISSM_{BM2} for the 3 m scenario). However, under the same amount of applied thinning, the flux response of the Bedmap2 initialized scenario was roughly twice that of the scenario initialized by a combination of BedMachine and *in-situ* data.

3.7 Discussion

3.7.1 Implications on Other Shear Margins and Ocean Circulation Models

The reasons why ice thickness is poorly constrained in the McMurdo Shear Zone within the Bedmap2 dataset, such as firn densification and presence of marine ice, are applicable to other shear margins within and around Antarctica. This discrepancy is concerning when taking into account the collocation of these inherently weak regions with basal troughs that preferentially channelize warm ocean water. The mechanism of basal channel deepening and shear-margin weakening has only recently been put forth and requires further exploration in paleo and modern numerical models. The results from this chapter suggest that particular care should be taken when initializing shear margin ice thickness in these simulations, and that estimates of sea level rise would benefit from *in-situ* thickness measurements in these previously poorly constrained regions.

This work not only has implications for ice flow numerical models, but sub-ice shelf ocean circulation models as well. In particular, the thickness estimates presented herein suggest a need for revising ice draft within the McMurdo Shear Zone as well as other shear margins more broadly. Modeled basal melt rates, such as those from Tinto and others

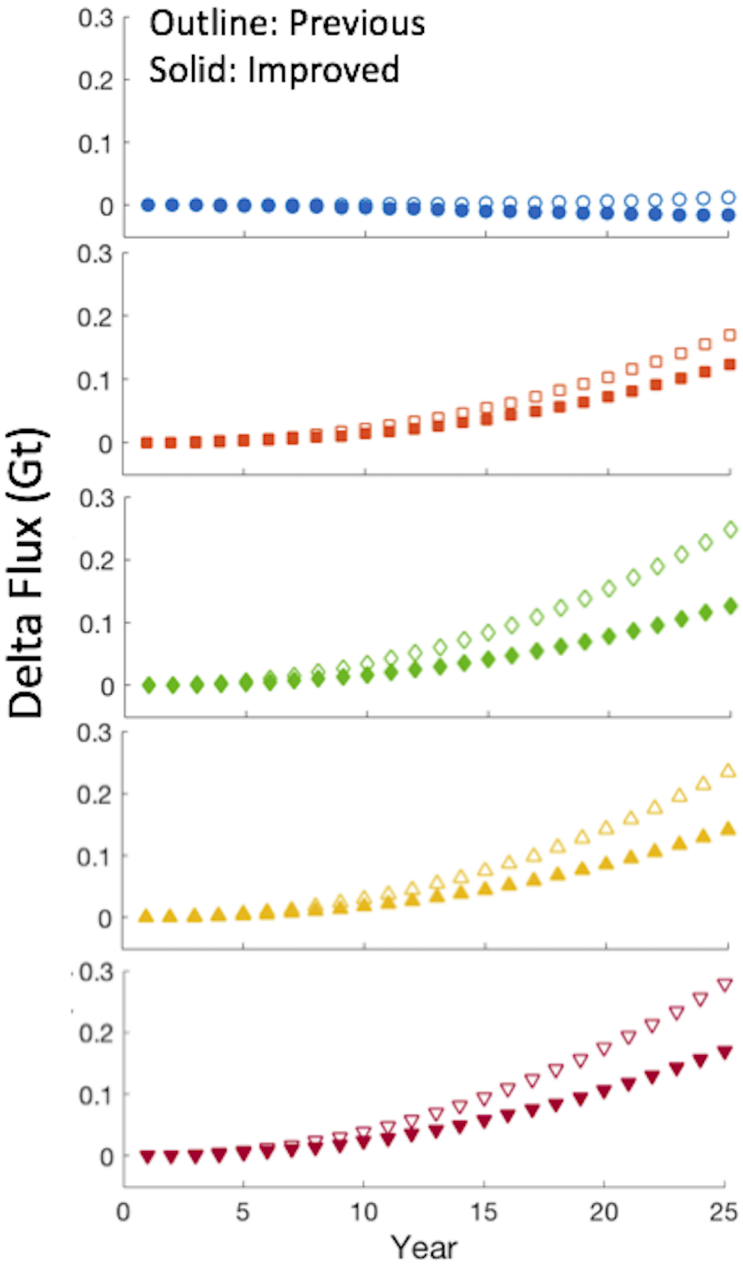

Figure 3.9. Comparison of ice flux across grounding line for various case studies Response to 1m thinning of a 25 year model run for ISSM_{BM2} and ISSM_{IS}

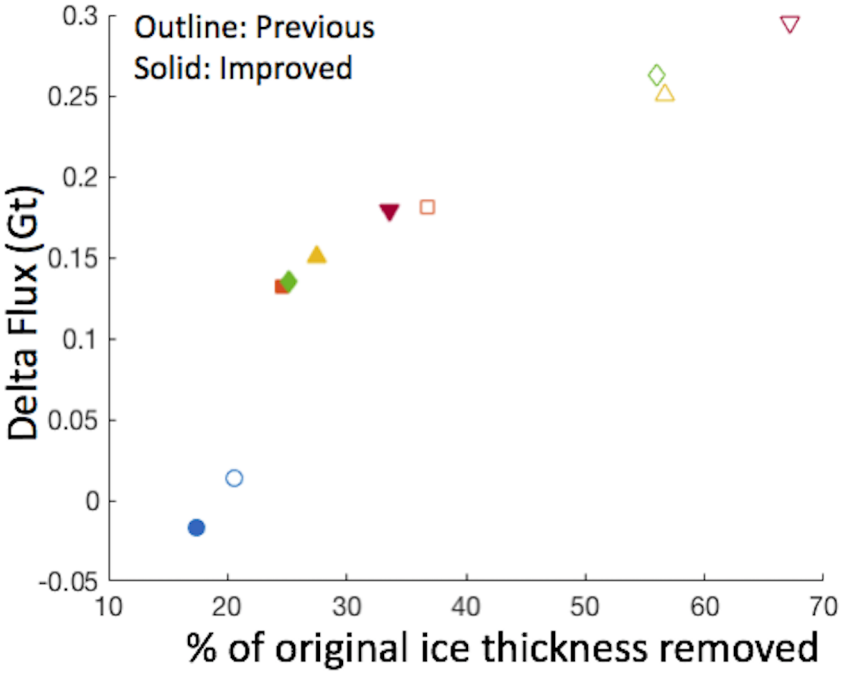

Figure 3.10. Percentage of ice thickness removed for each case study vs change in flux Case studies are from models ISSM_{BM2} and ISSM_{IS}

(2019), have overestimated basal melt rates within the MSZ compared to altimetry-based estimates (Adusumilli and others, 2020) as well as estimates derived from phase-sensitive radio echo sounding measurements (Stewart and others, 2019). The overestimation of basal melt rates within ocean circulation models is likely due to the discrepancy in ice draft between Bedmap2 data and the actual ice thickness; a scenario initialized with a thinner ice geometry would simulate warmer water circulation into the ice shelf cavity.

3.8 Conclusions

My analysis found the total thickness within the study region to range between 180 and 210 m, 28-55 m of which is basal marine ice. These thickness estimations are more than three times as thick as data from Bedmap2 in certain areas. The GPR observations also indicate that firn within the McMurdo Shear Zone is particularly dense, with a density of 721 kg m^{-3} for the top 28 m of firn and density of 819 kg m^{-3} for the remaining 12 meters.

Shear-induced firn densification processes likely contributed to these high values. It is likely that Bedmap2's underestimation of ice thickness in this region is due to an underestimation of total ice shelf column density due to both these firn processes as well as the incorporation of a denser basal marine ice layer. Through my numerical modeling simulations, I found the flux response of the scenarios initialized by Bedmap2 to be roughly twice as sensitive to the same amount of applied thinning to scenarios initialized by a combination of BedMachine and *in-situ* data. These findings suggest *in-situ* thickness estimates are sorely needed in previously poorly constrained ice shelf lateral margins more broadly over the ice sheet in order to improve estimates of sea level rise.

CHAPTER 4
CONSTRAINING KINEMATICS OF THE WHILLANS/MERCER ICE STREAM CONFLUENCE

4.1 Introduction

The West Antarctic Ice Sheet has experienced significant mass loss along its coastline region in recent decades and is believed to be preconditioned for collapse by the end of the century. The region's prerequisites for rapid change include both anthropogenic drivers such as oceanic warming as well inherent instabilities, such as the Marine Ice Sheet Instability. This runaway process – a grounding line retreat into deeper water that exposes a greater ice surface area to basal melt – could contribute approximately 3.3 m of sea level rise by the end of the century (Bamber and others, 2009). The Siple Coast is another region in West Antarctica undergoing dynamic changes and has had a complex history over the past ∼1000 years. Six of its major ice streams (Mercer, Whillans, Kamb, Siple, Bindschadler and MacAyeal) having experienced significant changes to flow patterns, mass balance, as well as shifts in shear margin and grounding line positions (Catania and others, 2012)). One major dynamic player in the region is the Whillans Ice Stream (WIS), which has stagnated and activated within the last 1000 years (Hulbe and Fahnestock, 2007). A long-term slowdown (∼4 m a^{-1}) and a thickening (0.06 +/- 0.02 m a^{-1}) of WIS are believed to be occurring (Joughin and others, 2005; Stearns and others, 2005) which could result in a shutdown by ∼2150.

While the exact mechanism of the switch from stagnation to activation in ice streams is unknown, the phenomenon arises from the fact that the ice-bed interface is thermo-mechanically unstable. As thinning occurs, a reduction in overburden pressure leads to a greater basal temperature gradient, and heat created from shear heating is advected away from the bed more efficiently. This will eventually lead to a switch from basal melting to basal freeze-on at the ice-till interface. This freeze-on causes a heat sink,

and water flows out of the till leading to dewatering or a more consolidated (i.e. stronger) till layer. This enhances ice flow slowdown, further reducing the contribution of shear-heating leading to further till consolidation and ice deceleration.

While weak englacial sediments and thermo-mechanical feedbacks at the ice-bed interface represent the internal drivers that can lead to velocity changes on centennial timescales and the imminent stagnation of WIS, it is important to note that all of the ice streams within the Siple Coast region are intricately connected. In some cases the ice streams are hydrologically linked through subglacial meltwater pathways (Christofferson et al., 2014), and in all cases each ice stream is thermo-mechanically linked at the confluence of its neighboring ice streams (Schoof and Mantelli, 2021). As an example, the last time WIS shut down it caused major impacts to the Mercer and Kamb Ice Streams (Catania and others, 2012), leading to grounding line retreat in the neighboring ice streams.

In this study, I combine crevasse observations from high-frequency ground penetrating radar (GPR) surveys and kinematic outputs derived from a collection of remotely-sensed ice surface velocities over the past two decades in order to characterize the slowdown of the Whillans Ice Stream through time and investigate the kinematic drivers of crevasse initiation within and around the shear margin of the Whillans and Mercer Ice Streams. In addition, I utilize the Ice Sheet System (ISSM; Larour and others 2012) to project previous slowdown trends forward in time in order to predict the future evolution of deceleration, thickening, shear margin advection, as well as impacts on crevasse initiation.

4.1.1 The Whillans/Mercer Ice Stream Confluence

Velocity observations along the Whillans Ice Plain and Mercer Ice Stream are temporally limited; *in-situ* datasets are scarce due to the difficulty of carrying out field campaigns in the remote region and satellite observations are exceptionally limited due to the regions extreme southern latitude. The earliest observations of the Whillans Ice Stream indicate it has been slowing down since at least 1963 (Stephenson and Bindschadler, 1988),

with a multi-decadal average deceleration rate between 3.0 to 5.6 +/- 2 m yr^{-2} (Beem and others, 2014) and a thickening rate of 0.06 +/- 0.02 m a^{-1} (Joughin and others, 2005). However, continuous GPS stations deployed near the Whillans and Mercer Ice Streams between 2007 and 2012 recorded a deceleration rate of 6.1 to 10.9 +/- 2 m yr^{-2}, nearly double that of the multi-decadal average.

While the general cause of long term changes in velocity along the Whillans Ice Stream is attributed to a strengthening of the ice stream bed due to basal freeze-on and dewatering of till, the exact subglacial mechanism that modulates basal resistance to ice motion on the short term timescale is debated. One possible mechanism of deceleration is a change in subglacial hydrology. Observations of lake drainage events from altimetry and GPS measurements reveal an active and interconnected system of lakes (Fricker and Scambos, 2009; Siegfried and others, 2014, 2016), with the timing of surface lowering (attributed to drainage events) often correlating with local accelerations to ice flow. In particular, high-frequency observations between 2012-2014 revealed a cascading drainage event, with velocity anomalies on the order of 1 to 4 percent (Siegfried and others, 2016), a large enough magnitude to reverse the regional slowdown over the two year time period.

In addition to hydrological mechanisms, a strengthening of the subglacial till has been proposed as a possible mechanism for short term changes. Previous studies predict a freeze-on rate of 2–5 mm yr^{-1} beneath the WIS (Joughin and others, 2004), a number consistent with force budget modeling estimates of a reduction of the basal till void ratio and increase in basal resistance on these time scales (Beem and others, 2014).

4.2 Methods

4.2.1 GPR Processing and Analysis

I post-processed ~150 km of 350 and 400 MHz GPR data within the WMIS region. While an analysis of the 400MHz was prioritized, there were some data recording issues with the GSSI SIR4000 control unit when synced to the 400MHz antenna. In these

locations, I supplemented with the lower-resolution 350 MHz dataset when necessary (see Fig. 4.1). Two places where the GPS stopped recording were excluded from the analysis.

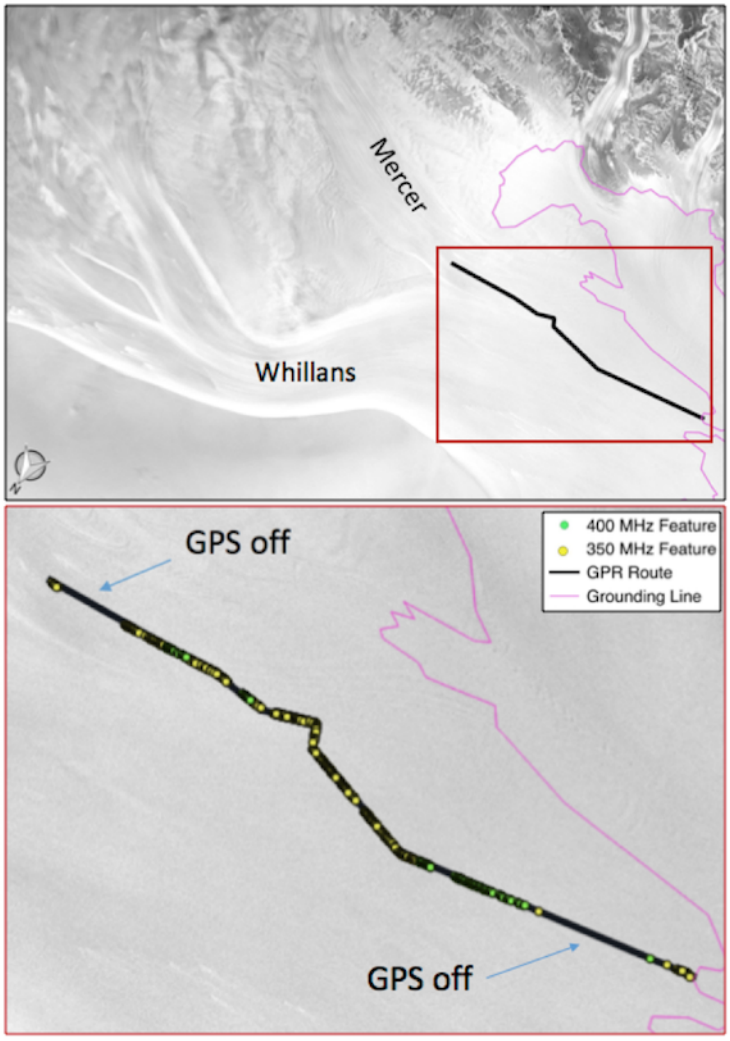

Figure 4.1. WMIS overview. Top) Overview of WMIS region with relevant portion of the Subglacial Antarctic Lakes Scientific Access (SALSA) traverse route overlaid on a RADARSAT 2 image with the grounding line shown in pink. Bottom) Zoom in of the red box in the overview figure. Green dots indicate features identified from the 400 MHz dataset and yellow dots indicate features identified from the 350 MHz dataset where higher-resolution data was unavailable due to recording issues. Sections where the GPS stopped recording (i.e. no data was available) are indicated with arrows.

For post-processing, I manually identified the leading edge of the direct-coupling wave in the radar profiles and set the depth to zero at that point. I then used the travel time to depth conversion to transform the round-trip transit time into thickness. A broadband

finite-impulse response filter was applied to the time-corrected transects to alleviate high-frequency noise and low-frequency modulation. Within the post-processed dataset, I searched for hyperbolic diffractions indicative of crevasses, and in particular searched for crevasses with distinct voids in which diffractions emanate from the terminated strata along their walls following the methodology outlined in Kaluzienski and others (2019).

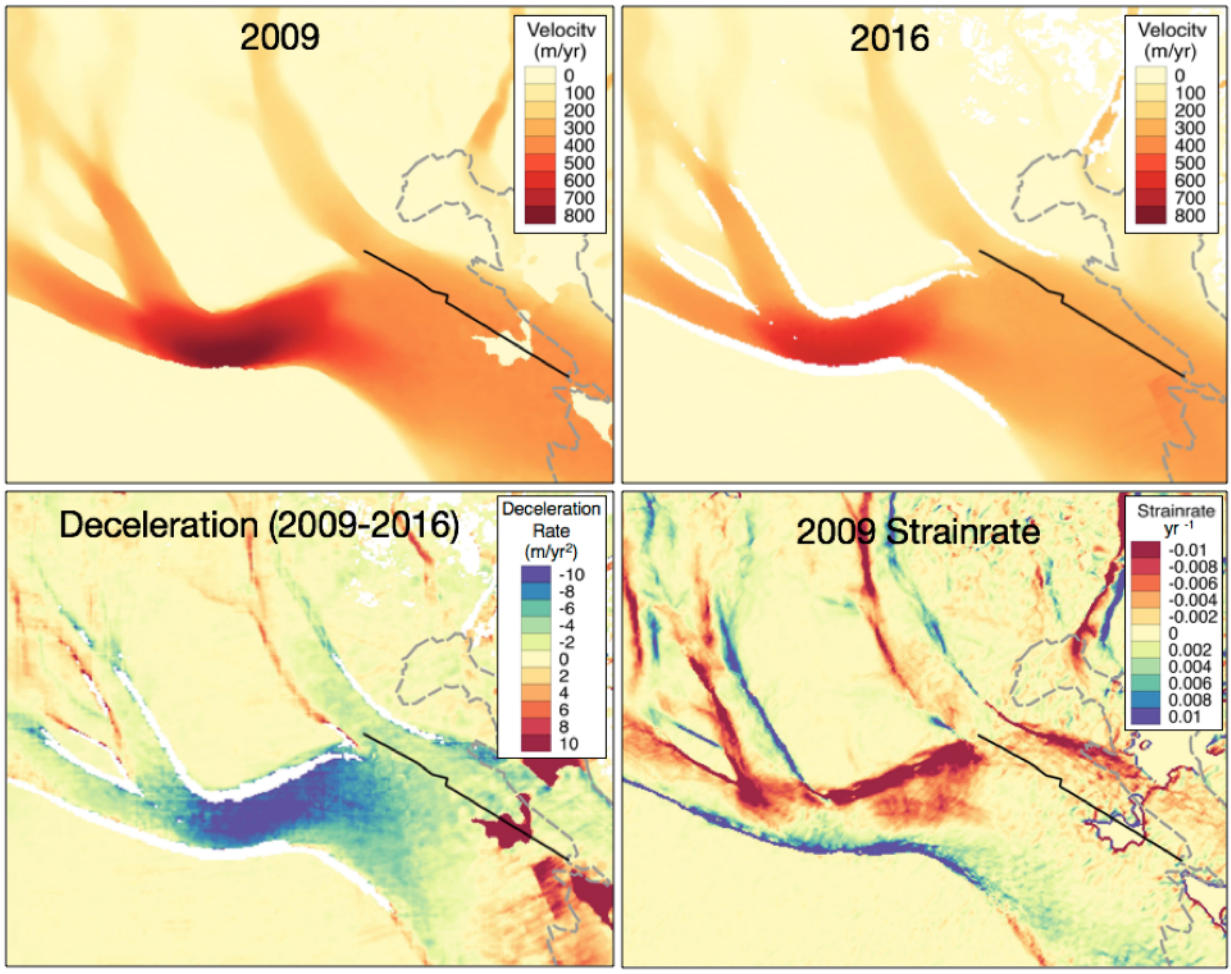

Figure 4.2. Kinematic plots of WMIS. Top Left) 2009 velocity map from RADARSAT2. Top Right) 2016 velocity map from MEaSUREs2. Bottom Left) Deceleration map from 2009-2016 time period showing yearly rate of deceleration. Bottom Right) Shear strain rate map derived from 2009 MEaSUREs 2 dataset.

4.2.2 Remote Sensing Data Collection and Kinematic Analysis

For the region of interest, only RADARSAT-1 and 2 data were available as no other sensor covered regions this far south. RADARSAT-1 collected data in 1997 and RADARSAT-2 collected data over several years between 2009-2018. However, only yearly velocity data from 1997, 2009, 2013, and 2016 had reasonable coverage over the study region. Yearly velocity estimates were derived within each dataset using speckle tracking techniques. The acquisition time period for 2013 and 2016 was centered on January 1st, while 1997 and 2009 were collected over three-month periods. The 1997 and 2009 velocity estimates had a tidal correction applied, whereas the latter two did not. However, because RADARSAT-2 had a repeat cycle of 24 days and multiple scenes were taken each year and averaged, I do not expect a significant tidal influence on the latter non-tidal corrected velocity datasets.

For each year, I created gridded estimates of spatial derivatives in ice velocity using a Kriging algorithm and calculated spatial gradients of the velocity field using neighboring pixels. Shear strain rate, vorticity rate, and dilatation rate were then calculated following previous work in Kaluzienski and others (2019). Applying the methodology therein, critical kinematic threshold values for crevasse initiation were determined based on the location of crevasses from the GPR record and the derived kinematic outputs.

A detailed streamline analysis was subsequently carried out along five separate streamlines (Fig. 4.1). I solved for the yearly along-flow deceleration rate over three different time periods: 1997-2009, 2009-2013, and 2013-2016 (these years had the most expansive velocity coverage). I also compared the yearly deceleration rate with spatial patterns of mass change estimated from ICESat and ICESat-2 missions (Smith and others, 2020) by extracting the average mass change per year along each streamline. I then analyzed the timing and location of subglacial lake drainage events and velocity fluctuations recorded by Siegfried and others (2014) between 2004 and 2014 in comparison with the deceleration rate(see Fig. 4.8a.).

4.2.3 Ice Sheet Numerical Modeling

The velocity time series and extrapolated mass change estimates from ICESat and ICEsat-2 missions (Smith and others, 2020) were incorporated into a large-scale ice flow model of the Whillans and Mercer Ice Streams developed within the Integrated Ice Sheet System Model (ISSM; Larour and others 2012), a finite element thermomechanical model of ice flow. Through inversion techniques, I solved for annual changes of the basal friction coefficient in order to force a continued slowdown of the Whillans Ice Stream through an increase in basal shear stress. Transient simulations were carried out over a 100 year time period to study the future evolution of the Whillans Ice Stream and resultant changes in principal strain rates that could impact crevasse initiation.

4.2.3.1 Geometry and Paramaterization

The model domain was first set to the local catchment. To reduce computation time, I clipped the upstream region where ice flow was less than $\sim$10 m yr^{-1}. I used an adaptive mesh with resolution varying between 7 km and 450 m. The mesh was refined based on an effective strain rate map derived from MEaSUREs phase-derived velocity data (Version 1; Mouginot and others 2019) resulting in refined shear margins and a final mesh of $\sim$13,000 mesh elements. Bed topography was initialized from BedMachine (version BedMachine Antarctica_2019-11-05v01.nc; Morlighem and others 2020). Initial ice thickness and surface elevation were informed from estimates of ice mass changes from Smith and others (2020) and a reference Digital Elevation Model from 2016 (details discussed in the following section) and horizontal velocities were initialized using a nearest neighbor interpolation of the 2016 dataset from Radarsat-2.

To solve for elevation and thickness data for 2009 and 2016 using mass changes from Smith and others (2020), I first needed a reference DEM from a known point in time which was derived from a combination of data from the Reference Elevation Model of Antarctica (REMA; Howat and others 2019) and ICESat-2. I first calculated the difference between

REMA and an average of the first two years of ICESat-2 (2018 and 2019). REMA had a wide time distribution that varies within the study region. I therefore calculated the difference between REMA and the ICESat-2 laser epoch. Running a nearest neighbor interpolation to fill data gaps in the resultant difference map and adding this result to REMA created a near-continuous elevation map that is the surface best fit to the average of the first two years of ICESat-2 (2018 and 2019). Estimates of ice thickness and surface elevation for 2009 and 2016 were then derived by subtracting or adding the estimated yearly mass change rate from Smith and others (2020) assuming a standard ice density of 917 kg/m^3.

4.2.3.2 Inverse Methods and Ice Shelf Solution

One strength of ISSM is its capability of performing inversions for variables that are not easily derived from satellite data such as the friction coefficient. I used ISSM to perform two separate inversions for the basal friction coefficient to assess changes through time based on velocity observations from remote sensing and Digital Elevation Models (DEMs). I chose to carry out inversions for years 2009 and 2016 because these years had the least amount of data gaps in spatial coverage of velocity.

Each inversion for the basal friction coefficient k was performed over the full domain using $\tau_b = -k^2 N V_b$ (where τ_b is the basal stress magnitude, N is the effective pressure, V_b is the basal velocity magnitude) and implementing an L-curve analysis to minimize the misfit between model and observations and the regularizing term (Jay-Allemand and others, 2011).An initial guess for the friction coefficient was based on the assumption that driving stress is equal to basal stress at any given point using the geometry of the grounded ice. After performing inversions for 2009 and 2016 using each time period's corresponding velocity and geometry datasets, I solved for the average change in friction per year in order to force a 100 year transient stress balance solution. I only applied an increase in friction coefficient in regions of fast flow (i.e. not at the margins or regions of stagnant ice).

Although ISSM has the capability to implement both Full Stokes and Higher Order solutions, a Shallow Shelf (also known as Shelfy-Stream) approximation (SSA; MacAyeal 1989) was implemented in order to reduce the amount of computation time required for multiple transient scenarios. Because the majority of the model domain was a region of fast flow where basal shear stress is very low and membrane stresses dominate, this vertically integrated 2D model was sufficient.

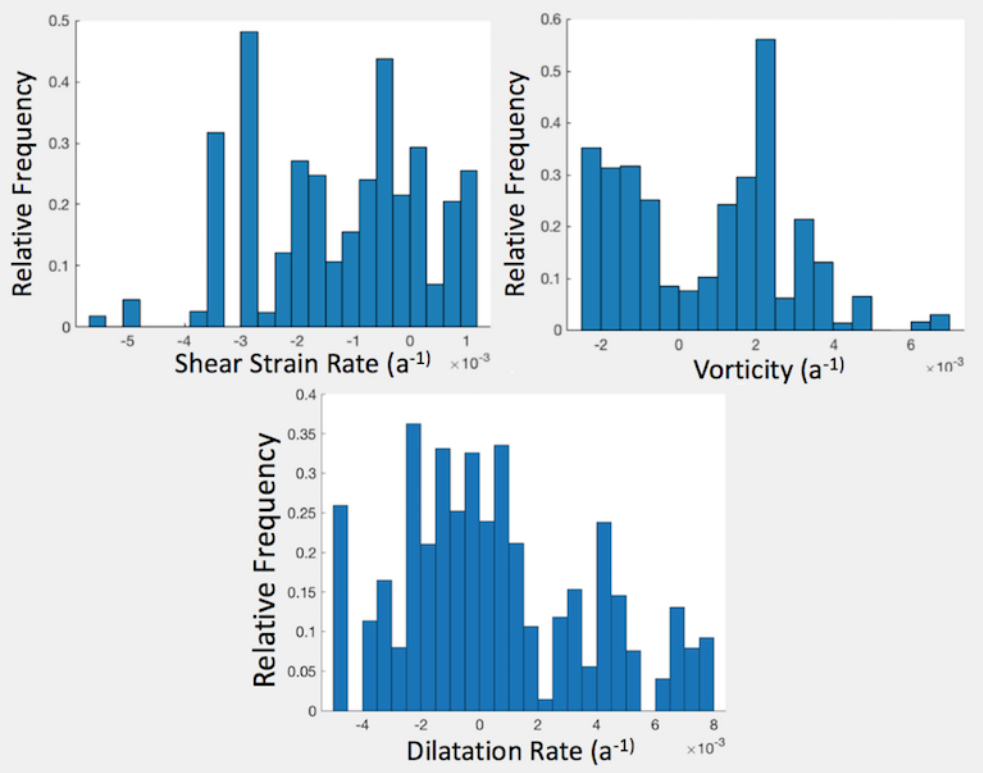

Figure 4.3. Relative frequency distribution of crevasses for WMIS region with respect to shear strain rate, vorticity and dilatation rate from the 2016 MEaSUReS2 velocity dataset.

4.3 Results

4.3.1 Kinematic and Streamline Analysis

The kinematic analysis did not reveal significant spatial changes in shear strain rate or other kinematic outputs between years. Furthermore, I did not find a strong kinematic signature that would indicate the presence of the WMIS lateral shear margin as was

expected (Fig. 4.2). This initially led me to believe the shear margin to be a relic feature with crevasses inherited from upstream. However, in light of a subsequent analysis on transient kinematic processes I later revised this hypothesis (see discussion section).

I was unable to find a correlation with the relative frequency of crevassing within any of the kinematic datasets (Fig. 4.2 ,Fig. 4.3). There are 3 potential reasons why the method did not work well for this study region:

1. The method assumes crevasses are actively forming (i.e. their occurrence is a function of the instantaneous local stress state) and does not account for the advection of features.

2. The region is not an example of simple shear (as was the case in the Kaluzienski and others 2019 study). The 2D kinematic analysis does not cover the 3D effect of basal shear stress. The region is further complicated by transient effects driven by an increase in basal resistence either due to a strengthening of the ice stream bed through basal freeze-on and dewatering of till or changes in subglacial hydrological conditions.

3. The radar dataset is less spatially detailed than in the previous study where a particular shear zone was crossed several times. In this instance the shear margin was only crossed once.

While I carried out a streamline analysis along five separate streamlines (Streamlines S1-S5, Fig. 4.5), much of streamline S4 was outside the velocity coverage from 2013. I therefore excluded this streamline from the analysis. Streamlines 1-3 (Fig. 4.4) followed the westernmost tributary of WIS and Streamline 5 (Fig. 4.5) followed the central flowline of MIS. For the WIS streamlines, the derived deceleration rate between 1997 and 2009 ranged between 3-5 m yr^{-2} and agrees well with the decadal deceleration rate found in literature ($\sim$4 m yr^{-2}, Catania and others 2012). Significantly however, I found a higher than average deceleration rate of $\sim$10-20 m yr^{-2} between 2009 and 2013 in the region of fastest

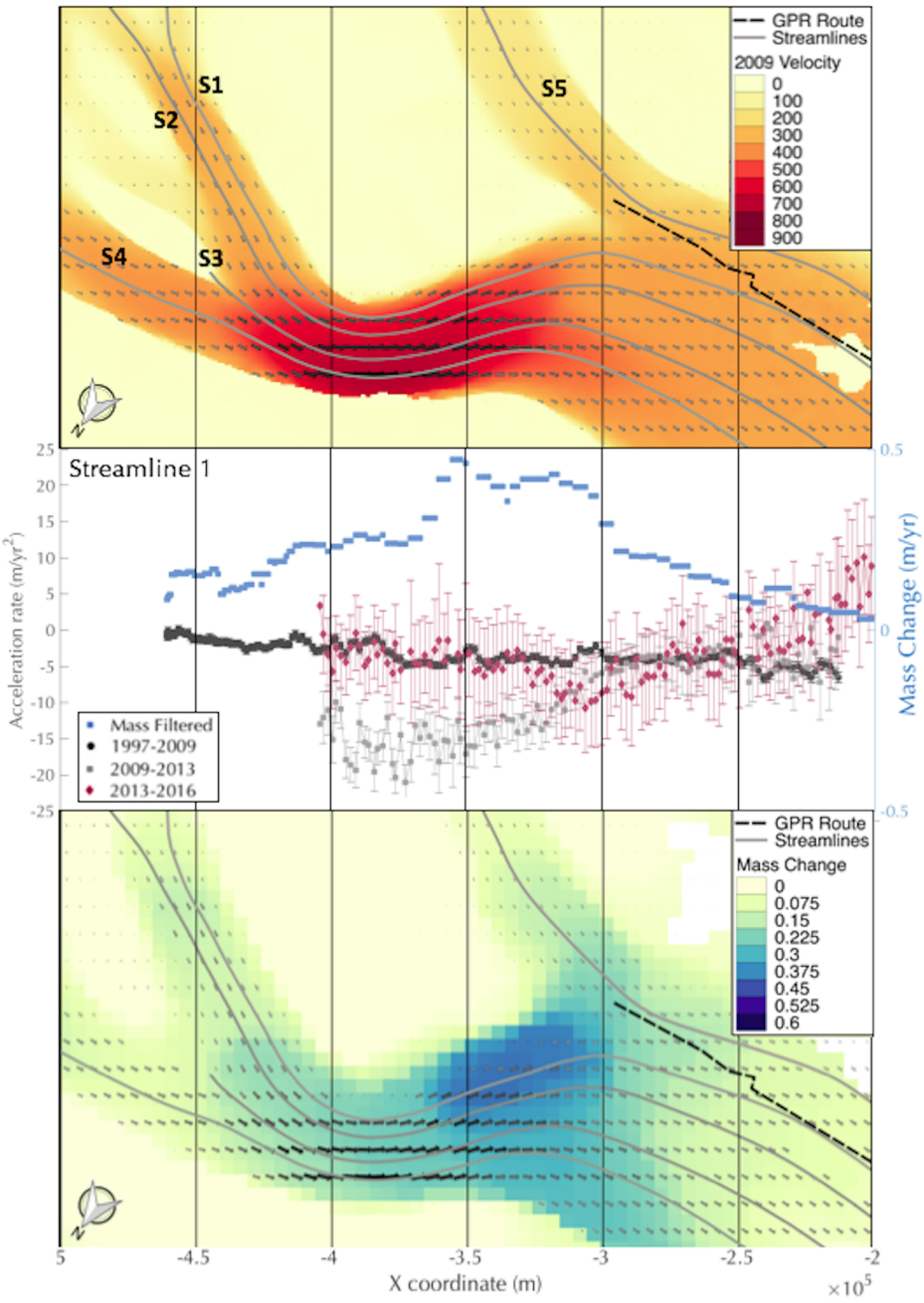

Figure 4.4. Along-flow analysis of Streamline 1. Top) 2009 MEaSUREs2 velocity map with overlaying velocity vectors. Streamlines used for flow line analysis are noted by the grey lines and the GPR route is shown by the dashed black line. Streamline 1-3 indicates the streamlines analyzed in this figure with Streamline 5 analyzed in the following Fig. 4.5. Middle) Scatter plot illustrating the acceleration rate (m yr^{-2}, left hand axis) for time periods of 1997-2009, 2009-2013, and 2013-2016 with error bars estimated from error analysis. Average mass change per year from Smith et al., (2020), shown in blue, is plotted on the right hand axis. Bottom) 2D contour plot of mass change per year (m yr^{-1}) from Smith et al., 2020 with 2009 MEaSUREs2 velocities vectors. All three panels are aligned by the polar stereographic X coordinates (in m) for spatial consistency.

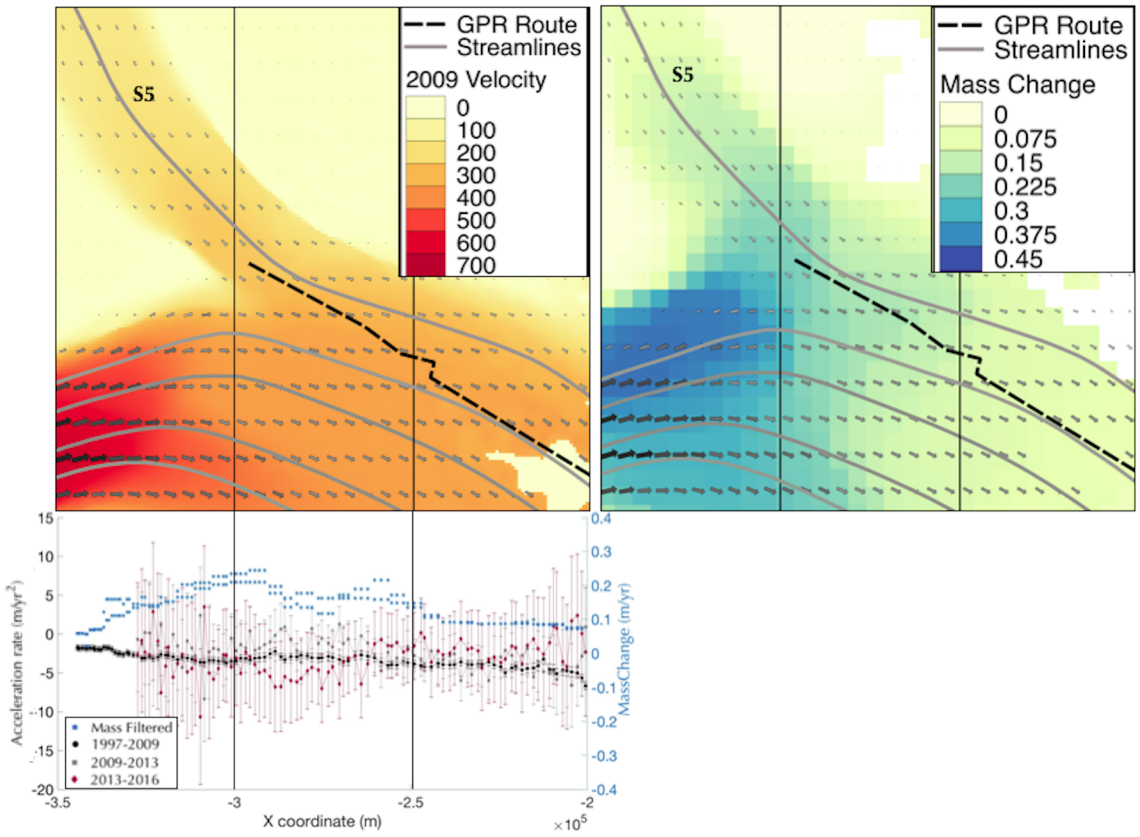

Figure 4.5. Along-flow analysis of Streamline 5 Top Left) 2009 MEaSUREs2 velocity map with overlaying velocity vectors for the zoomed in portion of the MIS. S5 indicates the streamline analyzed in this figure. Top Right) 2D contour plot of mass change per year (m yr^{-1}) from Smith et al., 2020 with 2009 MEaSUREs2 velocities vectors. Bottom) Scatter plot illustrating the deceleration rate (m yr^{-2}, left hand axis) for time periods of 1997-2009, 2009-2013, and 2013-2016 with error bars estimated from error analysis. Average mass change per year from Smith et al., (2020), shown in blue, is plotted on the right hand axis.

flow (Fig. 4.4 middle panel between -4 and -3.5 10^5 Easting). These results agree at least qualitatively with GPS measurements from Beem and others (2014) between 2012 and 2016 where they found an deceleration rate (6.1 to 10.9 +/2 m yr^{-2}) that was double the multi-decadal average. Just downstream of this area, I found the region of greatest positive mass change (Fig. 4.4 bottom panel between -3.5 and -3 x 10^5 Easting, middle blue line, bottom contour plot). Between 2013-2016, however, the peak in deceleration rate appeared to propagate downstream (Fig. 4.4, middle, red line at approximately -3 x10^5 Easting) while the region upstream returned to roughly the decadal deceleration rate. Perhaps the

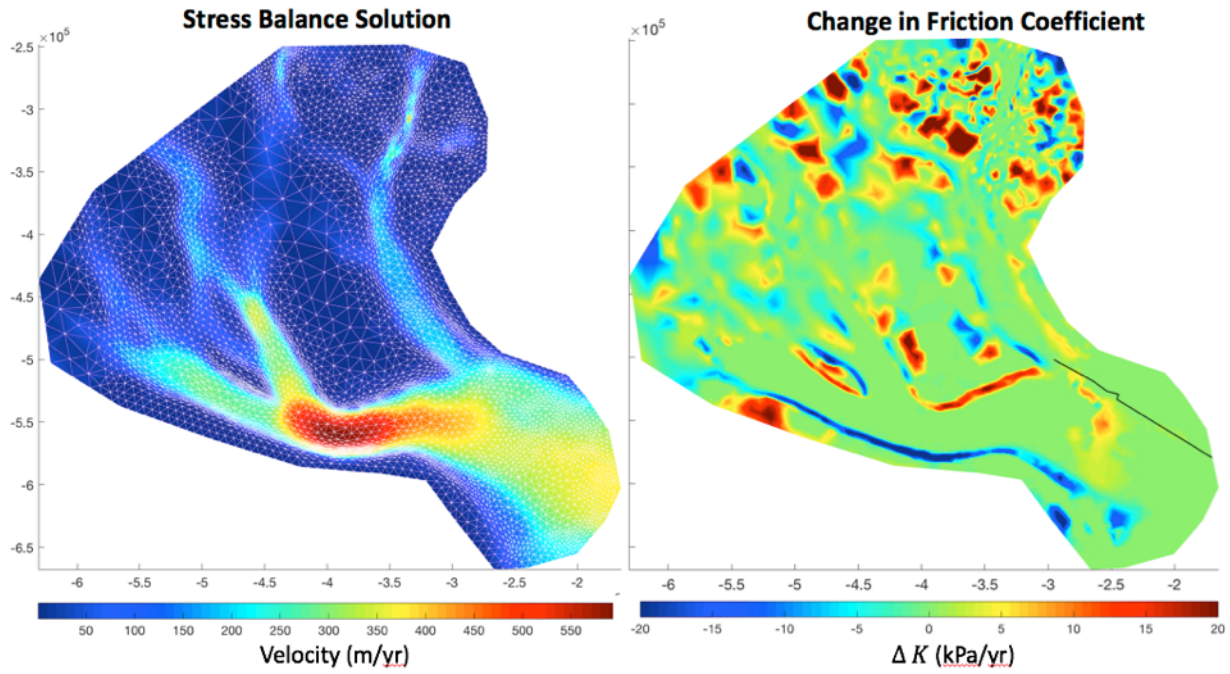

Figure 4.6. ISSM solution of ice flow and friction for WMIS region. Left) Solution of velocity from the initial ISSM stress balance solution. White outlines show grid cells for finite element analysis. Velocity initialized with 2016 MEaSUREs Velocity. Right) Yearly rate of change of friction coefficient from initial stress balance solution. GPR route indicated by black line.

most interesting finding was an acceleration further downstream of up to 10 m yr^{-2} (Fig. 4.4 red line, between -2.5 and 2 x10^5 Easting). While I found clear examples of transient velocities along WIS, I did not find significant changes in the MIS region comparable to the error estimates (Fig. 4.5), likely due to the fact that MIS velocities were much smaller compared to WIS.

4.3.2 3D Numerical Modeling

Throughout the numerical simulation, the friction coefficient increased significantly ~50 km downstream of the region of greatest mass increase (~10 kPa yr^{-1}, Fig. 4.6). This is in line with simulations from Beem and others (2014) where they found an increase in basal resistance between 10-40 kPa yr^{-1}. The model continues to increase the friction coefficient on a yearly basis and at some point in time this assumption becomes unrealistic. However,

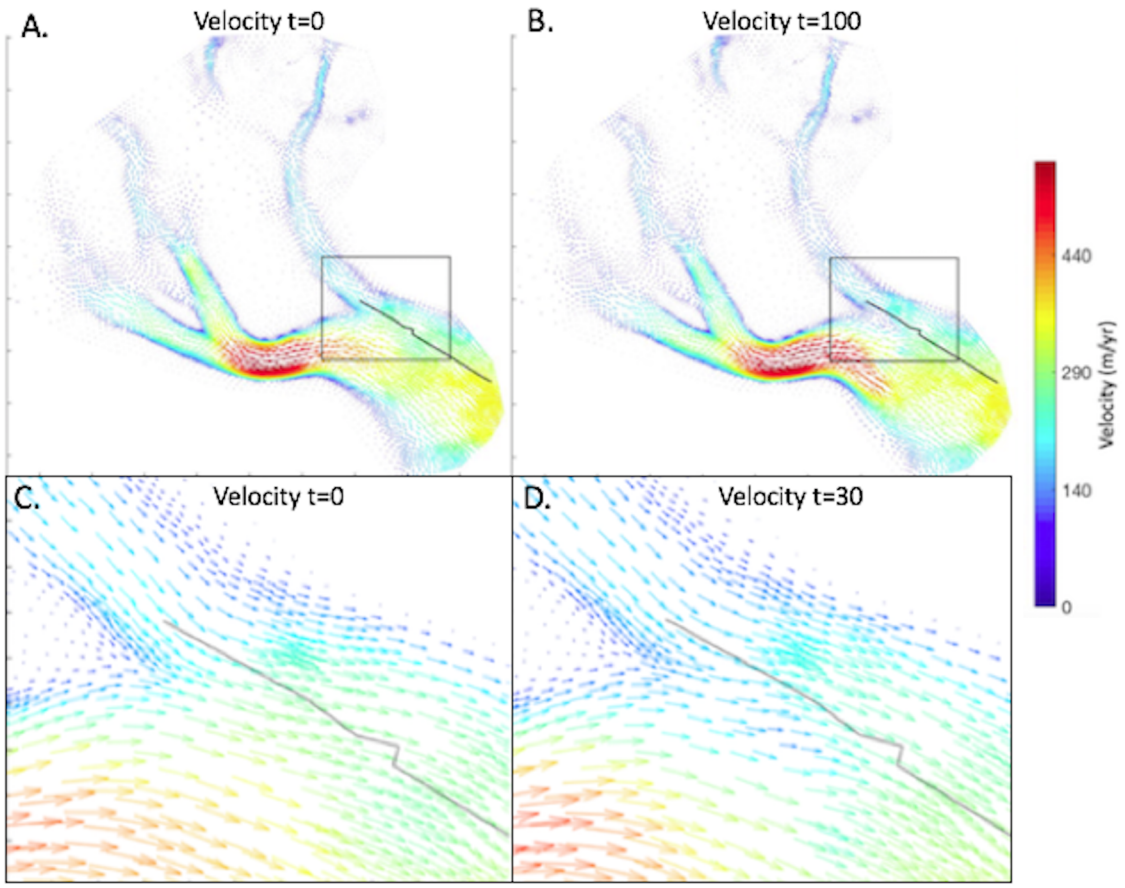

Figure 4.7. Long-term and near-term slowdown of WIS. A) Velocity vector field of initial ISSM model timestep t=0 and B) final timestep t=100. Black box in A) outlines the area of focus presented in panels C) and D) which show velocity vector fields at time t=0 and t=30 respectively.

the threshold at which this assumption breaks down is unknown. Therefore, the near-term implications of the model are more realistic. In the model, the WIS initially decelerated at a rate of $\sim$30 m yr^{-2} in the region of fastest flow just upstream of the applied region of increased basal friction. However, this deceleration rate quickly decreased in magnitude to $\sim$10 m yr^{-2} after 10 years of the simulation despite the yearly increase in friction coefficient. A long-term slowdown rate of $\sim$4 m yr^{-2} was then reached by year 25 of the simulation. The velocity slowdown lead to a thickness increase of $\sim$40 m upstream of the sticky spot in the first 25 years of the simulation, with a total thickness increase of 70 m by the end of the 100 year simulation.

As previously mentioned, the model continues to increase the friction coefficient throughout the simulation. This caused a change in ice flow direction around the area of increased basal resistance by year 10 of the simulation (See Fig. 4.7 top right for example at t=30). As flow rerouted around the sticky spot, the ice stream began to narrow and accelerate around year 40 (Fig. 4.7).

4.4 Discussion

4.4.1 Comparison of Kinematics with Subglacial Lake Drainage Events

Several subglacial lake drainage events occurred across the study region during the observation timeframe (Fig. 4.8 b). In particular, high-frequency GPS and altimetry observations between 2012-2014 revealed a cascading drainage event flowing between lakes USLC, SLC, and L7 and L8. GPS observations recorded local velocity anomalies on the order of 1 to 4 percent over this time period, which they interpreted to be large enough in magnitude to reverse the regional slowdown over the two year time period (Siegfried and others, 2016). However, results from the streamline analysis are inconsistent with this interpretation.

According to the timing of the cascading subglacial drainage event (see Fig. 4.8 b., and Siegfried and others 2016 Fig. 2d), I would have expected ice near lakes SLC, SLM, L7, and L8 to have flowed faster in 2013 before returning to normal flow speeds in 2016. This drainage event would have shown up as a deceleration event between 2013-2016 coincident or downstream of these lakes of interest, yet I either found no indication of deceleration (Fig. 4.8 red line Streamline 1/ SLC, and Streamline 5/ SLM) or an acceleration of flow (Fig. 4.8 red line Streamline 1/L78, Streamline 3/SLW, and Streamline 5/ L78). I interpreted these results to indicate that the short-term transient effects evident on the sub-decade scale were not in fact driven by lake drainage events.

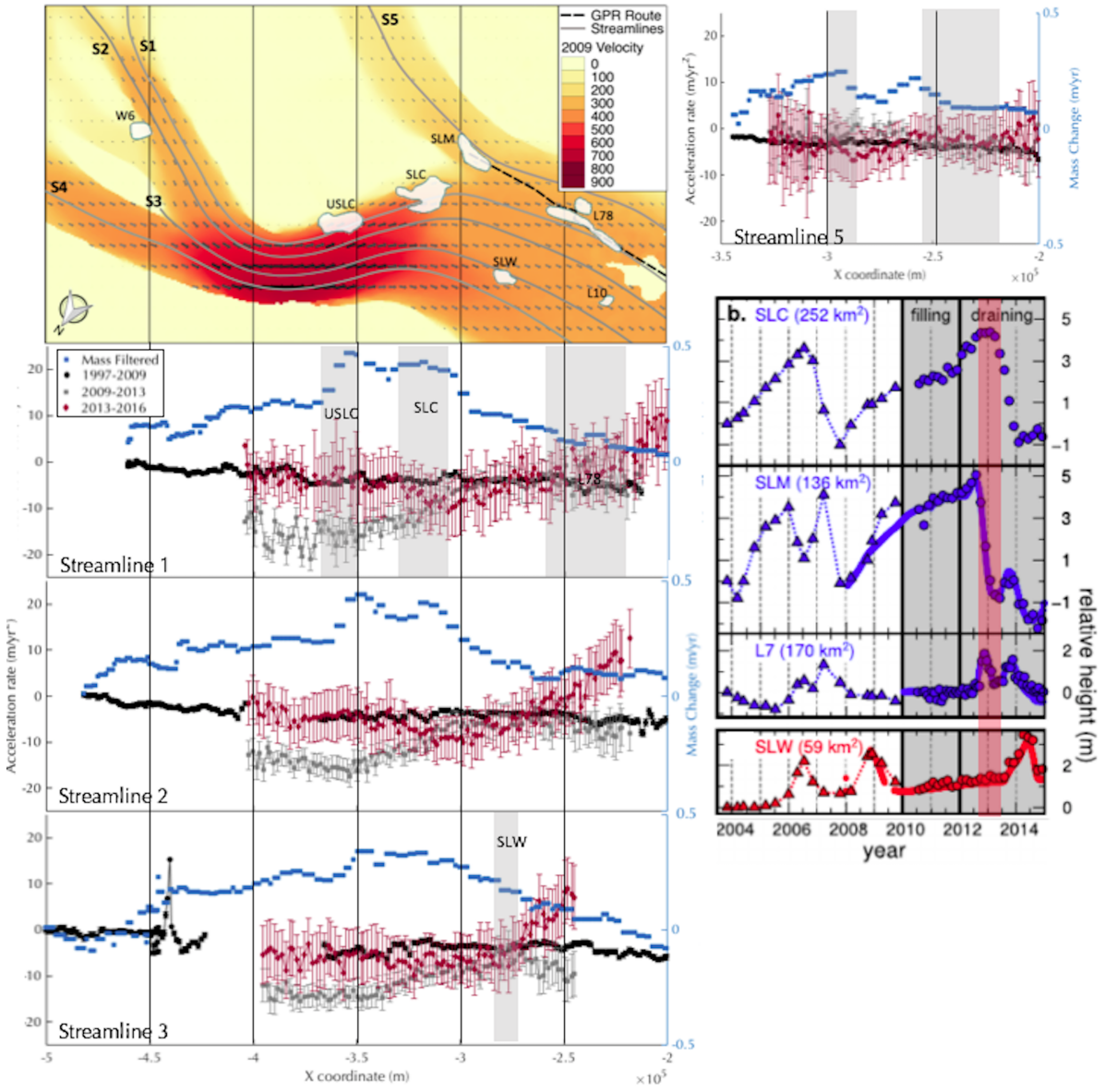

Figure 4.8. Comparison of streamline analysis to location and timing of lake drainage events a.) 2009 MEaSUREs2 velocity map with overlaying velocity vectors and locations for Streamlines 1-5, as well as locations of subglacial lakes from Siegfried et al., (2016). Below are scatter plots illustrating the acceleration rate (m yr^{-2}, left hand axis) for time periods of 1997-2009, 2009-2013, and 2013-2016 with error bars estimated from error analysis. Average mass change per year from Smith et al 2020 shown in blue, is plotted on the right hand axis. Grey shading indicates locations of subglacial lakes from Siegfried et al., 2016. b.) Time series of surface height anomalies from Siegfried et al., 2016 for lakes monitored between 2004 and 2015. Gray shading indicates period of GPS coverage with identified phases of filling and draining marked.

4.4.2 Long Term Slowdown of the Whillans Ice Stream and Implications at the Grounding Line

I was unable to find sufficient evidence that sub-decadal transient effects within WMIS region were driven by episodic lake drainage events. I therefore conclude that the underlying till mechanics exert the primary control on the variable deceleration rate of the Whillans Ice Stream. However, a hypothesis for the exact mechanism that would cause changes in the basal freeze-on rate at these timescales remains elusive in literature. The variable deceleration rate of WIS and the inadequacy of the available kinematic sampling adds complexity to the system in terms of predicting the long-term slowdown and evolution of the Whillans Ice Stream. Near-term results from the modeling scenario suggest that the slowdown could lead to a northward migration of the Whillans flow as it is diverted around the region of increased basal resistance.

Perhaps the most surprising finding from the transient streamline analysis was the discovery of a region of accelerated flow at the northwest portion of the survey. All basal processes discussed thus far have implications for a slowdown of flow in the region, not an acceleration. Similarly, the timing of lake drainage events are counter to these observations. I was therefore left to conclude that this acceleration is due to processes at the grounding line as the acceleration signal is localized to the region just above and downstream of the grounding line (Fig. 4.3 bottom left). One possible mechanism of acceleration could be localized thinning and subsequent grounding line retreat. This agrees with spatial observations of mass change from Smith and others (2020) which show a mass decrease of $\sim$0.5 m yr^{-1} over a small region just upstream of the grounding line. The slope of the grounding line in this region is very shallow, therefore it is plausible that small changes in mass could lead to a significant grounding line retreat. Another scenario could be a reduction in back-stress at the grounding line due to changes in downstream boundary conditions.

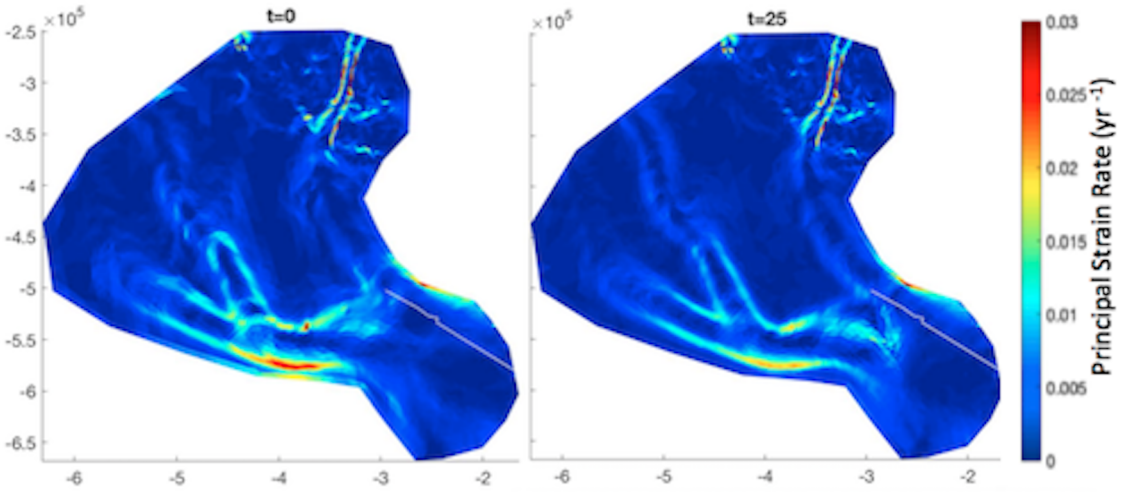

Figure 4.9. Comparison of first principal values of strain rate at t=0 and t=25. SALSA traverse route outlined in white.

4.4.3 Implications for Ground Traverses and Crevasse Initiation

The methodology that I developed as part of this work can be used to assess the likelihood of crevasse formations along other areas of complex ice flow, particularly in areas where the previous methods used in the McMurdo Shear Zone (which is undergoing simple and localized shear), are less applicable. In particular, visualizing the first principal strain rate of the modeling scenario and its change through time can help elucidate regions of likely crevasse formation (Fig. 4.9). As flow diverges around the region of increased basal resistance, the WMIS appears to split and the magnitude of the first principal strain rate increases within these two new shear margins (Fig. 4.9 right). These two regions could be particularly susceptible to increased crevassing in the near future.

4.5 Conclusions

The analysis presented here allowed for a characterization of short-term changes in the deceleration rate of WIS between 1997 and 2016. The derived deceleration rate between 1997 and 2009 ranges between 3-5 m yr^{-2} and agrees well with the decadal deceleration rate found in literature (4 m yr^{-2}, Catania and others 2012). Significantly however, I found

a higher than average deceleration rate of 10-20 m yr^{-2} between 2009 and 2013 in the region of fastest flow. A comparison of these velocity fluctuations and the location and timing of subglacial drainage events did not reveal a clear indication of a hydrologic influence. In addition, I found a region of accelerated flow at the bottom portion of the survey which I concluded was due to processes at the grounding line such as localized thinning and subsequent grounding line retreat.

Based on the model results, the friction coefficient increased significantly ∼50 km downstream of the region of greatest mass increase (∼10 kPa yr^{-1}) which agrees with simulations by Beem and others (2014). While I was unable to find a correlation with the relative frequency of crevassing within any of the kinematic datasets, I was able to predict changes in the first principal strain rate from the modeling simulations and identify regions that could have increased crevassing in the near future.

CHAPTER 5

CONCLUSIONS, BROADER IMPLICATIONS, AND FUTURE WORK

Ice shelves modulate the flow of ice from the ice sheet interior into the ocean. In turn, ice shelf lateral shear margins play an important role in providing resistance to flow and therefore represent a critical control on ice shelf stability. However, shear margins are inherently hazardous regions to both navigate and study. The presence of intense crevassing makes traversing these chaotic regions logistically difficult, sometimes hindering scientific expeditions that need to navigate around or collect data within them. In this dissertation, I have developed a statistical method to infer the presence or absence of crevasses in lateral shear zones. Through the delineation of crevasse features from ground penetrating radar observations and comparison with kinematic outputs derived from remotely-sensed ice surface velocities, I investigated the drivers of crevasse initiation within the McMurdo Shear Zone, Antarctica. My analysis suggested that flow in this shear zone is dominated by simple shear and that crevasse initiation typically occurs when the shear strain rate exceeds a value of 0.011 a^{-1} and vorticity magnitude of 0.013 a^{-1}.

A subsequent analysis of spatial patterns of crevasse attributes provided insight into crevasse history. I found crevasses to be wider with respect to their snowbridge thickness in the southern portion of our survey, which I interpreted to indicate that either a) the crevasses have a greater opening rate toward the south, or b) there is a transient effect where creases remain open for a longer period of time in the south. The latter would indicate the region is not in steady state but changing over time. However, future work to obtain observations of temporal variations in the spatial pattern of crevasse width and snowbridge thickness would be useful in order to investigate whether deviations in the flow field from steady state influence crevasse opening rates.

While the threshold values derived for the McMurdo Shear Zone cannot be directly applied to other glacial environments, thee methodology was repeated along the shear

margin between the Whillans and Mercer Ice Streams. However, this method proved inadequate for predicting crevasse initiation, likely due to the fact that the WMIS is an area of complex shear. The region is further complicated by the transient effects associated with the slowdown of the Whillans Ice Stream. A subsequent streamline analysis using available remotely-sensed velocity datasets between 1997 and 2016 revealed short-term changes in flow. The deceleration rate of the WIS was 3-5 m yr^{-2} between 1997-2009 and 10-20 m yr^{-2} between 2009-2013. Observations of these velocity fluctuations were incorporated into a transient finite element modeling solution of ice flow in order to study the future evolution of the Whillans Ice Stream. Annual changes in the basal friction coefficient were solved for using inversion techniques and a 100-year simulation was forced through an increase in basal shear stress.

Near-term results from the modeling scenario suggest that the slowdown could lead to a northward migration of the Whillans flow and a split of the current margin into two separate shear zones. A visualization of the first principal strain rate with time helped elucidate regions of potential crevasse formation within these newly formed shear margins. While this work was successful in characterizing the deceleration of the Whillans Ice Stream through time, both the streamline and numerical modeling analyses were limited by data availability due to a lack of satellite coverage in a region so far south. Future work should focus on incorporating newer velocity datasets as they become available and exploring short-term changes in velocity on a more refined timescale.

While transient changes in velocity alone can enhance crevassing, thinning within shear margins can be a compounding factor. Ice shelves in particular are vulnerable to thinning along their lateral margins through a reduction in drag and subsequent loss of buttressing. However, ice shelf shear margin geometries are poorly constrained due to inadequate density assumptions within the firn layer and presence of basal marine ice. The McMurdo Shear Zone is one such poorly constrained region; a comparison between Bedmap2 and BedMachine thickness datasets revealed the latter to be three times as thick in certain

areas. A combination of mid-frequency ground penetrating radar observations and Digital Elevation Models refined this thickness estimate further and found the total thickness within the McMurdo Shear Zone to range between 180 and 210 m. Observations from the GPR record also indicated an incredibly dense firn layer, possibly due to shear-induced firn densification processes, and 28-55 m of accreted basal marine ice.

Transient finite element numerical modeling simulations were carried out to determine how this discrepancy in ice thickness influenced mass flux across the grounding line. Three separate ice shelf geometry scenarios were tested within this numerical modeling framework, the first initialized from Bedmap2, the second initialized from BedMachine, and the last initialized using a combination of BedMachine and interpolated thickness data from the *in-situ* derived ice thickness measurements. Investigating various thinning and melt rate scenarios across each modeling suite revealed the flux response of the scenarios initialized by Bedmap2 to be roughly twice as large under the same amount of applied thinning to scenarios initialized by a combination of BedMachine and *in-situ* data.

The underlying reasons why ice thickness is poorly constrained in the McMurdo Shear Zone within the Bedmap2 dataset, such as firn densification and presence of marine ice, are applicable to other ice shelf lateral shear margins throughout Antarctica. Therefore, future work should focus on refining thickness estimates in these regions in order to improve numerical simulations and sea level rise predictions. In particular, models initialized by a combination of BedMachine and *in-situ* observations through ice core measurements within shear margins would be informative, both for total ice thickness as well as density assessment within the firn and marine ice layer.

Shear zone stability represents a potentially critical control on the mass balance of ice sheets. The work presented here developed methodologies to monitor these important regions through the utilization of *in-situ*, remote sensing, and numerical modeling techniques. In particular, I have developed a means to predict regions of intense crevassing. In regions of simple shear, I have illustrated the use of kinematic datasets such as shear

strain rate as a tool to predict crevasse initiation thresholds. In regions of complex shear or regions not in steady state, I have expanded this analysis to include a visualization of kinematic datasets and principal strain rates through time. Finally, I have illustrated that accurate ice thickness initialization within shear margins can be critically important for model projections of mass flux across the grounding line.

REFERENCES

Abramowitz, M. and I.A. Stegun, 1972. Handbook of Mathematical Functions with Formulas.

Adusumilli, Susheel, Helen Amanda Fricker, Brooke Medley, Laurie Padman and Matthew R Siegfried, 2020. Interannual variations in meltwater input to the Southern Ocean from Antarctic ice shelves, *Nature geoscience*, **13**(9), 616–620.

Alley, Karen E, Ted A Scambos, Richard B Alley and Nicholas Holschuh, 2019. Troughs developed in ice-stream shear margins precondition ice shelves for ocean-driven breakup, *Science advances*, **5**(10), eaax2215.

Alley, Karen E, Ted A Scambos, Matthew R Siegfried and Helen Amanda Fricker, 2016. Impacts of warm water on Antarctic ice shelf stability through basal channel formation, *Nature Geoscience*, **9**(4), 290–293.

Arcone, Steven A and Allan J Delaney, 2000. GPR images of hidden crevasses in Antarctica, Eighth International Conference on Ground Penetrating Radar, International Society for Optics and Photonics, vol. 4084, 760–766.

Arcone, Steven A, James H Lever, Laura E Ray, Benjamin S Walker, Gordon Hamilton and Lynn Kaluzienski, 2016. Ground-penetrating radar profiles of the McMurdo Shear Zone, Antarctica, acquired with an unmanned rover: Interpretation of crevasses, fractures, and folds within firn and marine iceGPR profiles of the McMurdo shear zone, *Geophysics*, **81**(1), WA21–WA34.

Arthern, Robert J, Dale P Winebrenner and David G Vaughan, 2006. Antarctic snow accumulation mapped using polarization of 4.3-cm wavelength microwave emission, *Journal of Geophysical Research: Atmospheres*, **111**(D6).

Bamber, Jonathan L, Riccardo EM Riva, Bert LA Vermeersen and Anne M LeBrocq, 2009. Reassessment of the potential sea-level rise from a collapse of the West Antarctic Ice Sheet, *science*, **324**(5929), 901–903.

Banwell, Alison F and Douglas R MacAyeal, 2015. Ice-shelf fracture due to viscoelastic flexure stress induced by fill/drain cycles of supraglacial lakes, *Antarctic Science*, **27**(6), 587–597.

Banwell, Alison F, Ian C Willis, Grant J Macdonald, Becky Goodsell and Douglas R MacAyeal, 2019. Direct measurements of ice-shelf flexure caused by surface meltwater ponding and drainage, *Nature communications*, **10**(1), 730.

Banwell, Alison F, Ian C Willis, Grant J Macdonald, Becky Goodsell, David P Mayer, Anthony Powell and Douglas R Macayeal, 2017. Calving and rifting on the McMurdo Ice Shelf, Antarctica, *Ann. Glaciol*, **58**, 78–87.

Beem, LH, SM Tulaczyk, MA King, M Bougamont, HA Fricker and P Christoffersen, 2014. Variable deceleration of Whillans Ice Stream, West Antarctica, *Journal of Geophysical Research: Earth Surface*, **119**(2), 212–224.

Van de Berg, WJ, MR Van den Broeke, CH Reijmer and E Van Meijgaard, 2006. Reassessment of the Antarctic surface mass balance using calibrated output of a regional atmospheric climate model, *Journal of Geophysical Research: Atmospheres*, **111**(D11).

Bindschadler, Robert, Hyeungu Choi, Amy Wichlacz, R Bingham, Jennifer Bohlander, Kelly Brunt, Hugh Corr, Reinhard Drews, Helen Fricker, Monica Hall and others, 2011. Getting around Antarctica: new high-resolution mappings of the grounded and freely-floating boundaries of the Antarctic ice sheet created for the International Polar Year, *The Cryosphere*, **5**(3), 569–588.

Blatter, Heinz, 1995. Velocity and stress fields in grounded glaciers: a simple algorithm for including deviatoric stress gradients, *Journal of Glaciology*, **41**(138), 333–344.

Blindow, N, 1994. The central part of the Filchner-Ronne Ice Shelf, Antarctica: internal structures revealed by 40MHz monopulse RES, *Annals of Glaciology*, **20**, 365–371.

Bohlander, Jennifer and T Scambos, 2007. Antarctic coastlines and grounding line derived from MODIS Mosaic of Antarctica (MOA), *National Snow and Ice Data Center, Boulder, CO, USA*.

Borstad, CP, A Khazendar, E Larour, M Morlighem, E Rignot, MP Schodlok and H Seroussi, 2012. A damage mechanics assessment of the Larsen B ice shelf prior to collapse: Toward a physically-based calving law, *Geophysical Research Letters*, **39**(18).

Borstad, Chris, Ala Khazendar, Bernd Scheuchl, Mathieu Morlighem, Eric Larour and Eric Rignot, 2016. A constitutive framework for predicting weakening and reduced buttressing of ice shelves based on observations of the progressive deterioration of the remnant Larsen B Ice Shelf, *Geophysical Research Letters*, **43**(5), 2027–2035.

Borstad, Chris, Daniel McGrath and Allen Pope, 2017. Fracture propagation and stability of ice shelves governed by ice shelf heterogeneity, *Geophysical Research Letters*, **44**(9), 4186–4194.

Bougamont, M, S Price, P Christoffersen and AJ Payne, 2011. Dynamic patterns of ice stream flow in a 3-D higher-order ice sheet model with plastic bed and simplified hydrology, *Journal of Geophysical Research: Earth Surface*, **116**(F4).

Budd, William F and TH Jacka, 1989. A review of ice rheology for ice sheet modelling, *Cold Regions Science and Technology*, **16**(2), 107–144.

Campbell, S, Z Courville, S Sinclair and J Wilner, 2017. Brine, englacial structure and basal properties near the terminus of McMurdo Ice Shelf, Antarctica, *Annals of Glaciology*, **58**(74), 1–11.

Catania, Ginny, Christina Hulbe, Howard Conway, Ted A Scambos and CF Raymond, 2012. Variability in the mass flux of the Ross ice streams, West Antarctica, over the last millennium, *Journal of Glaciology*, **58**(210), 741–752.

Catania, GA, TA Scambos, H Conway and CF Raymond, 2006. Sequential stagnation of Kamb ice stream, West Antarctica, *Geophysical Research Letters*, **33**(14).

Christianson, Knut, Leo E Peters, Richard B Alley, Sridhar Anandakrishnan, Robert W Jacobel, Kiya L Riverman, Atsuhiro Muto and Benjamin A Keisling, 2014. Dilatant till facilitates ice-stream flow in northeast Greenland, *Earth and Planetary Science Letters*, **401**, 57–69.

Christoffersen, Poul and Slawek Tulaczyk, 2003a. Response of subglacial sediments to basal freeze-on 1. Theory and comparison to observations from beneath the West Antarctic Ice Sheet, *Journal of Geophysical Research: Solid Earth*, **108**(B4).

Christoffersen, Poul and Slawek Tulaczyk, 2003b. Signature of palaeo-ice-stream stagnation: Till consolidation induced by basal freeze-on, *Boreas*, **32**(1), 114–129.

Colgan, William, Harihar Rajaram, Waleed Abdalati, Cheryl McCutchan, Ruth Mottram, Mahsa S Moussavi and Shane Grigsby, 2016. Glacier crevasses: Observations, models, and mass balance implications, *Reviews of Geophysics*, **54**(1), 119–161.

Courville, Z, 2015. Overall Shear Zone Report 2015, *Contract report to National Science Foundation Office of Polar Programs Antarctic Infrastructure and Logistics Program.*

Craven, Mike, Ian Allison, Helen Amanda Fricker and Roland Warner, 2009. Properties of a marine ice layer under the Amery Ice Shelf, East Antarctica, *Journal of Glaciology*, **55**(192), 717–728.

Craven, Mike, Frank Carsey, Alberto Behar, Jaret Matthews, Russell Brand, Alan Elcheikh, Seane Hall and Adam Treverrow, 2005. Borehole imagery of meteoric and marine ice layers in the Amery Ice Shelf, East Antarctica, *Journal of Glaciology*, **51**(172), 75–84.

Cuffey, Kurt M and William Stanley Bryce Paterson, 2010. The physics of glaciers, Academic Press.

Cyprych, D, Sascha Brune, S Piazolo and J Quinteros, 2016. Strain localization in polycrystalline material with second phase particles: Numerical modeling with application to ice mixtures, *Geochemistry, Geophysics, Geosystems*, **17**(9), 3608–3628.

Das, Indrani, Laurie Padman, Robin E Bell, Helen A Fricker, Kirsty J Tinto, Christina L Hulbe, Christine S Siddoway, Tejendra Dhakal, Nicholas P Frearson, Cyrille Mosbeux and others, 2020. Multidecadal basal melt rates and structure of the Ross Ice Shelf, Antarctica, using airborne ice penetrating radar, *Journal of Geophysical Research: Earth Surface*, **125**(3), e2019JF005241.

DeConto, Robert M and David Pollard, 2016. Contribution of Antarctica to past and future sea-level rise, *Nature*, **531**(7596), 591–597.

Dupont, TK and RB Alley, 2005. Assessment of the importance of ice-shelf buttressing to ice-sheet flow, *Geophysical Research Letters*, **32**(4).

Emetc, Veronika, Paul Tregoning, Mathieu Morlighem, Chris Borstad and Malcolm Sambridge, 2018. A statistical fracture model for Antarctic ice shelves and glaciers.

Enderlin, EM and GS Hamilton, 2014. Estimates of iceberg submarine melting from high-resolution digital elevation models: application to Sermilik Fjord, East Greenland, *Journal of Glaciology*, **60**(224), 1084–1092.

Favier, Lionel, Frank Pattyn, Sophie Berger and Reinhard Drews, 2016. Dynamic influence of pinning points on marine ice-sheet stability: a numerical study in Dronning Maud Land, East Antarctica, *The Cryosphere (Online)*, **10**(6).

Fretwell, Peter, Hamish D Pritchard, David G Vaughan, Jonathan L Bamber, Nicholas E Barrand, R Bell, C Bianchi, RG Bingham, Donald D Blankenship, G Casassa and others, 2013. Bedmap2: improved ice bed, surface and thickness datasets for Antarctica, *The Cryosphere*, **7**(1), 375–393.

Frey, Pascal, 2001. Yams a fully automatic adaptive isotropic surface remeshing procedure, (Ph.D. thesis, Inria.

Fricker, Helen Amanda and Ted Scambos, 2009. Connected subglacial lake activity on lower Mercer and Whillans ice streams, West Antarctica, 2003–2008, *Journal of Glaciology*, **55**(190), 303–315.

Gardner, Alex S, Geir Moholdt, Ted Scambos, Mark Fahnstock, Stefan Ligtenberg, Michiel van den Broeke and Johan Nilsson, 2018. Increased West Antarctic and unchanged East Antarctic ice discharge over the last 7 years, *Cryosphere*, **12**(2), 521–547.

Glasser, NF and Ted A Scambos, 2008. A structural glaciological analysis of the 2002 Larsen B ice-shelf collapse, *Journal of Glaciology*, **54**(184), 3–16.

Griggs, Jennifer A and JL Bamber, 2011. Antarctic ice-shelf thickness from satellite radar altimetry, *Journal of Glaciology*, **57**(203), 485–498.

Holland, David M and Adrian Jenkins, 1999. Modeling thermodynamic ice–ocean interactions at the base of an ice shelf, *Journal of Physical Oceanography*, **29**(8), 1787–1800.

Howat, Ian M, Claire Porter, Benjamin E Smith, Myoung-Jong Noh and Paul Morin, 2019. The reference elevation model of Antarctica, *The Cryosphere*, **13**(2), 665–674.

Hulbe, C and M Fahnestock, 2007. Century-scale discharge stagnation and reactivation of the Ross ice streams, West Antarctica, *Journal of Geophysical Research: Earth Surface*, **112**(F3).

Jansen, Daniela, Adrian Luckman, Bernd Kulessa, Paul R Holland and Edward C King, 2013. Marine ice formation in a suture zone on the Larsen C Ice Shelf and its influence on ice shelf dynamics, *Journal of Geophysical Research: Earth Surface*, **118**(3), 1628–1640.

Jay-Allemand, Maxime, Fabien Gillet-Chaulet, Olivier Gagliardini and Maëlle Nodet, 2011. Investigating changes in basal conditions of Variegated Glacier prior to and during its 1982–1983 surge, *The Cryosphere*, **5**(3), 659–672.

Jones, SJ and JW Glen, 1969. The effect of dissolved impurities on the mechanical properties of ice crystals, *Philosophical Magazine*, **19**(157), 13–24.

Joughin, Ian, RA Bindschadler, MA King, D Voigt, RB Alley, S Anandakrishnan, H Horgan, L Peters, P Winberry, SB Das and others, 2005. Continued deceleration of Whillans ice stream, West Antarctica, *Geophysical Research Letters*, **32**(22).

Joughin, Ian, Slawek Tulaczyk, Douglas R MacAyeal and Hermann Engelhardt, 2004. Melting and freezing beneath the Ross ice streams, Antarctica, *Journal of Glaciology*, **50**(168), 96–108.

Kaluzienski, Lynn, Peter Koons, Ellyn Enderlin, Gordon Hamilton, Zoe Courville and Steven Arcone, 2019. Crevasse initiation and history within the McMurdo Shear Zone, Antarctica, *Journal of Glaciology*, **65**(254), 989–999.

Kehle, Ralph O, 1964. Deformation of the Ross ice shelf, Antarctica, *Geological Society of America Bulletin*, **75**(4), 259–286.

Khazendar, Ala, Christopher P Borstad, Bernd Scheuchl, Eric Rignot and Helene Seroussi, 2015. The evolving instability of the remnant Larsen B Ice Shelf and its tributary glaciers, *Earth and Planetary Science Letters*, **419**, 199–210.

Kovacs, Austin, Anthony J Gow and J Cragin, 1982. The brine zone in the McMurdo Ice Shelf, Antarctica, *Annals of Glaciology*, **3**, 166–171.

Kovacs, Austin, Anthony J Gow and Rexford M Morey, 1995. The in-situ dielectric constant of polar firn revisited, *Cold Regions Science and Technology*, **23**(3), 245–256.

Kulessa, Bernd, Daniela Jansen, Adrian J Luckman, Edward C King and Peter R Sammonds, 2014. Marine ice regulates the future stability of a large Antarctic ice shelf, *Nature Communications*, **5**(1), 1–7.

Lambrecht, A, H Sandhäger, David G Vaughan and C Mayer, 2007. New ice thickness maps of Filchner–Ronne Ice Shelf, Antarctica, with specific focus on grounding lines and marine ice, *Antarctic Science*, **19**(4), 521–532.

Larour, E, H Seroussi, M Morlighem and E Rignot, 2012. Continental scale, high order, high spatial resolution, ice sheet modeling using the Ice Sheet System Model (ISSM), *Journal of Geophysical Research: Earth Surface*, **117**(F1).

Lenaerts, JTM and MR Van den Broeke, 2012. Modeling drifting snow in Antarctica with a regional climate model: 2. Results, *Journal of Geophysical Research: Atmospheres*, **117**(D5).

Lever, James H, 2002. Shear zone bridge safety analysis, *Contract report to US Antarctic Program (National Science Foundation) and Raytheon Polar Services.*.

Lever, James H, AJ Delaney, Laura E Ray, Eric Trautmann, LA Barna and AM Burzynski, 2013. Autonomous gpr surveys using the polar rover yeti, *Journal of Field Robotics*, **30**(2), 194–215.

Luckman, A, D Jansen, B Kulessa, EC King, P Sammonds and DI Benn, 2012. Basal crevasses in Larsen C Ice Shelf and implications for their global abundance, *The Cryosphere*, **6**(1), 113–123.

MacAyeal, Douglas R, 1989. Large-scale ice flow over a viscous basal sediment: Theory and application to ice stream B, Antarctica, *Journal of Geophysical Research: Solid Earth*, **94**(B4), 4071–4087.

MacDonald, G, A Banwell, I Willis, D Mayer, B Goodswell and D MacAyeal, 2019. Formation of pedestalled, relict lakes on the McMurdo Ice Shelf, Antarctica, in press, *Journal of Glaciology*.

MacGregor, Joseph A, Ginny A Catania, Michael S Markowski and Alan G Andrews, 2012. Widespread rifting and retreat of ice-shelf margins in the eastern Amundsen Sea Embayment between 1972 and 2011, *Journal of Glaciology*, **58**(209), 458–466.

Maule, Cathrine Fox, Michael E Purucker, Nils Olsen and Klaus Mosegaard, 2005. Heat flux anomalies in Antarctica revealed by satellite magnetic data, *Science*, **309**(5733), 464–467.

McGrath, Daniel, Konrad Steffen, Harihar Rajaram, Ted Scambos, Waleed Abdalati and Eric Rignot, 2012. Basal crevasses on the Larsen C Ice Shelf, Antarctica: Implications for meltwater ponding and hydrofracture, *Geophysical research letters*, **39**(16).

Meier, MF, 1958. Vertical profiles of velocity and the flow law of glacier ice, *International Association of Scientific Hydrology*, **47**, 169–170.

Morlighem, Mathieu, Eric Rignot, Tobias Binder, Donald Blankenship, Reinhard Drews, Graeme Eagles, Olaf Eisen, Fausto Ferraccioli, René Forsberg, Peter Fretwell and others, 2020. Deep glacial troughs and stabilizing ridges unveiled beneath the margins of the Antarctic ice sheet, *Nature Geoscience*, **13**(2), 132–137.

Mouginot, J, E Rignot and B Scheuchl, 2019. Continent-wide, interferometric SAR phase, mapping of Antarctic ice velocity, *Geophysical Research Letters*, **46**(16), 9710–9718.

Nath, PC and DG Vaughan, 2003. Subsurface crevasse formation in glaciers and ice sheets, *Journal of Geophysical Research: Solid Earth*, **108**(B1).

Oerter, Hans, J Kipfstuhl, Jürgen Determann, Heinrich Miller, D Wagenbach, A Minikin and W Graft, 1992. Evidence for basal marine ice in the Filchner–Ronne Ice Shelf, *Nature*, **358**(6385), 399–401.

Padman, Laurie, Susan L Howard, Alejandro H Orsi and Robin D Muench, 2009. Tides of the northwestern Ross Sea and their impact on dense outflows of Antarctic Bottom Water, *Deep Sea Research Part II: Topical Studies in Oceanography*, **56**(13-14), 818–834.

Padman, Laurie, Matt King, Derek Goring, Hugh Corr and Richard Coleman, 2003. Ice-shelf elevation changes due to atmospheric pressure variations, *Journal of Glaciology*, **49**(167), 521–526.

Pattyn, Frank, 2003. A new three-dimensional higher-order thermomechanical ice sheet model: Basic sensitivity, ice stream development, and ice flow across subglacial lakes, *Journal of Geophysical Research: Solid Earth*, **108**(B8).

Pattyn, Frank, 2018. The paradigm shift in Antarctic ice sheet modelling, *Nature communications*, **9**(1), 1–3.

Pollard, David, Robert M DeConto and Richard B Alley, 2015. Potential Antarctic Ice Sheet retreat driven by hydrofracturing and ice cliff failure, *Earth and Planetary Science Letters*, **412**, 112–121.

Pritchard, HDx, Stefan RM Ligtenberg, Helen A Fricker, David G Vaughan, Michiel R van den Broeke and Laurence Padman, 2012. Antarctic ice-sheet loss driven by basal melting of ice shelves, *Nature*, **484**(7395), 502–505.

Qi, Chao, David J Prior, Lisa Craw, Sheng Fan, Maria-Gema Llorens, Albert Griera, Marianne Negrini, Paul D Bons and David L Goldsby, 2019. Crystallographic preferred orientations of ice deformed in direct-shear experiments at low temperatures, *The Cryosphere*, **13**(1), 351–371.

Reese, Ronja, G Hilmar Gudmundsson, Anders Levermann and Ricarda Winkelmann, 2018. The far reach of ice-shelf thinning in Antarctica, *Nature Climate Change*, **8**(1), 53.

Rignot, Eric, G Casassa, P Gogineni, W Krabill, AU Rivera and R Thomas, 2004. Accelerated ice discharge from the Antarctic Peninsula following the collapse of Larsen B ice shelf, *Geophysical research letters*, **31**(18).

Rignot, E, J Mouginot and B Scheuchl, 2011. MEaSUREs InSAR-based Antarctica ice velocity map, *Science*, **333**, 1427–1430.

Rignot, E, J Mouginot and B Scheuchl, 2017. MEaSUREs InSAR-based Antarctica ice velocity map, version 2, *Boulder, CO: NASA DAAC at the National Snow and Ice Data Center*.

Ritz, Catherine, Tamsin L Edwards, Gaël Durand, Antony J Payne, Vincent Peyaud and Richard CA Hindmarsh, 2015. Potential sea-level rise from Antarctic ice-sheet instability constrained by observations, *Nature*, **528**(7580), 115–118.

Riverman, KL, RB Alley, S Anandakrishnan, K Christianson, ND Holschuh, B Medley, A Muto and LE Peters, 2019. Enhanced firn densification in high-accumulation shear margins of the NE Greenland Ice Stream, *Journal of Geophysical Research: Earth Surface*, **124**(2), 365–382.

Robel, Alexander A, Hélène Seroussi and Gerard H Roe, 2019. Marine ice sheet instability amplifies and skews uncertainty in projections of future sea-level rise, *Proceedings of the National Academy of Sciences*, **116**(30), 14887–14892.

Rott, Helmut, Florian Müller, Thomas Nagler and Dana Floricioiu, 2011. The imbalance of glaciers after disintegration of Larsen-B ice shelf, Antarctic Peninsula, *The Cryosphere*, **5**(1), 125–134.

Scambos, T, R Ross, R Bauer, Y Yermolin, P Skvarca, D Long, J Bohlander and T Haran, 2008. Calving and ice-shelf break-up processes investigated by proxy: Antarctic tabular iceberg evolution during northward drift, *Journal of Glaciology*, **54**(187), 579–591.

Schlegel, Nicole-Jeanne, Helene Seroussi, Michael P Schodlok, Eric Y Larour, Carmen Boening, Daniel Limonadi, Michael M Watkins, Mathieu Morlighem and Michiel R Broeke, 2018. Exploration of Antarctic Ice Sheet 100-year contribution to sea level rise and associated model uncertainties using the ISSM framework, *The Cryosphere*, **12**(11), 3511–3534.

Schoof, Christian and Elisa Mantelli, 2021. The role of sliding in ice stream formation, *Proceedings of the Royal Society of London Series A*, **477**(2248), 20200870.

Scott, David W, 1979. On optimal and data-based histograms, *Biometrika*, **66**(3), 605–610.

Scott, Julian BT, Andrew M Smith, Robert G Bingham and David G Vaughan, 2010. Crevasses triggered on Pine Island Glacier, West Antarctica, by drilling through an exceptional melt layer, *Annals of Glaciology*, **51**(55), 65–70.

Shean, David E, Oleg Alexandrov, Zachary M Moratto, Benjamin E Smith, Ian R Joughin, Claire Porter and Paul Morin, 2016. An automated, open-source pipeline for mass production of digital elevation models (DEMs) from very-high-resolution commercial stereo satellite imagery, *ISPRS Journal of Photogrammetry and Remote Sensing*, **116**, 101–117.

Siegfried, Matthew R, Helen A Fricker, Sasha P Carter and Slawek Tulaczyk, 2016. Episodic ice velocity fluctuations triggered by a subglacial flood in West Antarctica, *Geophysical Research Letters*, **43**(6), 2640–2648.

Siegfried, Matthew R, Helen A Fricker, Mackenzie Roberts, Ted A Scambos and Slawek Tulaczyk, 2014. A decade of West Antarctic subglacial lake interactions from combined ICESat and CryoSat-2 altimetry, *Geophysical Research Letters*, **41**(3), 891–898.

Smith, Ben, Helen A Fricker, Alex S Gardner, Brooke Medley, Johan Nilsson, Fernando S Paolo, Nicholas Holschuh, Susheel Adusumilli, Kelly Brunt, Bea Csatho and others, 2020. Pervasive ice sheet mass loss reflects competing ocean and atmosphere processes, *Science*, **368**(6496), 1239–1242.

Stearns, Leigh A, Kenneth C Jezek and Cornelis J Van Der Veen, 2005. Decadal-scale variations in ice flow along Whillans Ice Stream and its tributaries, West Antarctica, *Journal of Glaciology*, **51**(172), 147–157.

Stephenson, Simon N and Robert A Bindschadler, 1988. Observed velocity fluctuations on a major Antarctic ice stream, *Nature*, **334**(6184), 695–697.

Stewart, Craig L, Poul Christoffersen, Keith W Nicholls, Michael JM Williams and Julian A Dowdeswell, 2019. Basal melting of Ross Ice Shelf from solar heat absorption in an ice-front polynya, *Nature Geoscience*, **12**(6), 435–440.

Stuart, AW and Colin Bull, 1963. Glaciological observations on the Ross Ice Shelf near scott base, Antarctica, *Journal of Glaciology*, **4**(34), 399–414.

Thomas, Robert H, 1973. The creep of ice shelves: interpretation of observed behaviour, *Journal of Glaciology*, **12**(64), 55–70.

Thyssen, Franz, Andreas Bombosch and Henner Sandhäger, 1993. Elevation, ice thickness and structure mark maps of the central part of the Filchner-Ronne Ice Shelf, *Polarforschung*, **62**(1), 17–26.

Tinto, KJ, L Padman, CS Siddoway, SR Springer, HA Fricker, I Das, F Caratori Tontini, DF Porter, NP Frearson, SL Howard and others, 2019. Ross Ice Shelf response to climate

driven by the tectonic imprint on seafloor bathymetry, *Nature Geoscience*, **12**(6), 441–449.

Trautmann, Eric, Laura Ray and Jim Lever, 2009. Development of an autonomous robot for ground penetrating radar surveys of polar ice, 1685–1690.

Tulaczyk, Slawek, W Barclay Kamb and Hermann F Engelhardt, 2000. Basal mechanics of Ice Stream B, west Antarctica: 2. Undrained plastic bed model, *Journal of Geophysical Research: Solid Earth*, **105**(B1), 483–494.

Vaughan, David G, 1993. Relating the occurrence of crevasses to surface strain rates, *Journal of Glaciology*, **39**(132), 255–266.

Vaughan, David G, Jonathan L Bamber, Mario Giovinetto, Jonathan Russell and A Paul R Cooper, 1999. Reassessment of net surface mass balance in Antarctica, *Journal of climate*, **12**(4), 933–946.

Van der Veen, CJ, 1999. Crevasses on glaciers, *Polar Geography*, **23**(3), 213–245.

Vieli, A, AJ Payne, A Shepherd and Z Du, 2007. Causes of pre-collapse changes of the Larsen B ice shelf: Numerical modelling and assimilation of satellite observations, *Earth and Planetary Science Letters*, **259**(3-4), 297–306.

van de Wal, RSW, X Zhang, S Minobe, S Jevrejeva, REM Riva, C Little, K Richter and MD Palmer, 2019. Uncertainties in long-term twenty-first century process-based coastal sea-level projections, *Surveys in Geophysics*, **40**(6), 1655–1671.

Weertman, Johannes, 1974. Stability of the junction of an ice sheet and an ice shelf, *Journal of Glaciology*, **13**(67), 3–11.

Zhang, Tong, Stephen F Price, Matthew J Hoffman, Mauro Perego and Xylar Asay-Davis, 2020. Diagnosing the sensitivity of grounding-line flux to changes in sub-ice-shelf melting, *The Cryosphere*, **14**(10), 3407–3424.

Zotikov, Igor A, Victor S Zagorodnov and Juriy V Raikovsky, 1980. Core drilling through the Ross Ice Shelf (Antarctica) confirmed basal freezing, *Science*, **207**(4438), 1463–1465.

APPENDIX A

AUTO-RIFT OUTPUTS

Here I present results from the auto-RIFT derived velocities. While kinematic outputs were derived on a yearly basis from 2014–2017, I found the best results by averaging these years together. Threshold values for shear strain rate and vorticity show good agreement with MEaSUREs2 values despite differences in horizontal resolution and time periods.

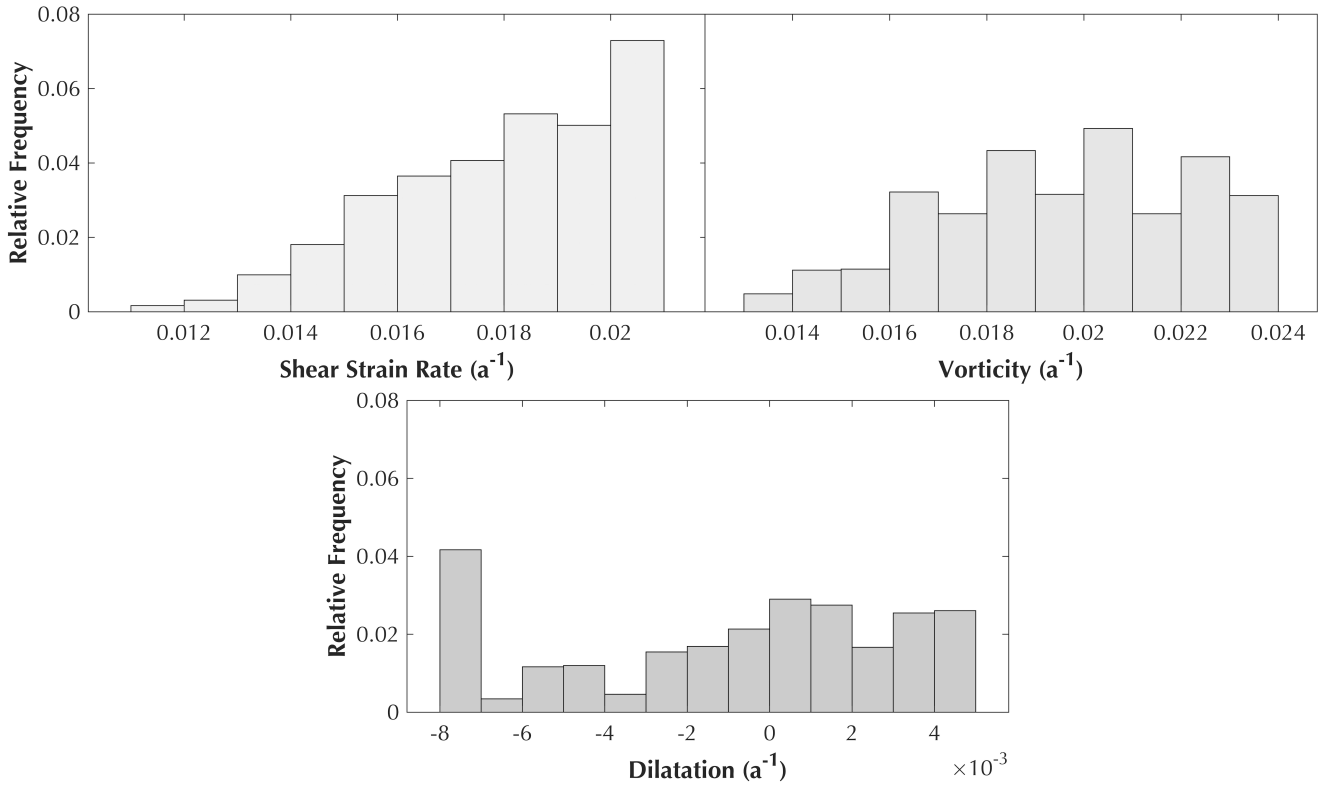

Figure A.1. Relative frequency distribution plots from auto-Rift velocity data. Plots of shear strain rate, vorticity, and dilatation

APPENDIX B

FREQUENCY DISTRIBUTION NORMALIZATION

The purpose of this section is to provide details on the subtleties of the relative frequency distribution plots in Fig. 2.3c and Fig. 2.4. It is important to note that these plots are not histograms of crevasse observations, but the relative frequency distribution of crevasses within a given bin. For example, Fig. 2.3c should not be interpreted to mean that 7% of crevasses occur between a shear strain rate of 0.019- 0.020, but rather that 7% of all observations within a shear strain rate of 0.019-0.02 are crevassed. Fig. B.1 provides a histogram of crevasse observations without normalization and a histogram of all observations; the division of the two provides the normalized plot in Fig. 2.3c.

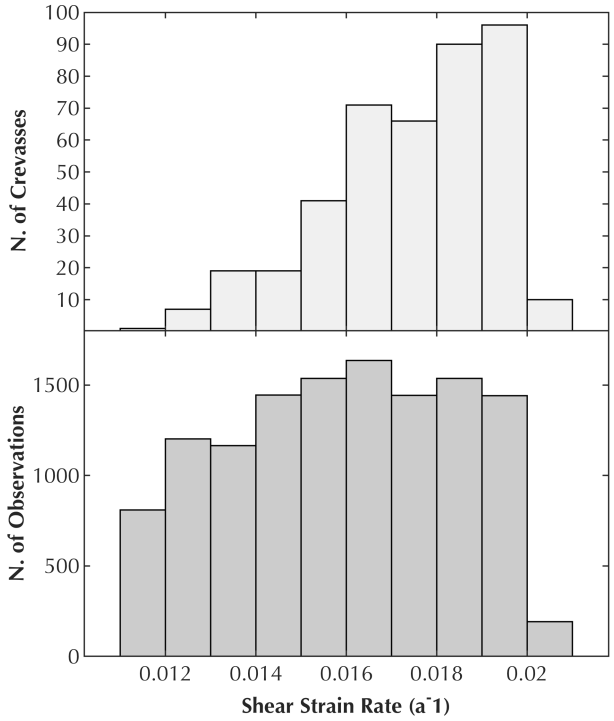

Figure B.1. Comparison of crevasse observations vs number of observations. (top) Histogram of crevasse observations. (bottom) Histogram of all observations.

APPENDIX C

GPS FIELD METHODS AND DATA PROCESSING

In order to map the flow and deformation of the region of interest, GPS surveys were carried out over two consecutive field seasons in 2014 and 2015. A network of 29 stakes was deployed between October 29, 2014 and November 9, 2014 and between October 28, 2015 and November 7, 2015 within a 12 x 12 km2 area of the McMurdo Shear Zone. Each season Trimble NetR9 receivers were deployed in rapid-static mode over periods of 2-3 hours at each stake to collect data at 15 s frequency. During the 2015 season, two of the receivers were deployed for the entirety of the campaign in an attempt to capture the full tidal cycle (Fig. 3.3; stations marked by black and white triangles). I processed geodetic dual-frequency GPS observations of the two tide stations using the precise point positioning technique through the Canadian Spatial Reference System Precise Point Position

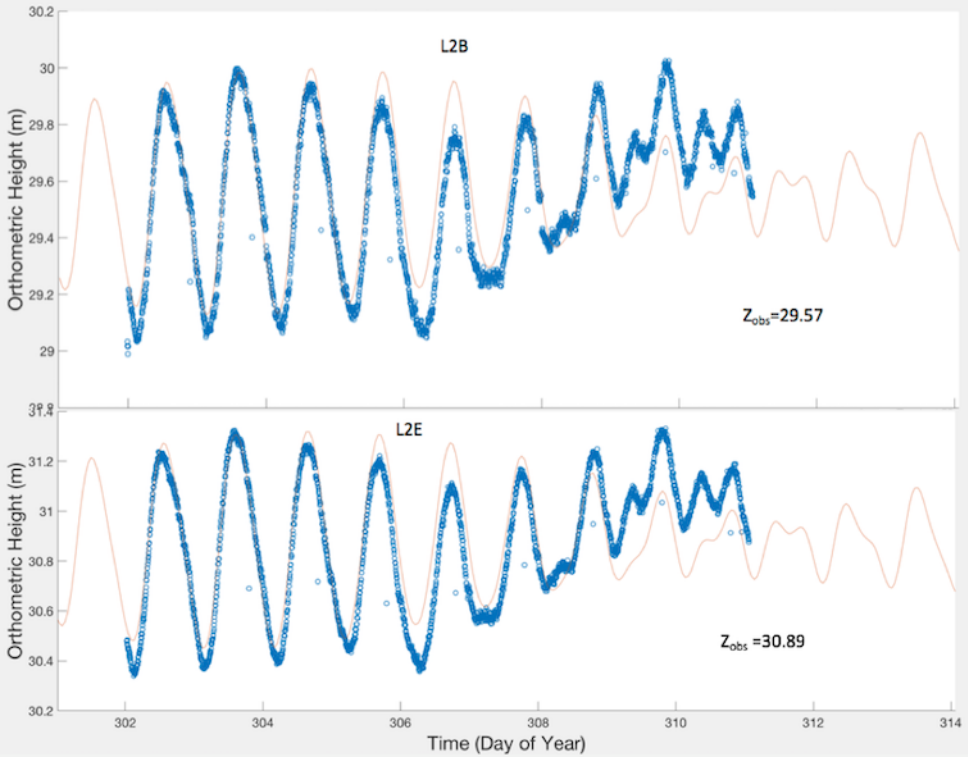

Figure C.1. Comparison of orthometric height of GPS to model tidal signal from CATS2008

(CRS-PPP) service in order to remove GNSS system clock errors and provide ellipsoidal heights. As the receivers were not placed on the ice surface, a post-processing correction of 1.65 m was applied to account for the height of the stake, as well as 1.5 cm to account for the antenna phase center. I then performed a geoid correction to convert to orthometric heights before averaging the data from 15 s to 5 min intervals to reduce errors (Fig. C.1). I then took the 9-day average of the GPS processed time series to solve for the height above mean sea level. However, because my time series did not cover the entire lunar cycle, I compared the modeled tidal signal for the same 2 locations from the CATS2008 model. I first averaged the model data over the same 9-day period and compared to the averaged model data over the full lunar cycle (29.5 days) to solve for a bias of 0.01 m. I then applied the bias to the GPS-derived 9-day average before comparing the tidally corrected orthometric heights to the DEM data. Stations L2B and L2E were shifted by 2.196 m and 2.055 meters respectively, giving an 2.13 m average correction to apply to the DEM.

BIOGRAPHY OF THE AUTHOR

Lynn Kaluzienski was born in Philadelphia, Pennsylvania. She attended Columbus High School and in May 2014 graduated with a B.S. in Physics and Astronomy from Emory University in Georgia. Before embarking upon her graduate degree, Lynn had not stepped foot outside the United States. Throughout her graduate degree she has become a world traveler, performing fieldwork in Antarctica, Greenland, Svalbard. In 2018, she moved to Alaska to become a visiting student at the University of Alaska Fairbanks. She has also participated as an instructor for the Juneau Ice Field Research Program and Girls in Icy Fjords Program. After graduation she plans to continue pursuing research in glaciology as a postdoctoral scholar at the University of Alaska Southeast. Lynn is a candidate for the Doctorate of Philosophy in Glaciology degree in the School of Earth and Climate Sciences from the University of Maine in December 2021. Lynn Marie Kaluzienski is a candidate for the Doctor of Philosophy degree in Glaciology and Remote Sensing from the University of Maine in December 2021.